Improvement in Runoff Parameterization for Global Climate Modelling

by

Jinliang Liu

A thesis submitted in conformity with the requirements
for the degree of Doctor of Philosophy
Graduate Department of Physics
University of Toronto

Improvement in Runoff Parameterization for Global Climate Modelling

Doctor of Philosophy, 2001, Jinliang Liu
Department of Physics, University of Toronto

Abstract

Diagnosed runoff was estimated from NCEP/NCAR reanalysis data for an 8-year period from 1987 to 1994. Bonan's land surface model (LSM) was run for the same period coupled to NCAR's CCM3. Comparisons between the diagnosed and simulated runoff indicate that, the runoff parameterization in the original LSM cannot produce a reasonable diagnosed horizontal distribution of runoff, which is important to the model climate. One of the possible reasons is the exclusion of topographic effects in the original runoff parameterization. Therefore, based on previous research results on river re-distribution models, a modification on the original runoff parameterization was proposed and implemented in the original LSM. This modification has two aspects: firstly, the topographic slopes cause outflows from higher topography and inflows into the lower topography points; secondly, topographic slopes also cause decrease of infiltration at higher topography and increases of infiltration at lower topography. Then changes in infiltration result in changes in soil moisture, surface fluxes and then in surface temperature. This mechanism is very clearly demonstrated in the point budgets analysis at the Andes Mountains vicinities. Analysis from a regional scale perspective in the Canadian GEWEX basin, the Mackenzie River basin, shows that the modified runoff parameterization can generate an expected horizontal distribution of total runoff which is much closer to the horizontal distribution of the observed and diagnosed runoff, and which is much more consistent with topography and thus very easy to explain physically. This represents a significant improvement over the original LSM. More importantly, very detailed analysis from a global perspective shows many very encouraging improvements introduced by the modified model

over the original model in simulating basic atmospheric climate properties such as thermodynamic features, precipitable water, net water exchange, and precipitation. The modified model somehow corrected some deficiencies evident in the AGCM. All of these improvements in the atmospheric climate simulation illustrate that the inclusion of topographic effects in the LSM can force the AGCM to produce a more realistic model climate. Analysis also shows that the modified model may improve the atmospheric CO_2 simulation which is very important to global environmental studies.

Acknowledgements

During the course of my Ph.D studies, there were many rough periods which I could not have overcome without the support of many individuals to whom I am wholeheartedly grateful. The most outstanding figure among them is my thesis supervisor, Professor Han-Ru Cho. My special tributes to him for providing me with a very enjoyable educational experience, as well as his insights, encouragement, understanding, patience and generous support. I have learned from him not only the academic necessities, but also the conducts of living. Thanks are also due to Professor W.R. Peltier and Professor G. W. Kent Moore for many valuable discussions and for serving on my supervisory committee. More thanks go to Professor G. W. Kent Moore for his generous offer of his DEC/Alpha machine and the ECMWF data in the early stage of this project. I also wish to thank Dr. R. E. Stewart at the Meteorological Service of Canada (MSC), the GEWEX Hydrometeorology Panel (GHP) Senior Scientist, for his valuable encouragement of my research and his kind help on our joint publication. Special thanks also go to Dr. G. S. Strong, Secretary of the Mackenzie Area GEWEX Studies (MAGS), Professor E. D. Soulis at the University of Waterloo and Professor D. P. Lettenmaier at the University of Washington, for their constructive comments on my research.

I really want to say many thanks to Dr. Chi-Fan Shih at the Data Support Section (DSS), Scientific Computing Section (SCD), NCAR, for his very kind help on using the NCEP/NCAR reanalysis data. Sincere thanks are also due to Dr. Erik Kluzek in the NCAR's CCM Core Group of the Climate and Global Dynamics (CGD) division, for his very timely help in running the NCAR CCM3/LSM. Thanks also go to all of those in the ccm-users news group who helped me in porting the CCM3/LSM to the DEC/Alpha machine.

Definitely, many of my colleagues have contributed, one way or the other, to the

success of my thesis. Together, they create a very stimulating and friendly environment. Thanks go to Dr. Jiansheng Zou, Dr. Shuzhan Ren, Dr. Zhenhao Bao, Dr. Boyd Tolton and Mr. Qi Liu for their many fine discussions and comments, to Mr. V. Smirnov for teaching me to use his ECMWF reanalysis dataset, and to Ms. Jennifer Lukovich and Mr. Amit Ghosh for proof reading parts of the thesis and related publications. I also wish to thank Dr. Rosemarie Drummond and Dr. Djoko Wirosoetisno for their extensive help on computer related problems, and Ms. Ana Sousa and Ms. Marianne Khurana for their warmhearted help from administrative perspectives.

To my mother and my father, there are no words which can express my gratitude to you for your lifetime support. It is your understanding, character, trust and care that brought me here today.

Finally, Lily Jianzhong Li, my wife and friend, I owe half of my success to you. You bring me the comfort and joy of life and always encourage me to concentrate on my studies. I also want to thank my son Tony Yuehua Liu. Your joyful spirit and love have given me great strength.

TO

my mother, Xiaoyun Li

and

my father, Ji Liu

Contents

List of Tables

List of Figures

Chapter 1

Introduction

Hydrological processes are attracting more and more interest from the global climate modelling community. Runoff is one of the most important hydrological processes and is included in most land surface models.

1.1 A Brief Review of Previous Studies

The development of land surface parameterizations has been rapid in recent years. These include the biosphere-atmosphere transfer scheme (BATS) (Dickinson et al. 1993) , the simple biosphere model (SiB) (Sellers et al. 1986), the simplified SiB (Xue et al. 1991), the biological ecological system transfer model (BEST) (Pitman et al. 1991), SECHIBA (Ducoudre et al. 1993), the Canadian land surface scheme (CLASS) (Verseghy 1991: Verseghy et al. 1993) and the most recently developed land surface model (LSM) (Bonan 1996b) at the National Center for Atmospheric Research (NCAR). Readers can find a brief review of these parameterizations in Bonan's papers (Bonan 1995, 1996b).

Along with the rapid development of these land surface parameterizations, the

verification of these models is clearly important. Bonan's LSM was chosen for this study for the following reasons.

- It was the latest-developed land surface model based on other models when this study began; It has more sophisticated physics package which includes more realistic interaction between different processes. It has higher resolution soil model (6-layer) than others (3-layer or 1-layer); It is widely used in the climate modelling community;

- It is freely available for downloading. On the contrary, it is very difficult to get other models for free.

Although Bonan's LSM has many advantages over other schemes, it does not include the lateral water fluxes caused by topography, which will be called the topographic effects in this study. This is confirmed by our verification results.

Most past studies tried to verify runoff parameterizations using hydrological data such as river flows. Liston et al. (1994) and Miller et al. (1994) verified some other runoff parameterizations by coupling river routing models into atmospheric global circulation models (AGCMs) and comparing the simulated river flows with the "observed" at monthly time scale. Bonan (1996a) compared his CCM2 (NCAR's Community Climate Model version 2) runoff output directly with the "observed" river flows while he also mentioned that the amplitude and timing of the simulated runoff are not necessarily the same as the "observed".

In this study, verification of the runoff parameterization is conducted by using both hydrological and atmospheric observational data. Different from previous studies which only discuss the area-integrated quantities (i.e. a single number for a big basin), this study emphasizes the horizontal distributions of hydrological variables, which we think are more important to the model climate.

Most river routing models include the lateral water fluxes caused by topography. But it seems more work is needed for the land surface models for AGCMs. Similar modifications are being proposed for the WAT-CLASS model (Soulis 2000), a combination of the WATerloo FLOOD forecast model (WATFLOOD) developed at the University of Waterloo, and the CLASS model of the MSC. The WATFLOOD model is a very high-resolution hydrological model. So, the WAT-CLASS is still in the category of river routing model which is very expensive to run when coupled to an AGCM. To avoid the expensive coupling with a river routing model, this study introduces the topographic effects directly into the runoff parameterization of the LSM.

1.2 Objectives of This Study

Verification of Bonan's LSM by comparing the simulated with the diagnosed total runoff from NCEP/NCAR reanalysis data reports a problem that Bonan's LSM does not include the lateral water exchange between neighbouring grid cells caused by topographic slopes. The main objective of this thesis is to propose a modification to fix this problem and eventually to improve the original model in simulating these aspects. The modification will make the LSM physically more realistic, and furthermore, the improved LSM will expectedly force the AGCM to give a more realistic climate. Improvements and deficiencies brought by the modification will be identified by comparing the modified model results and the original model results.

1.3 Structure of the Thesis

The above objectives also determined the structure of this thesis. Following this introduction, Chapter 2, provides a brief description of the original runoff parameterization in Bonan's LSM. Verification results for this LSM are provided in Chapter 3.

Detailed description on the NCEP/NCAR reanalysis data and model configurations are also given in Chapter 3. The summary of Chapter 3 describes a problem with Bonan's original runoff parameterization scheme: namely, the exclusion of the lateral water fluxes caused by topography. Based on this conclusion, Chapter 4 proposes a modified runoff parameterization and its implementation. In Chapter 5, to quantify the improvement of the runoff simulation based upon this modification and its impact on regional and global climates, the modified model results are compared with the original model results and some previous results of others. Significance check is also conducted in Chapter 5 by T-test and power spectrum analysis of atmospheric waves. Conclusions and discussion are offered in Chapter 6.

1.4 What's New in This Study

Compared with previous studies, this study is new in the following respects:

1. Because of the difficulty in obtaining the horizontal distribution of runoff from observational hydrological data, the first step of this study consists of a pioneering attempt in the field of estimating the horizontal distribution of runoff from atmospheric data (Cho and Liu 2001);

2. The above horizontal distribution of runoff from atmospheric data was used to verify the runoff parameterization in a land surface model (LSM). This is the first time this has been attempted to our knowledge (Cho and Liu 2001);

3. For the first time, topographic effects have been introduced directly into a runoff parameterization in a LSM (Liu and Cho 2001b), instead of by expensive coupling of a river routing model as in most previous and ongoing studies.

4. Detailed analysis shows that topography does have a very important impact on regional and global climates by modifying the horizontal distributions of runoff and infiltration. Furthermore, the modified model presents many encouraging improvements over the original model, on simulations of hydrological processes, climate processes, environmental processes, and the interaction among these processes.

5. This study could be a significant contribution to the central objective of the Canadian GEWEX (MAGS) project, i.e., understanding and modelling high latitude water and energy cycles (Cho and Liu 2000).

Chapter 2

The Runoff Parameterization in the Bonan LSM

2.1 Introduction

As shown in Figure 2.1, Bonan's LSM parameterizes interception, throughfall, snow accumulation and melt, infiltration, surface runoff, subsurface runoff/drainage, and redistribution within the soil column to simulate canopy water, snow water and soil water. All fluxes and pools of water are in units of kgm^{-2} or mm.

Precipitation first falls onto the vegetation (trees, grass, etc.) as shown in Figure 2.1. Part of the precipitation is intercepted by the vegetation and becomes canopy water. The remaining part of the precipitation goes through the vegetation and reaches the ground as throughfall and stemflow. Some of the canopy water returns back into the atmosphere by evaporation and transpiration (or, collectively called evapotranspiration). The total water on the ground surface is the summation of the throughfall, stemflow and snowmelt. Part of this water goes back to the atmosphere by evaporation. The remaining ground surface water tries to saturate the soil first

by infiltration. After the soil is saturated, the leftover of the ground surface water will flow into rivers or lakes as surface runoff. The infiltrated water into the ground forms the so-called subsurface runoff (or drainage, or underground flow in previous textbooks and papers). Total runoff is simply the sum of surface runoff and subsurface runoff. This is a simplified explanation of the water cycle shown in Figure 2.1. In fact, the formation of runoffs could be very complicated as readers can find in the next section.

In Bonan's LSM, vegetation structure is defined by time-varying leaf and stem areas and time-invariant canopy height, root profile, leaf dimension, carbon and nitrogen. For details about the treatment of vegetation in the model, readers are referred to Bonan (1996b). Next we will focus on the treatments of infiltration, surface runoff and subsurface runoff in Bonan's LSM.

2.2 Infiltration and Surface Runoff

The liquid water at the soil surface (i.e., throughfall, snow melt, dew) either infiltrates into the soil column q_{infl} (mms^{-1}) or is lost as surface runoff q_{over} (mms^{-1}). Ignoring, for the moment, spatial heterogeneity, surface runoff (mms^{-1}) is

$$R = \begin{cases} P + Q & \text{for } s \geq 1 \text{ and } P > 0 \\ P + Q - f^* & \text{for } s < 1,\ Q \geq f^*, \text{ and } P > 0 \\ P + Q - f^* & \text{for } s < 1,\ Q < f^*, \text{ and } P > f^* - Q \end{cases}$$

where P is throughfall (mms^{-1}), $Q = q_{melt} + q_{sdew}$ (mms^{-1}), q_{melt} and q_{sdew} are snow melt and dew respectively; $s = \frac{\theta_1}{\theta_{sat}}$ is the water content of the first soil layer relative to saturation, and f^* is the infiltration capacity (mms^{-1}) which depends on s. All the surface water $(P + Q)$ is lost as Dunne runoff when the soil is saturated $(s \geq 1)$. Horton runoff occurs when the soil is not saturated $(s < 1)$ and when $P + Q > f^*$.

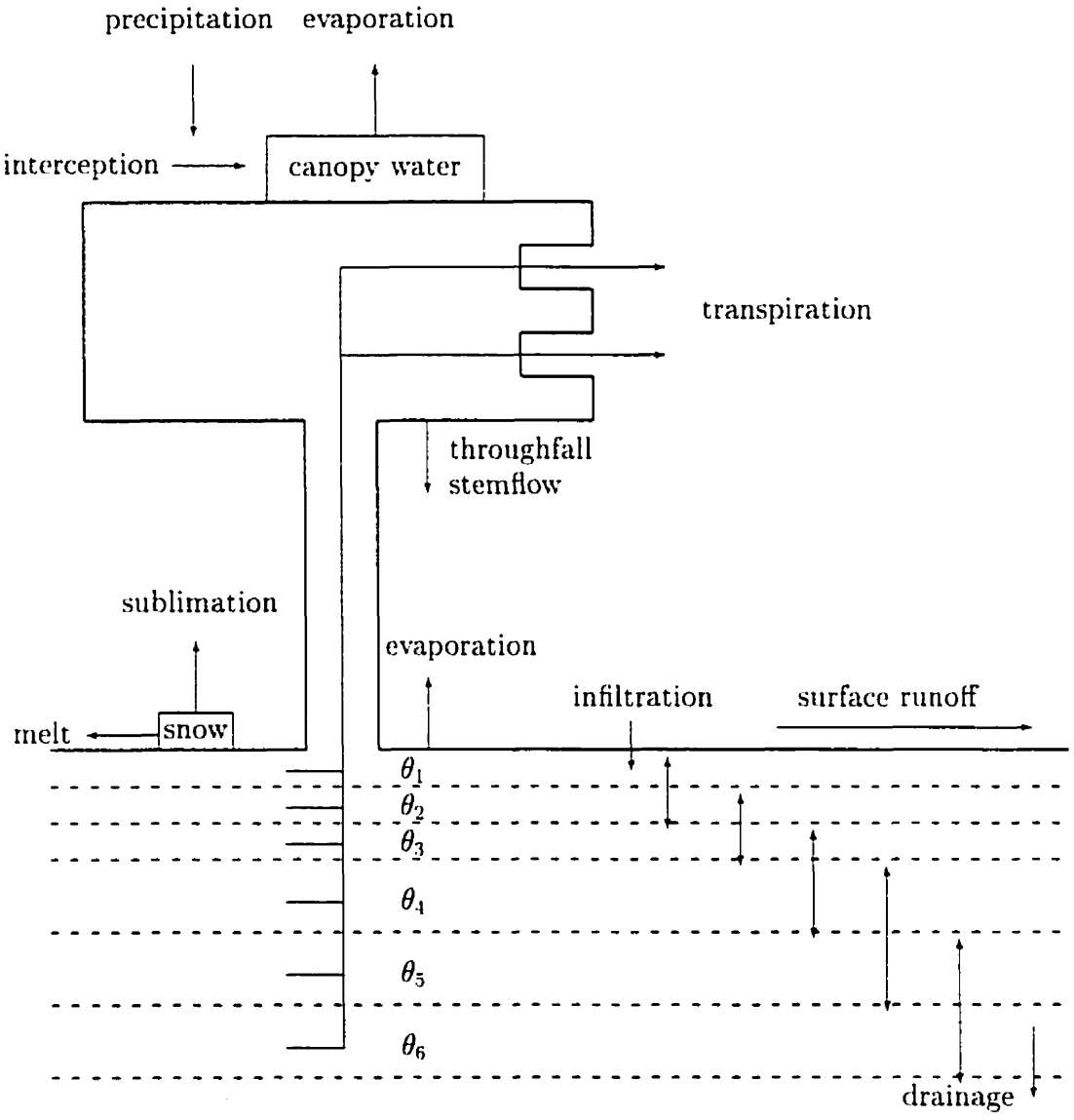

Figure 2.1: Schematic diagram of the water cycle in Bonan's LSM. (regenerated from Bonan 1996b)

This happens for two reasons: when $Q \geq f^*$, $P + Q > f^*$ for all $P > 0$; and when $Q < f^*$, $P + Q > f^*$ when $P > f^* - Q$. For non-soil surfaces, $R = 0$. Infiltration is $I = P + Q - R$.

Spatial heterogeneity is introduced in two ways. First, the mean rate of the throughfall differs between the regions k_c and $(1 - k_c)$.

$$\bar{r} = \begin{cases} q_{prcl} + \frac{q_{prcc}}{k_c} & \text{in region } k_c \\ q_{prcl} & \text{in region } (1 - k_c) \end{cases}$$

where q_{prcl} and q_{prcc} are large-scale and convective-scale precipitation rates respectively. k_c is a constant with a value of 0.6.

Second, P and s have stochastic spatial distributions similar to Entekhabi and Eagleson's (1989), Pitman et al.'s (1990, 1993), Dolman and Gregory's (1992), and Johnson et al.'s (1993) work with precipitation and Entekhabi and Eagleson's (1989) and Johnson et al.'s (1993) work with soil water as

$$f_P(P) = \frac{1}{\bar{P}} exp(-\frac{P}{\bar{P}}) \tag{2.1}$$

$$f_s(s) = \frac{1}{\bar{s}} exp(-\frac{s}{\bar{s}}) \tag{2.2}$$

where $\bar{P}$ is the average throughfall (mms^{-1}) for the region k_c or $(1 - k_c)$ and $\bar{s}$ is the average s. Consequently I and R are solved separately for each region assuming an exponential distribution of throughfall and soil water within the region and a constant rate of snow melt and surface dew. Total surface runoff q_{over} and infiltration q_{infl} are the weighted sums of the two regions.

Runoff for each region is given by

$$\begin{aligned} R = & \int_1^\infty \int_0^\infty (P + Q) f_P(P) dP f_s(s) ds + \\ & \int_{sQ}^1 \int_0^\infty (P + Q - f^*) f_P(P) dP f_s(s) ds + \\ & \int_0^{sQ} \int_{f^* - Q}^\infty (P + Q - f^*) f_P(P) dP f_s(s) ds \end{aligned} \tag{2.3}$$

where s_Q is the value of s at which $Q \geq f^*$. The first term is the Dunne runoff for the area $s \geq 1$. The next two terms are the Horton runoff for the area $0 \leq s < 1$.

The solution for R requires a physically realistic infiltration capacity that is easily integrated with respect to s. As in Entekhabi and Eagleson (1989)

$$f^* = k_{sat} v s + k_{sat}(1 - v) \tag{2.4}$$

where k_{sat} is the saturated hydraulic conductivity (mms^{-1}), $v = \frac{-(d\psi/ds)}{0.5\triangle z_1}$ evaluated for $s = 1$, ψ is the soil matrix potential (mm), and $\triangle z_1 = 100mm$ is the thickness of the first soil layer(Figure 2.2), with hydraulic properties defined at depth $\triangle z_1$. The value of s at which $Q \geq f^*$ is $s_Q = \frac{Q - k_{sat}(1-v)}{k_{sat} v}$. Expressions for k_{sat} and ψ are given as

$$k_{sat} = 0.0070556 \times 10^{-0.884 + 0.0153(\%sand)} \tag{2.5}$$

$$\psi_{sat} = -10.0 \times 10^{1.88 - 0.0131(\%sand)} \tag{2.6}$$

The solution for R is $R = R_1 + R_2 + R_3$, where R_1 is the Dunne runoff from the area with $S \geq 1$ and $P > 0$, namely

$$R_1 = (\bar{P} + Q) exp(-\frac{1}{\bar{s}}) \tag{2.7}$$

R_2 is the Horton runoff from the area $s_Q \leq s < 1$ (i.e., $s < 1$, $Q \geq f^*$ and $P > 0$, namely

$$\begin{aligned} R_2 = {} & [\bar{P} + Q - k_{sat}(1 - v)][exp(-\frac{s_Q}{\bar{s}}) - exp(-\frac{1}{\bar{s}})] + \\ & k_{sat} v[(1 + \bar{s}) exp(-\frac{1}{\bar{s}}) - (s_Q + \bar{s}) exp(-\frac{s_Q}{\bar{s}})] \end{aligned} \tag{2.8}$$

and R_3 is the Horton runoff from area $0 \leq s < s_Q$ (i.e., $s < 1$, $Q < f^*$) and $P > f^* - Q$, namely

$$R_3 = \frac{\bar{P}^2}{\bar{P} + k_{sat} v \bar{s}} exp[\frac{Q - k_{sat}(1 - v)}{\bar{P}}][1 - exp(-\frac{s_Q}{\bar{s}} - \frac{s_Q k_{sat} v}{\bar{P}})] \tag{2.9}$$

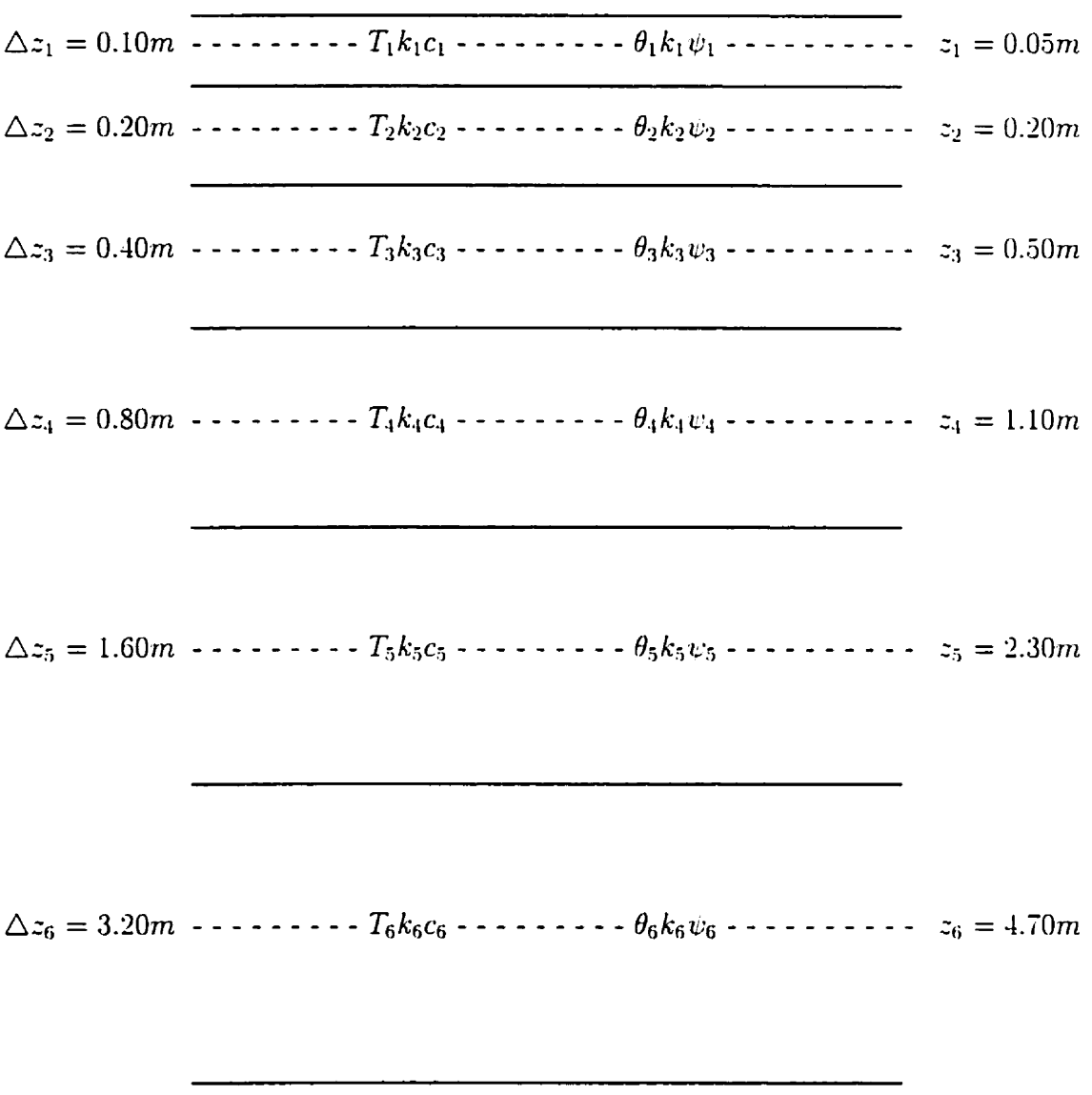

Figure 2.2: Schematic diagram of the six-layer soil profile. Thermal properties (temperature T_i; thermal conductivity k_i; volumetric heat capacity c_i) are defined at the center (depth z_i) of a layer with thickness Δz_i. The hydraulic properties (volumetric water content θ_i; hydraulic conductivity k_i; and matrix potential ψ_i) are also defined at depth z_i.

With $Q = 0$, $s_Q = 1$ and this equation reduces to Equation (15) in Entekhabi and Eagleson (1989). This runoff parameterization differs from Entekhabi and Eagleson (1989) in that it allows for a constant rate of snow melt and surface dew. It differs from Pitman et al. (1990, 1993) in that only throughfall, not the net flux of water at the surface, has an exponential distribution.

This runoff parameterization was found to give too much surface runoff, resulting in dry soils, when coupled to a AGCM (Bonan 1996b). The Dunne runoff was adjusted as $P + Q - k_{sat}$ for $s \geq 1$ and $P > k_{sat} - Q$, resulting in

$$R_1 = \int_1^{\infty} \int_{k_{sat}-Q}^{\infty} (P + Q - k_{sat}) f_P(P) dP f_s(s) ds = \bar{P} exp(\frac{Q - k_{sat}}{\bar{P}} - \frac{1}{\bar{s}}) \qquad (2.10)$$

for $Q < k_{sat}$ and

$$R_1 = (\bar{P} + Q - k_{sat}) exp(-\frac{1}{\bar{s}}) \qquad (2.11)$$

for $Q > k_{sat}$. This adjusted Dunne runoff greatly reduces surface runoff compared with the standard method.

2.3 Soil Water

Soil water is calculated from the conservation equation

$$\frac{\Delta\theta\Delta z}{\Delta t} = -q_i + q_o - e \qquad (2.12)$$

where θ is the volumetric soil water content ($mm^3 mm^{-3}$), Δz is the soil thickness (mm), Δt is the time step (seconds), e is the evapotranspiration loss (mms^{-1}), and q_i and q_o are fluxes of water (mms^{-1}) into and out of soil (positive in the upwards direction). Vertical water flow in an unsaturated porous media is described by Darcy's law as

$$q = -k[\frac{\partial(\psi + z)}{\partial z}] = -k(\frac{\partial\psi}{\partial z} + 1) = -k(\frac{\partial\theta}{\partial z}\frac{\partial\psi}{\partial\theta} + 1) \qquad (2.13)$$

where k is the hydraulic conductivity (mms^{-1}), ψ is the soil matrix potential (mm), and z is height (mm) above some datum in the soil column. Setting $e = 0$, so that $\frac{\Delta\theta}{\Delta t} = -(\frac{q_i - q_o}{\Delta z})$, i.e. $\frac{\partial\theta}{\partial t} = -\frac{\partial q}{\partial z}$, results in the Richards equation

$$\frac{\partial\theta}{\partial t} = \frac{\partial}{\partial z}[k(\frac{\partial\theta}{\partial z}\frac{\partial\psi}{\partial\theta} + 1)] \tag{2.14}$$

This equation, with $e = q_{seva} + q_{tran}$ (i.e., soil evaporation and transpiration) and with the boundary conditions of q_{infl} as the flux of water into the soil and gravitational drainage $q_{drai} = k$ as the flux of water at the bottom of the soil column, is numerically implemented for a sixlayer soil to calculate soil water. For irrigated crops, soil layers to a depth of 1 m are kept saturated during the growing season (i.e., when leaf area index is greater than zero). Consequently, soil water is conserved only for nonirrigated soils, where

$$\sum_i \Delta\theta_i \Delta z_i = (q_{infl} - q_{seva} - q_{tran} - q_{drai})\Delta t \tag{2.15}$$

2.3.1 Hydraulic Properties

The hydraulic conductivity k and the soil matrix potential ψ vary with θ and soil texture based on the work of Clapp and Hornberger (1978) and Cosby et al. (1984). For the i^{th} layer,

$$k_i = k_{sat} s_i^{2b+3} \tag{2.16}$$

$$\psi_i = \psi_{sat} s_i^{-b} \tag{2.17}$$

where $s_i = \frac{\theta_i}{\theta_{sat}}$. Cosby et al. (1984) empirically related the hydraulic conductivity at saturation k_{sat} (mms^{-1}), the matrix potential at saturation ψ_{sat} (mm), the water content at saturation θ_{sat} (i.e. porosity), and b to %sand and %clay as in equations x and y. And

$$\theta_{sat} = 0.489 - 0.00126(\%sand) \tag{2.18}$$

$$b = 2.91 + 0.159(\%clay) \tag{2.19}$$

From the definition of ψ, the water content when the soil is dry θ_{dry} and the optimal water content for evapotranspiration θ_{opt} , which are used in the calculation, are

$$\theta_{dry} = \theta_{sat}(\frac{-316230}{\psi_{sat}})^{-\frac{1}{b}} \tag{2.20}$$

$$\theta_{opt} = \theta_{sat}(\frac{-158490}{\psi_{sat}})^{-\frac{1}{b}} \tag{2.21}$$

2.3.2 Numerical Solution

As with soil temperatures, the soil column is discretized into six layers with thickness Δz_i of 100, 200, 400, 800, 1600, and 3200 mm (Figure 2.2). Hydraulic properties (i.e., water content θ_i $[mm^3mm^{-3}]$; hydraulic conductivity k_i $[mms^{-1}]$; matrix potential ψ_i $[mm]$) are defined at the center of each layer with depth z_i (mm) (Figure 2.1).

Analogous to the soil heat flux, the flux of water q_i (mms^{-1}) between layers i and $i+1$ is

$$q_i = -[\frac{(\psi_i + z_i) - (\psi_{i+1} + z_{i+1})}{\frac{\Delta z_i}{2k_i} + \frac{\Delta z_{i+1}}{2k_{i+1}}}] \tag{2.22}$$

where with $z_i - z_{i+1} = (\Delta z_i + \Delta z_{i+1})/2$,

$$q_i = -[\frac{2(\psi_i - \psi_{i+1}) + (\Delta z_i + \Delta z_{i+1})}{\frac{\Delta z_i}{k_i} + \frac{\Delta z_{i+1}}{k_{i+1}}}] \tag{2.23}$$

These equations are derived, with reference to Figure 2.2, assuming the water flux from the i^{th} layer (depth z_i) to the interface between the i^{th} and the $(i+1)^{th}$ layer (depth $z_i + 0.5z_i$) equals the water flux from the interface to the $(i+1)^{th}$ layer (depth z_{i+1}), i.e.,

$$-k_i[\frac{(\psi_i + z_i) - (\psi_m + z_m)}{\frac{1}{2}\Delta z_i}] = -k_{i+1}[\frac{(\psi_m + z_m) - (\psi_{i+1} + z_{i+1})}{\frac{1}{2}\Delta z_{i+1}}] \tag{2.24}$$

where ψ_m is the interface matrix potential and z_m is the interface depth.

The water balance for the i^{th} layer is

$$\frac{\Delta\theta_i \Delta z_i}{\Delta t} = -q_{i-1} + q_i - e_i \tag{2.25}$$

v and k are non-linear functions of θ (last section) so that $q_i = f(\theta_i, \theta_{i+1})$. with q_i approximated as

$$q_i = q_i^n + \frac{\partial q_i}{\partial \theta_i}\Delta\theta_i + \frac{\partial q_i}{\partial \theta_{i+1}}\Delta\theta_{i+1}, \tag{2.26}$$

where q_i^n is the water flux evaluated at the beginning of the time step. the water balance for the i^{th} layer is substitution of the above equation into the water balance equation. we have

$$\begin{aligned} e_i + q_{i-1}^n - q_i^n &= -[\frac{\partial q_{i-1}}{\partial \theta_{i-1}}]\Delta\theta_{i-1} + \\ &\quad [\frac{\partial q_i}{\partial \theta_i} - \frac{\partial q_{i-1}}{\partial \theta_i} - \frac{\Delta z_i}{\Delta t}]\Delta\theta_i + [\frac{\partial q_i}{\partial \theta_{i+1}}]\Delta\theta_{i+1}. \end{aligned} \tag{2.27}$$

which is a tridiagonal system of equations for $\Delta\theta$. If set

$$u = -2(\psi_i - \psi_{i+1}) - (\Delta z_i + \Delta z_{i+1}) \tag{2.28}$$

$$v = \Delta z_i k_i^{-1} + \Delta z_{i+1} k_{i+1}^{-1} \tag{2.29}$$

then, $\frac{\partial}{\partial q_i}$ and $\frac{\partial}{\partial q_{i+1}}$ give

$$\frac{\partial q_i}{\partial \theta_i} = [-2v\frac{d\psi_i}{d\theta_i} + u\frac{\Delta z_i}{k_i^2}\frac{dk_i}{d\theta_i}]v^{-2} \tag{2.30}$$

$$\frac{\partial q_i}{\partial \theta_{i+1}} = [-2v\frac{d\psi_{i+1}}{d\theta_{i+1}} + u\frac{\Delta z_{i+1}}{k_{i+1}^2}\frac{dk_{i+1}}{d\theta_{i+1}}]v^{-2} \tag{2.31}$$

From the definition of k_i and ψ_i, we have

$$\frac{dk_i}{d\theta_i} = (\frac{2b+3}{\theta_i})k_i \tag{2.32}$$

$$\frac{d\psi_i}{d\theta_i} = -(\frac{b}{\theta_i})\psi_i. \tag{2.33}$$

The boundary conditions are

$$\begin{cases} q_{i-1} = -q_{infl} & \text{for the first soil layer } (i=1) \\ q_i = -k_i & \text{for the bottom soil layer } (i=6) \\ e_i = q_{seva} + q_{tran} r_i & \text{for the first soil layer } (i=1) \\ e_i = q_{tran} r_i & \text{for other soil layers} \end{cases}$$

The last two equations mean that surface evaporation is removed from the first soil layer and transpiration is removed from each soil layer in proportion to the relative root abundance r_i. The water balance for the first soil layer ($i = 1$) is, therefore,

$$\frac{\triangle\theta_1 \triangle z_1}{\triangle t} = q_{infl} + q_1 - e_1 \tag{2.34}$$

and

$$e_1 - q_{infl} - q_1^n = [\frac{\partial q_1}{\partial \theta_1} - \frac{\triangle z_1}{\triangle t}]\triangle\theta_1 + [\frac{\partial q_1}{\partial \theta_2}]\triangle\theta_2. \tag{2.35}$$

For the bottom layer ($i = 6$),

$$q_6 = -k_6 = -k_6^n - \frac{dk_6}{d\theta_6}\triangle\theta_6 \tag{2.36}$$

so that the water balance for this layer is

$$e_6 + q_5^n - q_6^n = -[\frac{\partial q_5}{\partial \theta_5}]\triangle\theta_5 - [\frac{\partial q_6}{\partial \theta_6} + \frac{\partial q_5}{\partial \theta_6} - \frac{\triangle z_6}{\triangle t}]\triangle\theta_6 \tag{2.37}$$

The subsurface runoff/drainage is

$$q_{drai} = -q_6 \tag{2.38}$$

Chapter 3

Verification of Bonan's Runoff Parameterization

In this chapter, the atmospheric method to diagnose runoff will first be reviewed. A "bug" in some previous studies is reported and corrected in this study. This is followed by the data used in this study and the verification results. The last section will be the summary and a problem in Bonan's original runoff parameterization will be reported, which will be the basis for the next chapter.

3.1 The Atmospheric Method to Diagnose Runoff

It is well known in the field of climatology that moisture flux divergence gives water balance information that can complement the traditional hydrological data such as precipitation, evaporation and runoff/discharge (Peixoto and Oort, 1983). The basic concept of using atmospheric data to estimate the terrestrial water balance was first presented by Starr and Peixoto(1958). The application of this concept to regional studies (Rasmusson, 1968) or a region and period with special observations

(Peixoto, 1970), has been troublesome because there were only a few scattered observation stations of upper air soundings (Bryan and Oort, 1984). Brubaker et al. (1994) interpolated these upper air-sounding data onto a regular grid and analyzed the atmospheric moisture fluxes over North and South Americas. Rasmusson(1977) suggested that this method to estimate the regional water balance using moisture flux divergence should be useful and accurate for climatological estimates over regions larger than $10^6 km^2$ and over monthly or longer periods, with the operational rawinsonde network and the observational schedules. Since 1980, objective analysis data have been prepared in the context of prescribing initial and boundary conditions for daily numerical weather forecasting using various models and observational data. In recent years, re-analysis data such as the ECMWF and the NCEP/NCAR re-analyses data are available with much more improved spatial resolution and more recent analysis techniques. Therefore, it is worth applying such atmospheric data to the estimation of water balance in river basins.

As stated by Oki et al. (1995), another advantage of the atmospheric water balance method is its good global availability. It is not easy to collect discharge/river flow data and cover all the continents. Even though the spatial density of the observational network varies among regions, the atmospheric data, especially the new re-analyses data, cover the whole world.

As formulated by Peixoto(1973), Alestalo(1983) and others, the rate of change of water vapor, W, in an atmospheric column is given by

$$\frac{\partial W}{\partial t} + \nabla \cdot \vec{Q} = E - P \tag{3.1}$$

where E is the evapotranspiration; P precipitation; And $\vec{Q}$ is the vertically integrated moisture flux given by

$$\vec{Q} = \frac{1}{g} \int_{p_{sfc}}^{p_{top}} (q\vec{V}) dp \tag{3.2}$$

where q is the atmospheric specific humidity, $\vec{V}$ is the wind vector, and p_{sfc} and p_{top} are the surface pressure and the pressure on the top of the atmosphere.

The corresponding expression for the soil column is

$$\frac{\partial S}{\partial t} + \nabla \cdot \vec{F} = P - E \tag{3.3}$$

where S is the column water content of the soil-ocean-cryosphere and: $\vec{F}$ is the lateral transport of water. The divergence of this transport could be complicated because it includes both surface runoff and subsurface flows in terrestrial regions and the advection of ice and water in the ocean. It is the total runoff to the best of our knowledge, i.e. the sum of surface runoff and subsurface runoff.

If we integrate Eqs. (3.1) and (3.2) for a long time period, compared with other terms, the contributions of $\int_{longtime} \frac{\partial W}{\partial t} dt$ and $\int_{longtime} \frac{\partial S}{\partial t} dt$ are negligible. Therefore, we obtain the approximation of runoff R expressed by the atmospheric moisture flux con/divergence as

$$\begin{aligned} R &\approx \int_{longtime} \nabla \cdot \vec{F} dt = \int_{longtime} (P - E) dt \\ &= -\int_{longtime} \nabla \cdot \vec{Q} dt = -\frac{1}{g} \int_{longtime} \int_{p_{sfc}}^{p_{top}} (q\vec{V}) dp dt \end{aligned} \tag{3.4}$$

or for short

$$R \approx -\frac{1}{g} \int_{longtime} \int_{p_{sfc}}^{p_{top}} (q\vec{V}) dp dt \tag{3.5}$$

This is the equation we will use to verify the runoff parameterization.

The National Center for Environmental Prediction (NCEP) / National Center for Atmospheric Research (NCAR) reanalysis data from 1987 to 1994 were used for the verification. A brief description about the data can be found in section 3.2.2: and for details about the NCEP/NCAR reanalysis data, readers are referred to Kalnay et al (1996).

3.2 Topography and the Green Theorem

This section reports a "bug" in some previous studies on estimating atmospheric moisture flux con/divergence using Green Theorem. Simple calculation results show in this section support our correction of the "bug".

3.2.1 Introduction

The Green Theorem(Danielson 1997) on a domain is

$$\iint \nabla \cdot \vec{Q}\, dS = \oint_{outer} \vec{Q} \cdot \vec{n} dl - \oint_{inner} \vec{Q} \cdot \vec{n} dl \tag{3.6}$$

Where $\vec{Q}$ is any vector, $\vec{n}$ is an outward pointing unit vector normal to the domain boundaries, dS is the area element in the integration domain and dl is a line segment of the domain boundaries. On the right hand side(RHS) of (3.6), the subscripts of the line integration "outer" and "inner" indicate the outer and inner boundaries respectively. On a simply connected plane, or on a multiply connected plane with uniform distribution of $\vec{Q}$ along the inner boundary, the second line integration on the RHS of (3.6) is zero provided that the inner boundaries are closed loops. Otherwise, the line integration along the inner boundary has to be considered, i.e., subtracted from the line integration along the outer boundary. This is the case when (3.6) was used for real-time observational data over complex topography.

This theorem has been widely used in the calculation of flux divergence in atmospheric science for its simplicity(Walsh et al. 1994, Serreze et al. 1995). For real-time atmospheric observational data, the lower vertical levels often intersect with complex topography. Equation (3.6) then becomes an integration over a multiply connected domain. Nonuniformity is a typical feature for most atmospheric variables. Therefore, both terms on the RHS of (3.6) should be considered. To illustrate this point,

we will use Green Theorem to calculate moisture flux divergence over the Mackenzie River Basin (MRB). The MRB was proposed as one of the intensive study areas in Canada for the international Global Water and Energy cycle EXperiment(GEWEX). The area has a rather complex terrain with the Rocky Mountains on the west side of the basin.

3.2.2 Data and Methodology

The NCEP/NCAR reanalysis data (Kalnay et al 1996) in 1994 was used for this study. The resolution for this data is 2.5° × 2.5° with 8 pressure levels in the vertical from 1000hPa to 300hPa. Figures 3.1 and 3.2 show the horizontal computation area. The frame ABCDEFGHA encloses the MRB. The contour lines were drawn for $\sigma = P_k/P_s$ (Figure 3.1 for 1000hPa and Figure 3.2 for 925hPa), where P_k is the pressure on the current level, and P_s is the surface pressure at that point. If $\sigma > 1$, the grid is underground. From Figure 3.1, nearly all of the calculation area is underground on the 1000hPa pressure surface. On the 925hPa surface, the underground area is framed by the polygon IBCDQPONMLKJI in Figure 3.2. The changes in the underground area on these two levels are slight from month to month.

To avoid errors generated from the numerical models, instead of the forecasts (at 3-hour or 6-hour intervals), this study used only the analysis data at 00:00GMT and 12:00GMT, when upper atmospheric observation is available. The calculation was done under the assumption of steady conditions between these two times, i.e., no diurnal changes were counted. Consequently, horizontal moisture flux divergence over the MRB was calculated twice a day at 00:00GMT and 12:00GMT. Horizontal moisture flux con/divergence on a pressure level is defined as $\nabla \cdot \vec{Q} = \nabla \cdot (q\vec{V})$, where q is the specific humidity and $\vec{V}$ is the horizontal wind vector. Then equation (3.6)

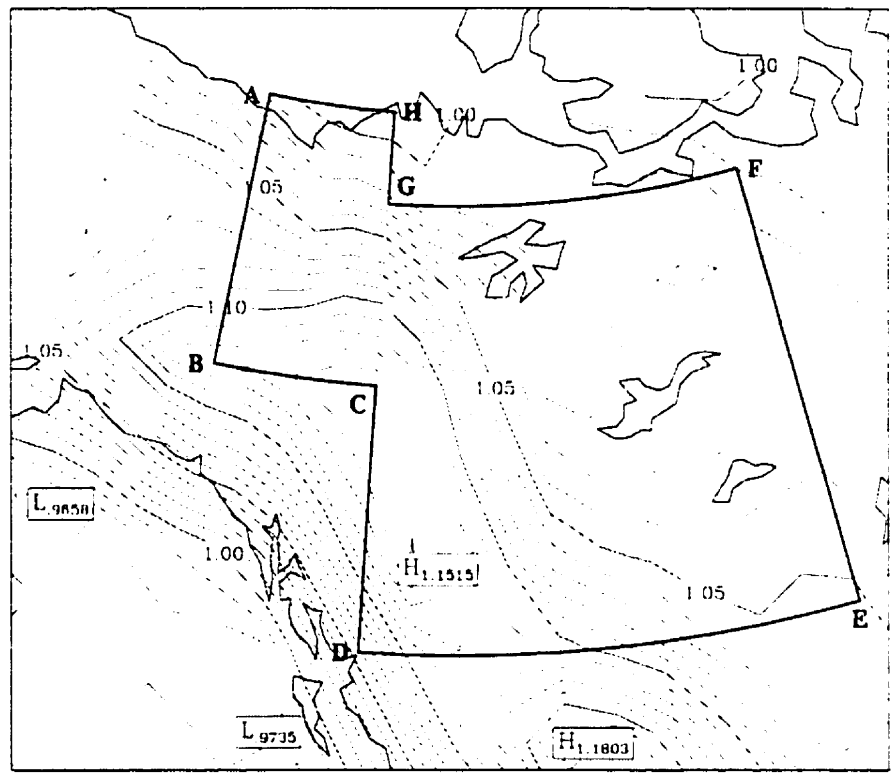

Figure 3.1: Computational area with σ contours (with intervals of 0.01) on 1000hPa surface. Polygon ABCDEFGA frames the Mackenzie River Basin(MRB)

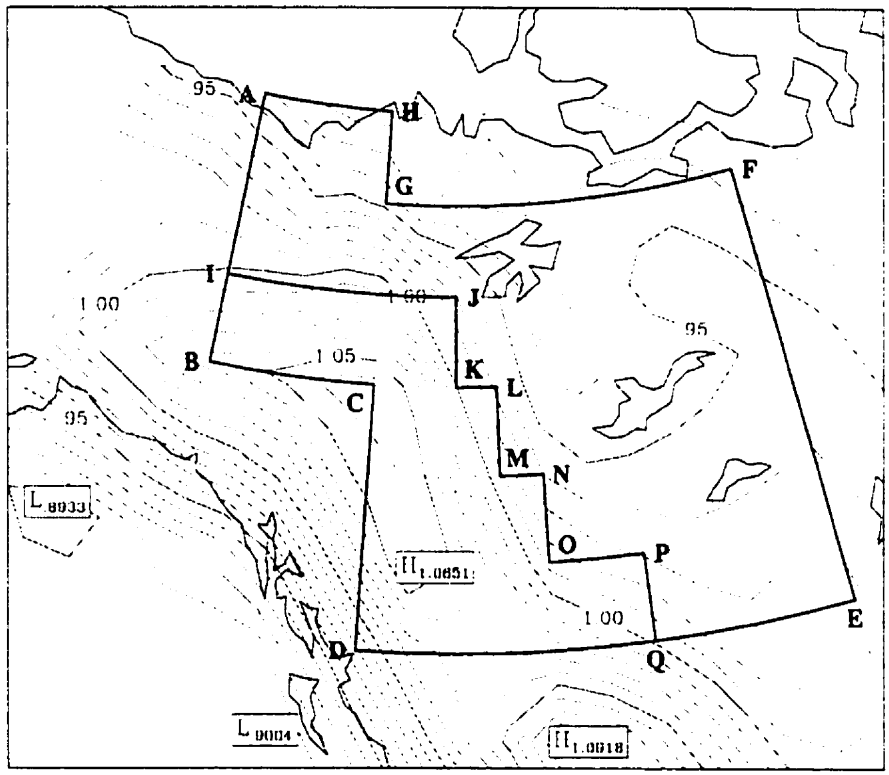

Figure 3.2: Computational area with σ contours (with intervals of 0.01) on 925hPa surface. Polygon ABCDEFGA frames the Mackenzie River Basin(MRB) and area framed by polygon IBDQPONMLKJI is underground.

can be written as

$$\iint \nabla\cdot(q\vec{V})\,dS = \oint_{outer}(q\vec{V})\cdot\vec{n}dl - \oint_{inner}(q\vec{V})\cdot\vec{n}dl \tag{3.7}$$

Before the calculations of moisture flux divergence, the data was preprocessed by putting q to zero if $q < 0$ (for only a few points with errors generated from the reanalysis procedure), and setting u, v and q to zero if $\sigma > 1$ (for the underground points).

To demonstrate the effects of topography, three methods were used to estimate horizontal moisture flux divergence.

Method 1 Calculate the RHS of (3.7) on each level to obtain the line integration on each level $(LI)_p$ and then calculate the vertical integration of $(LI)_p$.

$$I_1 = \frac{1}{g}\int_{1000hPa}^{300hPa}(LI)_p dp \tag{3.8}$$

Note that, to account for the topographic effects of the Rocky Mountains, both line integrals on the RHS of (3.7) on the first level 1000hPa were set to 0 because, as shown in Figure 3.1, the whole computational area is underground. On the second level at 925hPa (Figure 3.2), the computational area is multiply connected, i.e., there are both inner and outer boundaries. The line integral on the second level 925hPa was calculated as the difference between integrals along the outer and inner boundaries represented by polygons ABCDQEFGHA and IBCDQPONMLKJI respectively. This is equivalent to the line integration along AIJKLMNOPQEFGHA.

Method 2 Calculate the moisture divergence using $\nabla\cdot(q\vec{V})$ on each level first, then calculate the LHS area integral of (3.7) on each level to obtain $(AI)_p$, and last, calculate the vertical integration of $(AI)_p$.

$$I_2 = \frac{1}{g}\int_{1000hPa}^{300hPa}(AI)_p dp \tag{3.9}$$

Note, the area integration on the first level 1000hPa was set to 0 for the same reason as in the previous method. The area integration on the second level 925hPa was calculated only over the above-ground area circled by AIJKLMNOPQEFGHA in Figure 3.2. According to (3.7), this should be equal to I_1 in theory. For levels higher than 925hPa, the area integration was calculated over the region circled by ABCDEFGHA in Figure 3.1.

Method 3 First, vertically integrate qu and qv, the components of $q\vec{V}$ as in Walsh et al. (1994) and Serreze et al. (1995),

$$(VI)_{qu} = \frac{1}{g}\int_{1000hPa}^{300hPa} qudp \tag{3.10}$$

$$(VI)_{qv} = \frac{1}{g}\int_{1000hPa}^{300hPa} qvdp \tag{3.11}$$

then calculate the area integration on the RHS of (3.7) along the outer boundary ABCDEFGHA in Figure 3.1.

$$I_3 = \oint_{outer} (\vec{VI})_{quqv} \cdot \vec{n} dl \tag{3.12}$$

where

$$(\vec{VI})_{quqv} = (VI)_{qu}\vec{i} + (VI)_{qv}\vec{j} \tag{3.13}$$

This method, although it appears to have included the effects of topography by setting the values of u, v, q and moisture flux to zero underground, cannot include the effect of topography completely because the values of horizontal moisture fluxes were left unchanged in regions above the mountains. At the topographic surface, although the normal components of mass or moisture fluxes should be zero, their horizontal components may not be zero because of the slopes of ground surfaces of the mountains and the nonzero values of their tangential components. Therefore, to completely include the effects of topography, Method 1 should be used.

In the calculations, central differencing was used for horizontal derivatives. Area integration was calculated by multiplying the grid cell area ($2.5° \times 2.5°$) by the average of the 4 corner values surrounding this area. The expression for the vertical integration used above can be written as

$$I_n = \frac{1}{g}\int_{1000hPa}^{300hPa} A dp = \frac{1}{g}\sum_{l=1}^{7}(\frac{A_l + A_{l+1}}{2})(p_l - p_{l+1}) \tag{3.14}$$

where A is $(LI)_p$, $(AI)_p$, or qu and qv for $n = 1, 2$ and 3; l is the vertical level number ranging from 1 to 8; and p_l is the pressure on the corresponding level.

3.2.3 Results

The vertical profiles of horizontal moisture flux divergence over MRB for the year 1994 are shown in Figure 3.3 according to the three methods outlined above. One can see from Figure 3.3 that, the most significant differences come from the lower levels, 1000hPa and 925hPa, which intercept with the Rocky Mountains. Concerning the lowest 2 levels, the longer the integration time, the less the difference between the thick solid line and the thin solid line, i.e., the better the approximation using Green Theorem. In the one-time profile (labeled as Aug. 16, 94), the difference between them is the largest; while in the yearly-integrated profile (labeled as 1994), these two are nearly equal. But the integration time does not reduce the difference between the dashed line and the two solid lines at all, which was mainly caused by the topographic effects.

The effects of topography can also be found from the results of I_1, I_2 and I_3 defined in section 3.3.2. Values of these integrals are listed in Table 3.1. Even for the one-year long time integration, one can still find that the difference between I_3 and I_1 is larger than that between I_2 and I_1. The difference between I_1 and I_2 is

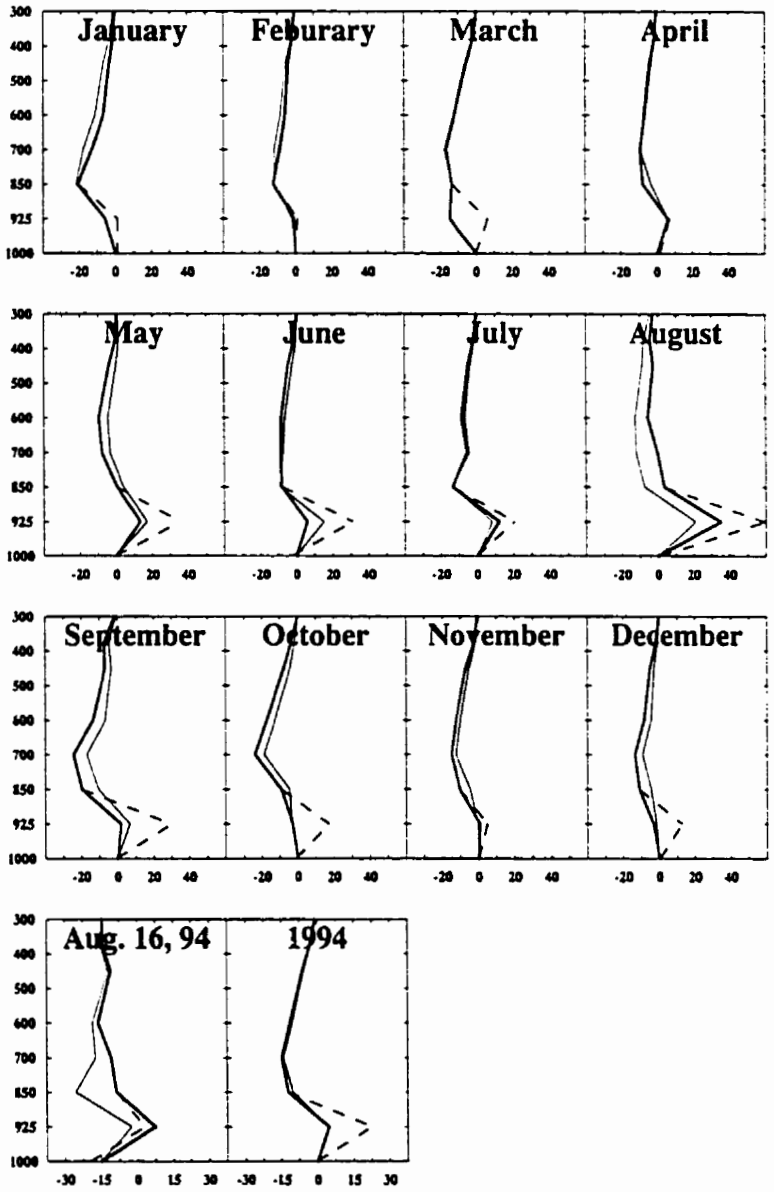

Figure 3.3: Vertical profiles of horizontal moisture flux con/divergence ($\times 10^8 Kg$) over MRB, for monthly (the first 12 panels), a single time at 00:00GMT on August 16 ($\times 10^3 Kg$), and the whole year ($\times 10^9 Kg$) of 1994, as labeled. The thick solid line is $(LI)_p$, the difference between the 2 terms on the RHS of (3.7), which was used to calculate I_1; thin solid line is $(AI)_p$ used to calculate I_2; and dashed line was obtained by calculating only the first term on the RHS of (3.7).

Table 3.1: Comparison of line and area integrations from 00:00GMT January 01 to 12:00GMT December 31, 1994 in MRB, in the unit of m^3

name	I_1	I_2	I_3
value($\times 10^{11}$)	5.13	4.54	3.69

$0.59E11m^3$, representing the error due to different calculations of the same quantity because these two methods should give identical results theoretically. The difference between I_1 and I_3 is $1.44E11m^3$, representing the effects of topography. Comparison of I_3 with I_1 is more useful for the purpose of this study because, as mentioned above, Method 3 for I_3 cannot completely include the topographic effects as in Method 1 for I_1. This concludes that Method 3 is most "buggy".

Therefore, when using Green Theorem to calculate flux divergence over complex topography, one should, as in Method 1, carry out line integration along both outer and inner boundaries and subtract the inner line integration from the outer line integration on the calculation level.

3.2.4 Summary

When calculating the total horizontal moisture flux divergence in an air column over complex terrain, Green Theorem should be used only on each level in the vertical. And the inner line integral has to be subtracted from the outer line integral if there are mountains intercepting the lower levels. If calculating only the line integral along the outer boundary, one is violating Green Theorem and cannot completely include the effects of topography. Results of calculations using NCEP/NCAR reanalysis data

demonstrate this conclusion.

3.3 The Numerical Model

The runoff parameterization to be verified is the one included in Bonan's Land Surface Model (LSM) Version 1.0 (Bonan 1996b). This LSM is a blend of the ecological processes found in many ecosystem models, hydrological processes found in many hydrologic models, and the surface fluxes common to the land surface models used with atmospheric models. Our interest in this study is in hydrological processes in this study. A detailed description of the hydrological component in the LSM can be found in Chapter 2 and Bonan (1996b).

An on-line method was chosen to perform the verification, i.e., the LSM was coupled to a GCM. NCAR's Community Climate Model version 3 (CCM3) (Jeffery et al. 1996; Thomas et al. 1996) was used as the AGCM in the current study. For a detailed description of these two models, readers are referred to the corresponding reference mentioned above. Briefly, CCM3 is a spectral general circulation model which is, in this study, configured at T42 resolution (approximately 2.8° × 2.8° transform grid). This model has 18 vertical levels with the model top at 2.9hPa. It uses prescribed climatologically varying sea surface temperature (SST), prescribed surface albedos, and prescribed surface wetness. Radiation calculations are only performed every model hour. CCM3 uses a 20-min time step and the coupled LSM use a 10-min time step.

3.3.1 Initial and Boundary Conditions

Initial and boundary data sets used for the current study are listed in Table 3.2. All data sets were downloaded from NCAR's anonymous ftp site. Interested readers are referred to the README files for the data sets on NCAR's anonymous ftp site. The

Table 3.2: Initial and boundary data sets for the T42 CCM3/LSM models

Model	Initial Conditions	Boundary Conditions		
		time-invariant (Topo)	time-variant (SST)	time-invariant (ozone)
CCM3	SEP1.amip.T42 .0596	tibds.T42.0596	T42.Dec1949 -May1995	ozn.T42.0596
LSM	None	SURFDAT.T42.0596		

current verification is based on T42 CCM3/LSM runs because the T42 resolution represents a 2.8° × 2.8° horizontal grid system, which is the closest to the 2.5° × 2.5° resolution used for the NCAR/NCEP reanalysis data. This allows the best comparability between the diagnosed and the model results while requiring reasonable computing resources.

SEP1.amip.T42.0596 is the initial dataset for CCM3. SEP1 means this data climatologically represents the condition on September 1. The exact year for the simulation will be determined by the prescribed Sea Surface Temperature (SST) data named as T42.Dec1949-May1995, which contains the monthly mean of SST from December 1949 to May 1995 with 12 monthly means per year. But for this study, we only use a 10-year period from September 1984 to December 1994 because data at hand for diagnosed analysis begins with the year 1987. Therefore the total length of the model simulation is 10.5 years with the first 2.5 years as the spin-up for the CCM3/LSM. The remaining 8-year simulation result will be used for our analysis, i.e. from January 1987 to December 1994.

The time-invariant boundary condition data tibds.T42.0596 contains the standard deviation of topography. And ozn.T42.0596 contains the climatological monthly means for 12 months. The model will reuse this ozone data for 12-month loops.

The boundary condition file for the LSM, SURFDAT.T42.0596, contains the latitude, longitude, surface type, soil color, percent sand, percent silt, percent clay, percent lake, and percent wetland. Arbitrary initial conditions was used for the LSM because, according to Bonan (1996a), for long time simulations, there is not much difference between runs with and without the assumption of specific initial conditions.

3.3.2 CCM3/LSM Runs

The model simulation starts on September 01, 1984. After the first 1-day initial run, a 486-day restart run and a 1-year restart run finished the 2.5-year spin-up run on January 01, 1987, the starting time of our NCEP/NCAR reanalysis data. Then, eight 1-year runs were completed for verification of the runoff parameterization.

3.4 The Verification Results

Verification was conducted at a global scale and in 5 major basins over the world, the Mackenzie River basin and the Mississippi River basin in North America, the Amazon River basin in South America, the ALPS mountains area in Europe and the Yangtze River basin and the Tibet Plateau area in Asia. Concerning the length of the thesis, only the results in the Mackenzie River basin and the Mississippi River basin will be shown in detail. However, brief descriptions of the other basins will be provided in the section discussing global scale verification. In this section, results will be presented in an order of descending scale, i.e., beginning with the global view, and thereafter focusing upon a more detailed discussion of the results for North America

and, finally in even greater detail on the Mackenzie River Basin itself.

Before discussing the verification, annual averages of typical variables (including runoff) for our 3-year, 4-year, 5-year, 6-year, 7-year and 8-year results were compared at both global and basin scales. I found there is little difference among the annual averages of 3-year, 4-year, 5-year, 6-year, 7-year and 8-year results. This indicates that the model is climatologically stable and that the 8-year period is long enough to enable the verification to be performed.

3.4.1 Verification Results at the Global View

The 8-year integrated diagnosed runoff presented in Figure 3.4 has a very familiar horizontal distribution pattern. There is a high band around the equator with low bands at its north and south sides. This implies that at the equator, precipitation exceeds evaporation. This pattern is consistent with many previous results, such as those of Oki et al. (1995) based upon ECMWF reanalysis data and of Trenberth and Guillemot (1996) based upon NCEP/ NCAR reanalysis data. It is also consistent with classical results for global climatology (Gill 1982a).

In terms of hydrology, there is, of course, no runoff over oceans or other water covered regions. Therefore, hereafter, we will discuss only the results over land.

The absolute values of the extremes range from several to 20 meters in Figure 3.4, that is to say the annual runoff has a maximum of 250cm. In Figure 3.4, extremes can be found at major river basins. The most significant one is in the Amazon River Basin with a high of 18.38m for the 8-year time integrated runoff. There is another high of over 12m just to the south of the Amazon River Basin at the east side of the Andes Mountains, and one more high of over 8m at the east side of the Andes Mountains at the south-most point of South America. In North America, the diagnosed result gives a most significant of 13.86m at the west coast around the border between the US and

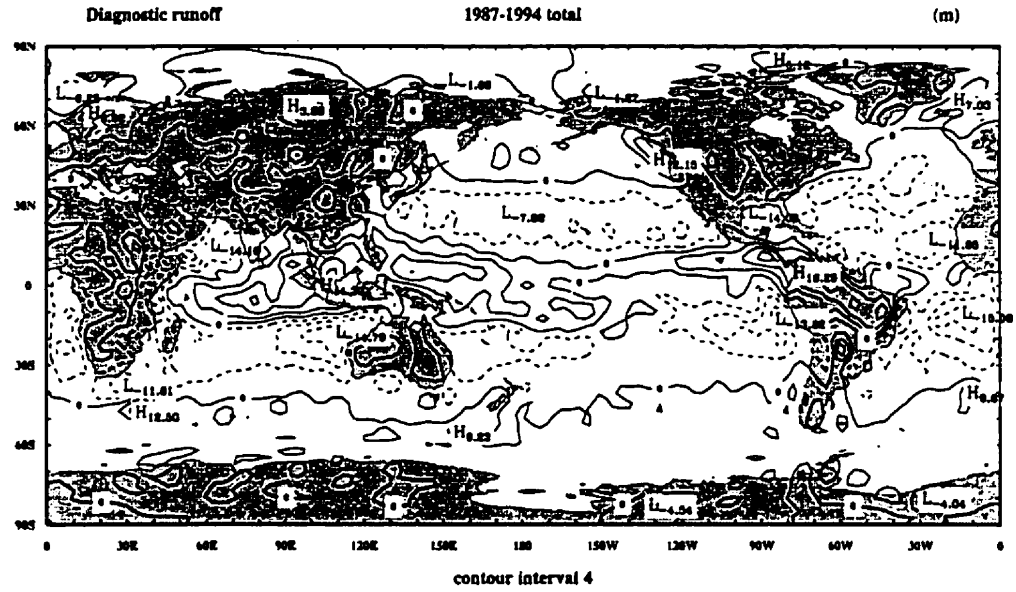

Figure 3.4: 8-year accumulation of diagnosed runoff(m) at a global view.

Canada. This one is at the western side of the Rocky Mountains and is associated with strong moisture convergence by the local weather system. Actually, there are also high bands along the east side of the Rocky Mountains at the Mackenzie River Basin and the Mississippi River basins, but they do not show up in this global view because of the relative high values elsewhere. They will be discussed in details later.

In Africa, to the south of the desert region in the North Africa, there is a high band in the central part of the whole African region along the river systems such as Nile, Congo, and Zambezi, etc. The highest runoff of over 4m is diagnosed at the tropical rainforest region in Central Africa. There are also 3 more highs at Nile in Sudan, Central African Public and South Angola.

In Asia, a high over 8m was diagnosed in India and a high over 4m is located at the Sichuan basin in China. Very weak runoff was diagnosed for Australia.

Next, let us take a look at the CCM3 T42 simulated runoff at a global view (Figure 3.5). At an overall look, the model can reproduce the horizontal distribution pattern

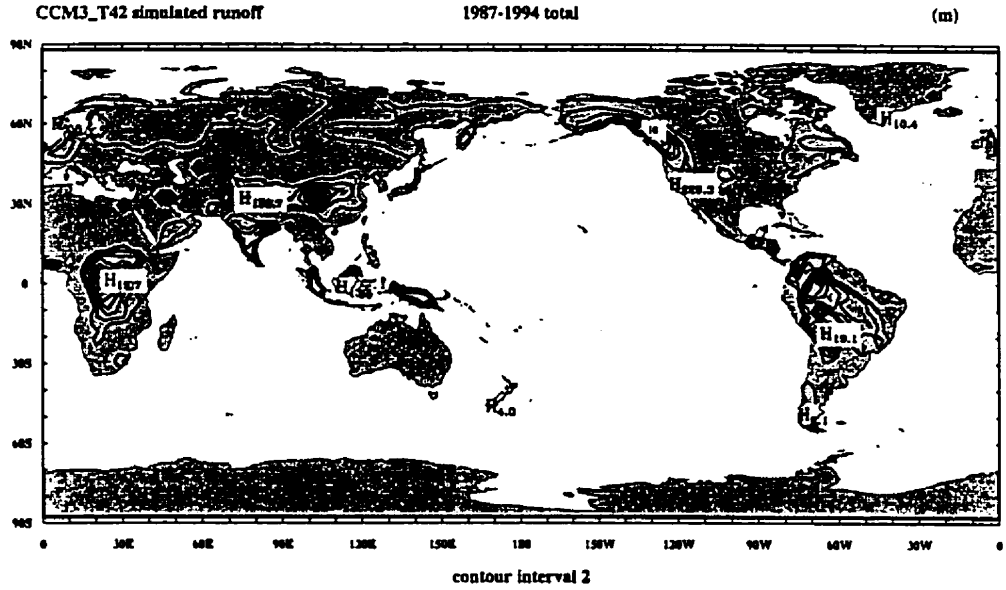

Figure 3.5: 8-year accumulation of the original CCM3/LSM simulated runoff(m) at a global view.

of the diagnosed runoff over land. The model does not produce runoff over water. It can generate high runoff bands at most major basins. The model produced a 13.7m high at the west coast of North America around the US and Canada borders. The difference from the diagnosed high is, the model-generated center is located over land but the diagnosed one is a little bit shift to the west and over the sea. At Amazon River Basin, a high of over 24m was generated by the model at the similar location as in the diagnosed result with a value of 18.36m. The other 2 highs in South America have values of 19.1m and 8.1m corresponding with the diagnosed 12m and 8m. But detailed analysis shows that the locations of the model-produced highs are located closer to the mountain tops. In Africa, a high band at the similar location as in the diagnosed result was obtained at the central part of Africa with a value of 15.7m. In Asia, a high over 12m in India and a high band along the Yangtze River with a maximum of 196.7m at Sichuan Basin, China can be observed in the modeled runoff.

There are also some weaker highs over the islands between Asia and Australia.

According to the above discussion, the model can generate the overall pattern of the diagnosed runoff. Relative high runoff bands agree well between the diagnosed and modeled results in most of the regions. But, obviously, the model generally overestimates the runoff in nearly all regions, and even gives wrong runoff in Sichuan Basin, China with a value of 196.7m, and at another point at the west coast of the US with an unreasonably large value of 229.3m.

To better verify the parameterization, detailed comparisons will be done at smaller scales at 2 regions, the North America and the Mackenzie River Basin. Comparison will be made for either basin scale area integrals, same as in other previous studies, or for horizontal distribution which is more important for the verification and model climates, or both.

3.4.2 Detailed Verification Results in North America

The diagnosed and modeled runoff in North America is shown in Figures 3.6 and 3.7 respectively. To retain more realistic information, weaker smoothing (5-point smoothing) was done on the diagnosed results for this region. That is why the absolute values of the diagnosed extremes are larger than in the global view in last section. This will not affect our conclusions.

In this closer look at the diagnosed result in North America, one can see an over-4m high bands between the Rocky Mountains and the MRB, Canada and in the Mississippi River Basin at the east side of the Rocky Mountains, the US. Another high in Mackenzie River Basin is at its bottom, around the Great Slave Lake, with a value of over 8m. While, in the modeled runoff (Figure 3.7), even the contours were drawn with a interval of 1m, still no high bands were caught between the Rocky Mountains and the Great Bear Lake, or at the basin bottom in Mackenzie River

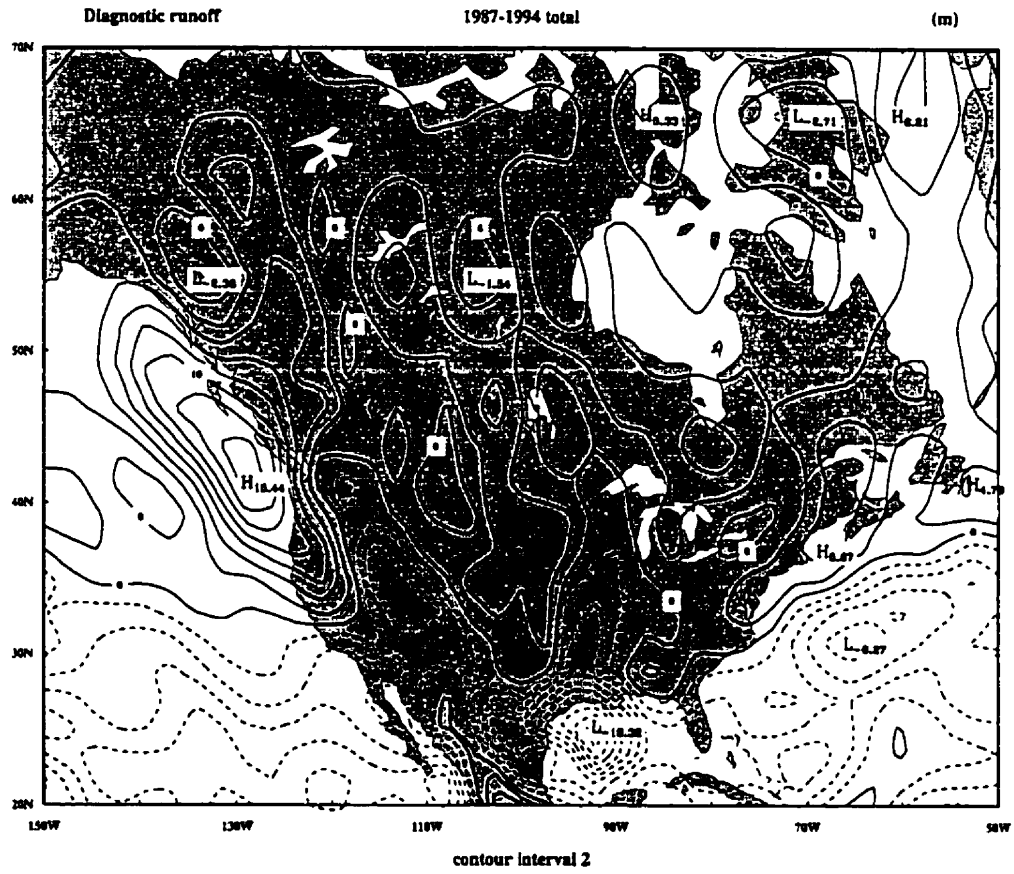

Figure 3.6: 8-year accumulation of diagnosed runoff(m) in North America.

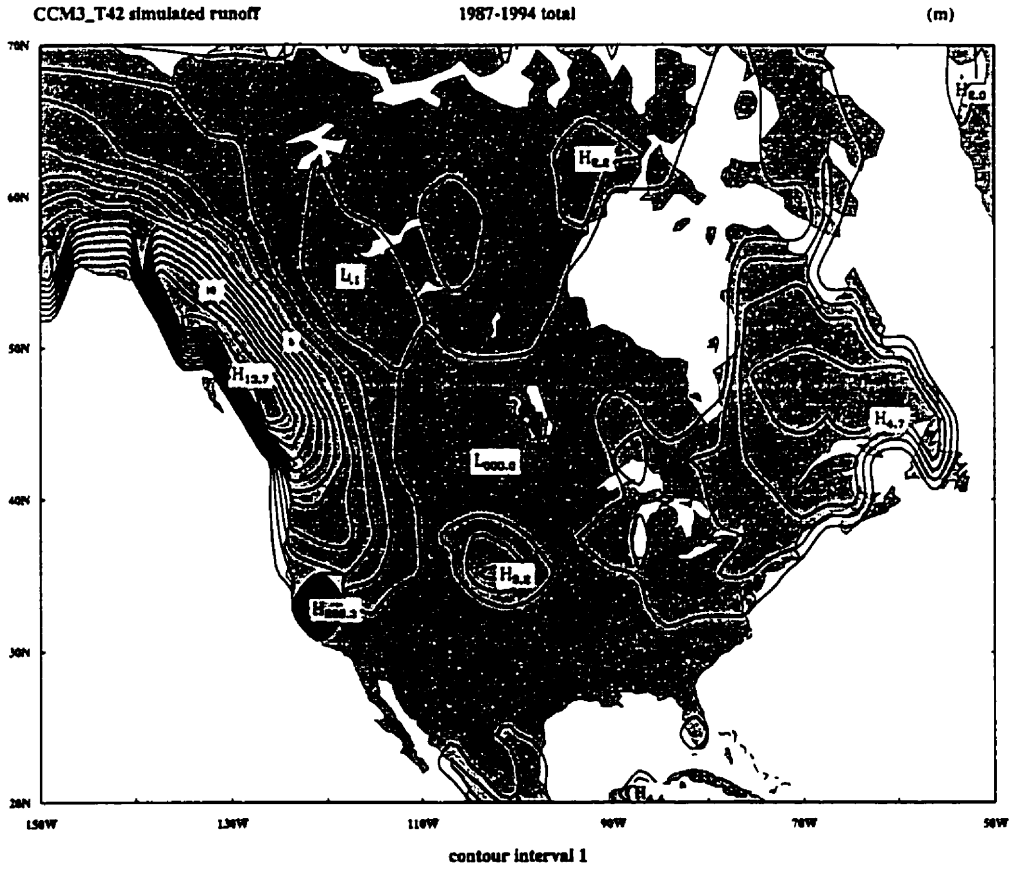

Figure 3.7: 8-year accumulation of the original CCM3/LSM simulated runoff(m) in North America.

Basin. On the contrary, a low of 0.1m was produced by the model at the bottom of the MRB. A 3.2m high can be observed in the Mississippi River Basin corresponding with the over-4m high in the diagnosed result. Obviously, the model underestimated the runoff over these regions.

The high bands at the maritime agree well between the diagnosed and the modeled runoff.

If looking the diagnosed runoff in Figure 3.6 from west to east, one can find there is a sort of oscillation. This is probably the Gibbs oscillation (Pinsky 1991) caused by topography, which can be seen also in other basins.

3.4.3 Detailed Verification Results in the MRB

The most detailed discussion is in the MRB because this study was first proposed for the Mackenzie Area GEWEX Study (MAGS)(Krauss 1995). Discussion in this section will be focussed on two aspects, the basin scale area integrals of runoff and the horizontal distribution of runoff in the MRB.

The 8-year CCM3 simulation results are consistent with Bonan (1996a) in terms of area integrals of runoff (comparing the last 2 columns in Table 3.3). Comparison between the diagnosed and simulated runoff indicates that the area integration of model simulated runoff rate ($m^3 s^{-1}$) and accumulated runoff (m^3) in the MRB are very close to the diagnosed results from NCEP/NCAR reanalysis data in the same region. From Table 3.3, one can also find, in terms of the annual time-integrated runoff, our model result is $5.5 \times 10^{11} m^3/year$, which is very close to Bonan's result, is $5.2 \times 10^{11} m^3/year$. Liu et al (2001) also concluded for the 1994-1995 water year that the area integrals of the diagnosed runoff are in very good agreement with previous results by using other observational data in the Canadian GEWEX study area (Stewart et al 2001).

Table 3.3: Comparison between diagnosed and CCM3/LSM simulated runoff in the MRB, area integrals

Items compared	Diagnosed	LSM/CCM3 simulated	
		Cho and Liu(2001) (8-year run)	Bonan(1996a) (5-year run)
Averaged Runoff rate ($m^3 s^{-1}$)	19134.88	17692.11	16645.00
Total runoff ($\times 10^{12} m^3$)	4.83	4.40	2.59 *

* This number was calculated according to the averaged runoff rate in Bonan's paper (Bonan 1996a)

Horizontal distribution of runoff is much more important than the area-integration (a single number) to verify a model. Diagnosed and simulated horizontal distributions of runoff in MRB are shown in Figures 3.8 and 3.10 respectively. When comparing Figures 3.8 and 3.10, one can easily conclude that, the diagnosed horizontal distribution pattern of runoff is reasonable with a high band between Rocky Mountains and the Great Bear Lake, and another over the Great Slave Lake at the bottom of the MRB. This diagnosed runoff horizontal distribution pattern is also very similar with the observed (Figure 3.9) in this area (Matthews and Morrow 1995). Again, possible Gibbs oscillation exists in Figure 3.8. If drop the negative band caused by Gibbs oscillation, the whole MRB is dominated by positive runoff in the diagnosed result with high bands between the Rocky Mountains and the Great Bear Lake, and at the basin bottom.

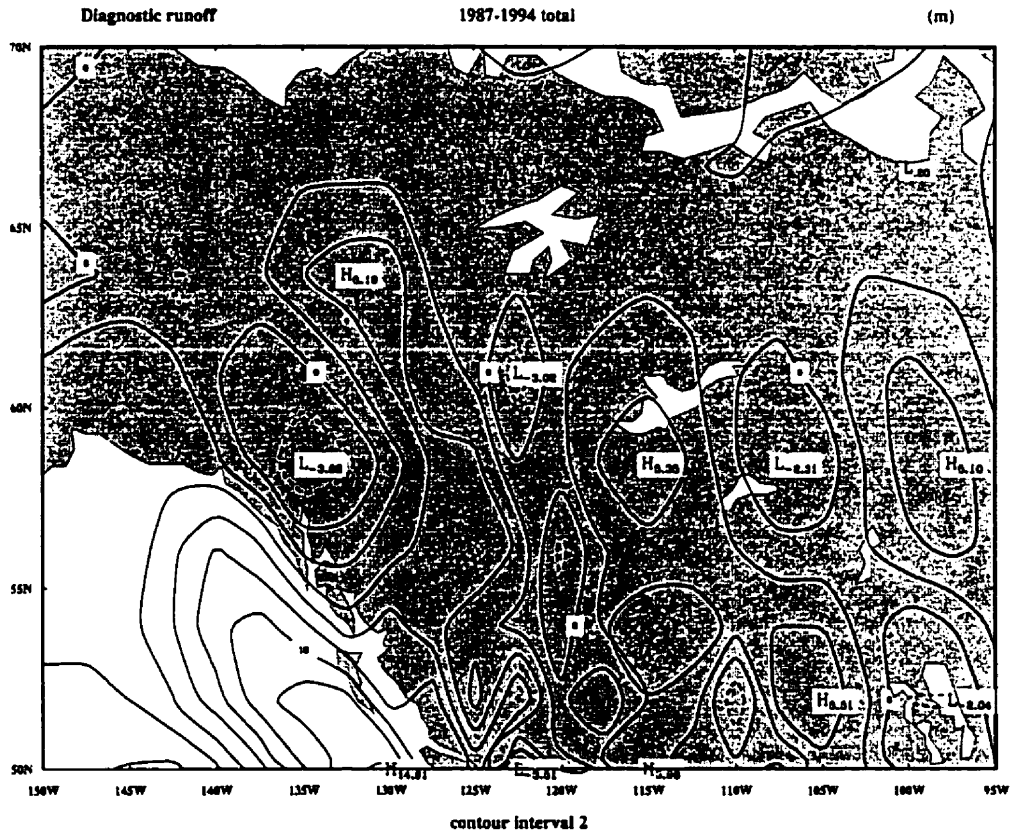

Figure 3.8: 8-year accumulation of diagnosed runoff(m) at the MRB.

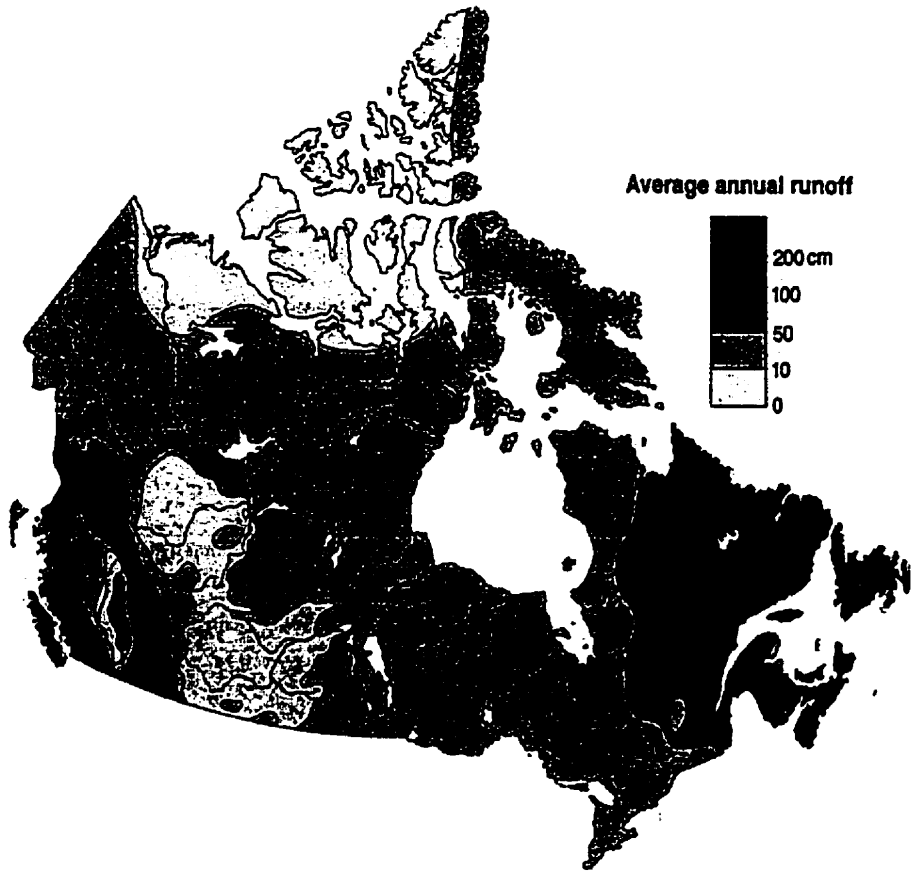

Figure 3.9: The observed average annual runoff (cm) over Canada. (Courtesy of Matthews and Morrow 1995)

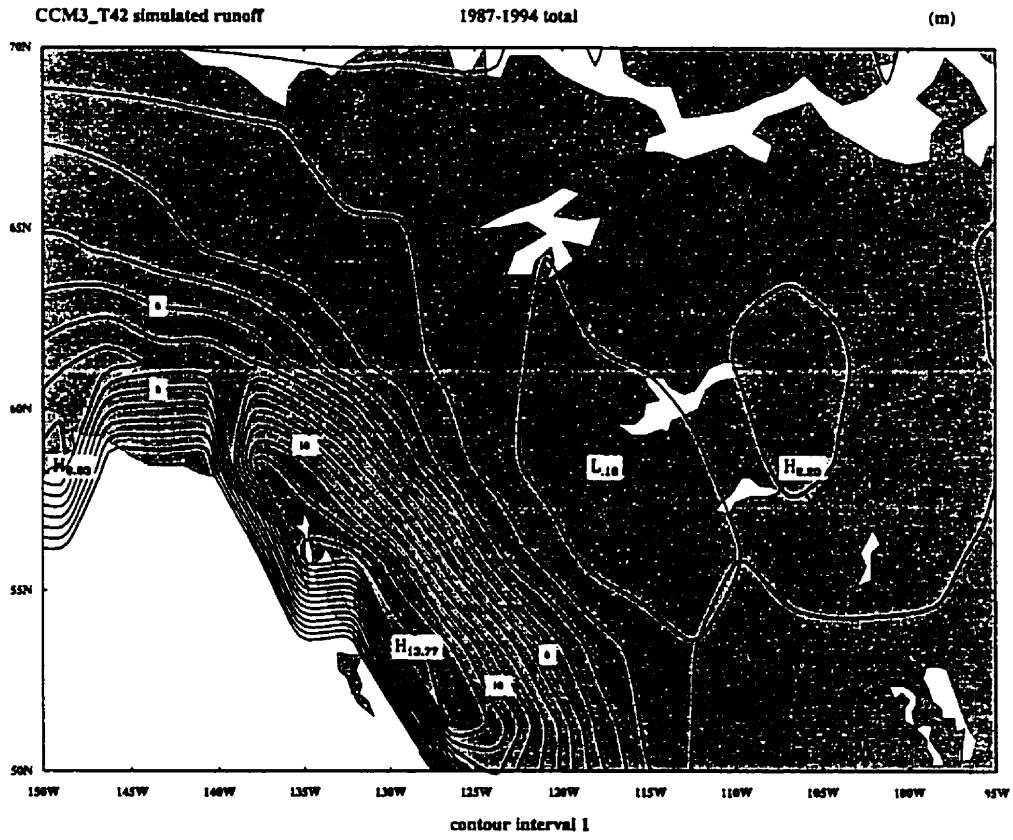

Figure 3.10: 8-year accumulation of the original CCM3/LSM simulated runoff(m) at the MRB.

On the contrary, the current runoff parameterization in LSM/CCM3 cannot generate the observed horizontal distribution pattern of runoff, and even, gives an unreasonable horizontal distribution at least in the MRB because, (1) the model gives a minimum runoff center over the Great Slave Lake, where there is a maximum center in the diagnosed result; (2), the model did not produce any high band between the Rocky Mountains and the Great Bear Lake. This is very unlikely.

Figure 3.11 shows the difference between the simulated and the diagnosed runoff in the MRB. Obviously, the current runoff parameterization underestimated runoff between the Rocky Mountains and the Great Bear Lake, and over the Great Slave Lake at the bottom of MRB. Again, if we drop the possible Gibbs oscillation mentioned above, the current runoff parameterization underestimated the runoff in the whole MRB. After comparing our results and the topography in MRB (Figure 3.12), and understanding the current runoff parameterization, one can conclude that the unreasonable horizontal distribution pattern of runoff from the model is possibly due to its exclusion of topographic effects. Lateral water fluxes caused by topographic slopes not only affect the horizontal redistribution of runoff, but also directly affects the infiltration capacity of the soil. Modification on these 2 aspects is expected to improve the runoff parameterization on simulating the horizontal distribution pattern of runoff, and thus improve the AGCM simulated model climate.

3.5 Summary – A Problem of the Current Scheme

Diagnosed runoff was estimated from NCEP/NCAR reanalysis data for an 8-year period from 1987 to 1994. Bonan's LSM was run for the same period coupled to NCAR's CCM3. Comparisons between the diagnosed and simulated runoff from the model indicate that, at a global view, the runoff parameterization can reproduce the

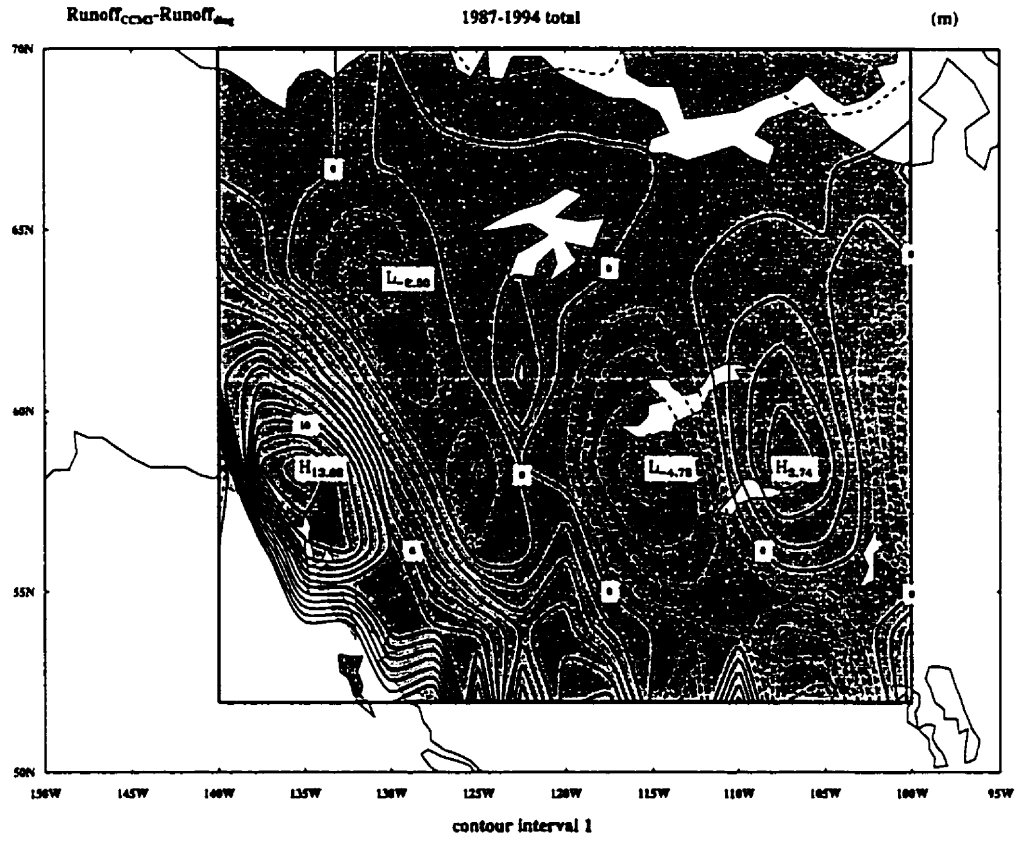

Figure 3.11: Difference between the 8-year accumulations of simulated and diagnosed runoff (m) in the MRB: $R_{CCM3} - R_{diagnosed}$.

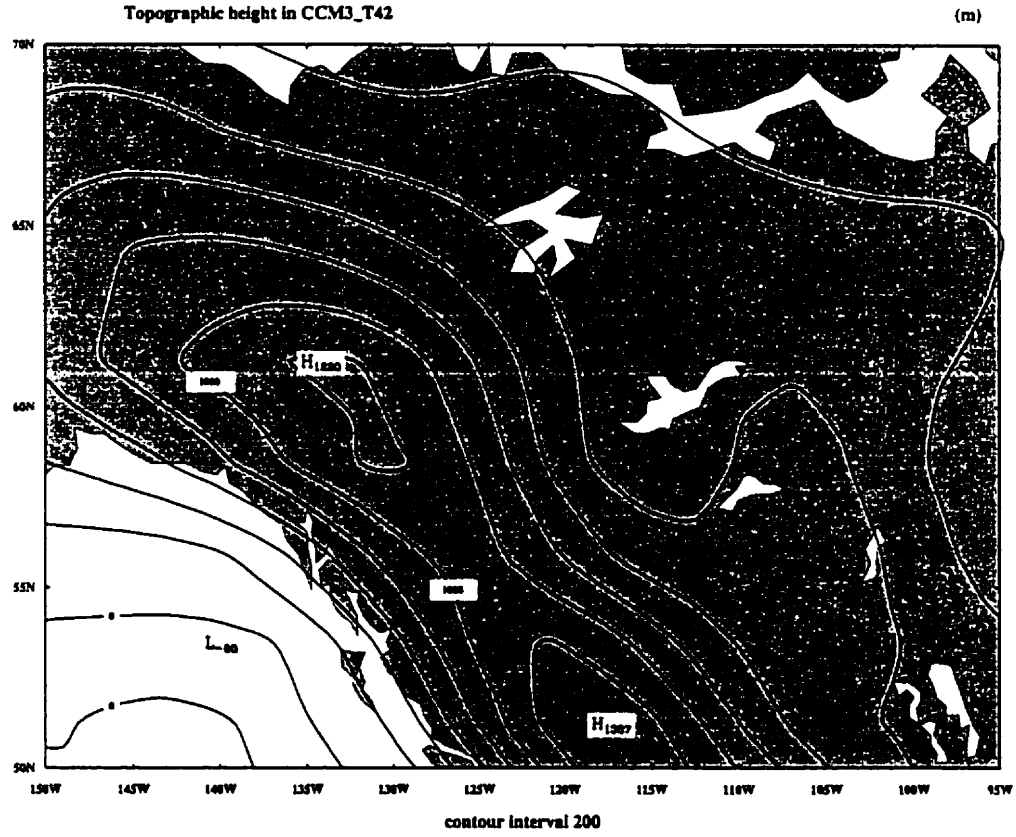

Figure 3.12: Topographic height (m) in the MRB resolved by the CCM3 with T42 resolution.

general horizontal distribution pattern of the diagnosed runoff but with substantial overestimates in some regions and underestimates in others. Closer look at the North America and the MRB shows that, the area integrals of runoff are fine in the MRB, but the runoff parameterization cannot reproduce the reasonable diagnosed horizontal distribution of runoff, which is more important to the model climate. One of the possible reasons is that topographic effects are not included in the current runoff parameterization. Lateral water fluxes caused by topographic slopes not only affect the horizontal redistribution of runoff, but also directly affects the infiltration capacity of the soil. Modification on these 2 aspects is expected to improve the runoff parameterization on simulating the horizontal distribution pattern of runoff, and thus improve the AGCM simulated model climate.

Theoretically, negative runoff is possible, actually, in climatology, at most of the time, evaporation is larger than precipitation, and then according to our approximation in section 3.1, there will be negative runoff. But the current LSM does not allow negative runoff. This is not consistent with theory. Modification of the runoff parameterization will also allow negative runoff in the model.

Another finding in this chapter is that, possible Gibbs oscillation exists in both the NCAR/NCEP and the ECMWF reanalysis data. This is also found in other places such as Mississippi River Basin and South America.

Chapter 4

Modification on Bonan's Runoff Parameterization

4.1 Effects of Topography on Surface Water Redistribution

4.1.1 A Qualitative Explanation

As concluded in last chapter, Bonan's runoff parameterization scheme does not include the topographic effects which are very important to the surface water redistribution and soil moisture, and thus very important to both the land surface climate and the AGCM climate. The topographic effects on the redistribution of surface water are illustrated in Figure 4.1.

The remained water on the ground surface from precipitation and snowmelt is divided into three parts: evaporation back to the atmosphere, infiltration into the soil, and surface runoff into rivers and lakes. Here we emphasize on the impact of topographic slopes on surface runoff and infiltration. Obviously, water redistribution

is also greatly affected by vegetation and soil type. This study assumes that these effects are already treated properly.

Changes in infiltration will also change soil moisture and thus the evaporation. This chain reaction will change the AGCM climate starting with the change in surface evaporation as described in the next chapter.

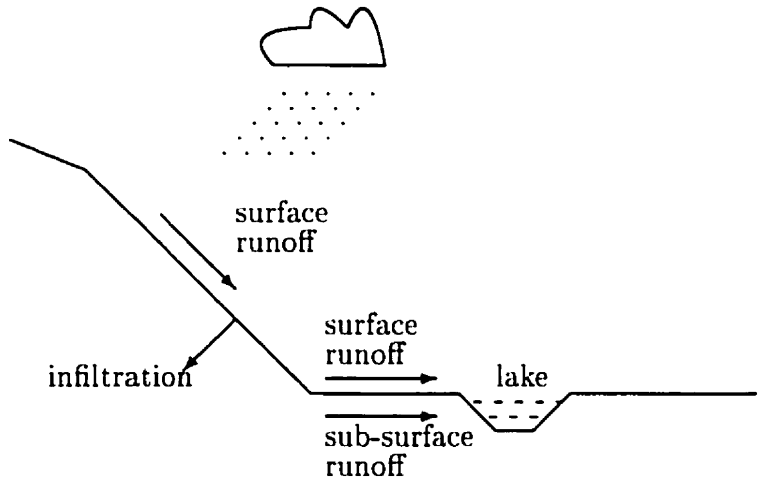

Figure 4.1: Schematic showing the effect of slope.

As shown in Figure 4.1, the steeper the slope, the more difficult for the precipitation water to stay on the slope, the less opportunity for the water to infiltrate into the soil. Therefore, qualitatively, topographic effects should be very important to the runoff redistribution and thus to the AGCM climate.

4.1.2 Quantitative Formulation

First of all, we will determine the lateral water fluxes caused by topography. For a given grid cell in the model (Figure 4.2), differences in topography between neighboring grid cells will result in lateral inflows or outflows in every possible direction. For simplicity, only the four main directions will be considered in this study. Subscripts of the water flow F: N, S, E and W represent the four main directions: north, south, east and west, respectively; subscripts i and o denote inflow and outflow, respectively; or for simplicity, we can used F_1, F_2, F_3 and F_4 to represent the net lateral fluxes caused by topography in the four main direction.

With the consideration of lateral water fluxes caused by topography, the newly proposed surface runoff rate q_{over} and infiltration rate q_{infl} should be calculated by

$$q_{over} = q^*_{over} + q_{flux} \tag{4.1}$$

$$q_{infl} = q^*_{infl} + q_{flux} \tag{4.2}$$

where q^*_{over} and q^*_{infl} are the surface runoff rate and infiltration rate calculated by the original Bonan's land surface scheme; q_{flux} is the lateral water flux caused by topography. It is determined by the next expression

$$q_{flux} = \nabla \cdot \vec{F} \tag{4.3}$$

where

$$\vec{F} = (F_2 + F_4)\vec{i} + (F_1 + F_3)\vec{j} \tag{4.4}$$

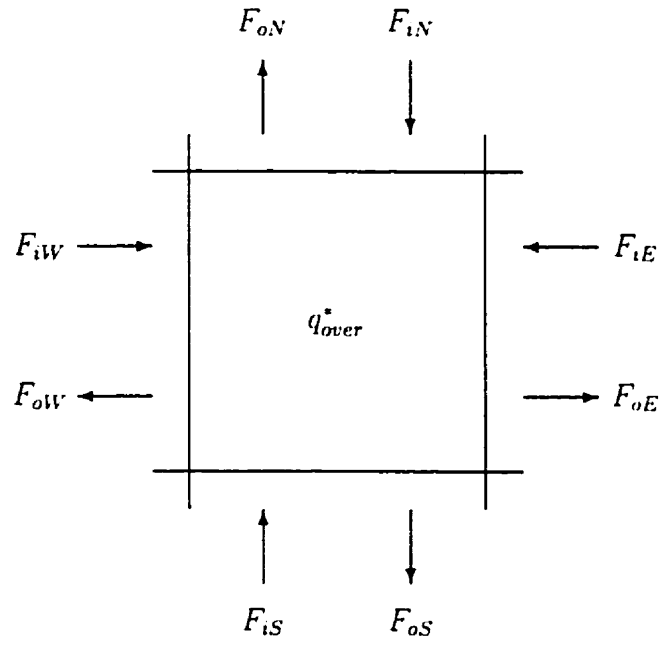

Figure 4.2: Schematic showing the lateral water fluxes in the main 4 directions. The lowercase subscripts i and o denote inflow to and outflow from the local grid cell, respectively. The uppercase subscripts W, E, S and N represent the four main directions *west*, *east*, *north* and *south*, respectively. The net lateral fluxes in (4.4) are defined as: $F_1 = F_{iN} - F_{oN}$; $F_2 = F_{iW} - F_{oW}$; $F_3 = F_{iS} - F_{oS}$ and $F_4 = F_{iE} - F_{oE}$.

if using F_k to represent the net water fluxes in each of the four main directions, with A as the area of the grid cell concerned. In one direction, only one of the inflow or outflow is possible at a given time.

Miller(1994), Coe(1998) proposed an expression for the outflow in his river routing model as, in one direction,

$$F_k = max[(WE_l - WE_d)A, 0]\frac{u}{d} \tag{4.5}$$

where WE_l and WE_d are the water elevations of the local grid cell and the downstream grid cell, respectively; d is the grid size, and u is the flow speed between neighboring grid cells defined as

$$u = 0.35\sqrt{\frac{s}{s_0}} \tag{4.6}$$

here s is the slope determined by the elevation difference ($\triangle z$) between neighboring grid cells and the grid distance d (Figure 4.3). s_0 is called critical slope and set to a constant of 0.00005. The constants s_0 and 0.35 depend on the horizontal resolution of the model and were chosen more empirically than physically (Miller 1994). In the current study, as a result of our many experiments, 0.35 has been changed to 0.0035 to allow $0.15 < u < 5$ (Miller 1994; Coe 1998). This empirical condition helps to restrict the lateral water fluxes to a proper magnitude.

In previous studies (Miller 1994; Coe 1998), the above equation was used to calculate outflows only. According to this equation, the outflow from the local grid cell to the downstream grid cell is determined by two factors: 1) the local water elevation WE_l must be larger than the downstream water elevation WE_d, otherwise, no outflows; 2) if condition 1) is satisfied, the magnitude of outflows will also be controlled by the ratio of the slope-determined u and the downstream distance d (grid size).

However, inflows and outflows are relative to the grid cells discussed. In magnitude, outflows from the local grid cell to the downstream grid cell is actually, on the

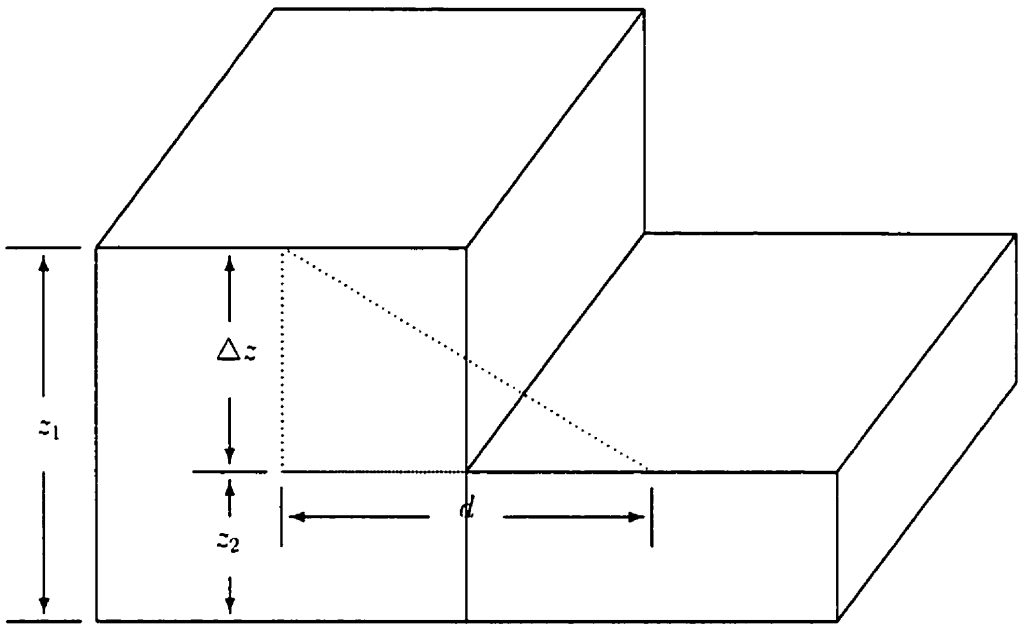

Figure 4.3: Schematic showing the calculation of slope between neighboring grid cells. Plotted are two neighboring grid cells in the CCM3/LSM, with z_1 as the topographic height of the left grid cell, and z_2 of the right hand side grid cell; $\Delta z = z_1 - z_2$ is the difference in topographic height between this two grid cells. The slope s is calculated in the dotted triangle with Δz and d as its two sides, i.e., $s = \Delta z/d$.

contrary, inflows to the downstream grid cell from the local grid cell. Therefore, the above equation should apply to not only outflows, but also inflows. In this study, the above equation is modified to

$$F_k = \begin{cases} ABS[(WE_l - WE_d)A]\frac{u}{d} & \text{outflow, when } (WE_l - WE_d)A > 0 \text{ and } u > 0 \\ ABS[(WE_l - WE_d)A]\frac{u}{d} & \text{inflow, when } (WE_l - WE_d)A < 0 \text{ and } u < 0 \\ 0 & \text{no fluxes, in other cases} \end{cases}$$

where sign ABS represents the absolute value of the bracket. The magnitude of inflows or outflows will be determined by the difference of water elevation and the ratio of u and d. The nature of the lateral water flux (inflow or outflow) is determined by u or the topographic height. When water elevation of the local grid cell is larger than that of the downstream grid cell, and the local grid cell has higher topography, i.e. $u > 0$, there will be outflows from the local to the downstream grid cell; when water elevation of the local grid cell is smaller than that of the downstream grid cell, and the local grid cell has lower topography, i.e. $u < 0$, then there will be inflows to the local from the "downstream" grid cell; There is no lateral water fluxes in other cases.

Keeping in mind that u controls the nature of the lateral water fluxes, i.e., inflow or outflow, the above equation set can be simplified to one equation for both inflows and outflows, as

$$F_k = ABS[(WE_l - WE_d)A]\frac{u}{d} \tag{4.7}$$

In equation (4.7), the value of the square bracket is actually the area integral of the water elevation difference between the local and the downstream grid cells. In the current study, the grid cell area is not a constant. Therefore a more precise form of equation (4.7) is

$$F_k = ABS[(WE_lA_l - WE_dA_d)]\frac{u}{d} \tag{4.8}$$

Water elevation WE is defined as the summation of the water depth h and the land elevation z as in Hornberger et al. (1998), i.e. $WE = h + z$. Then, Equation (4.8) can be rewritten as

$$F_k = ABS[(h_l A_l - h_d A_d) + (z_l A_l - z_d A_d)]\frac{u}{d} \tag{4.9}$$

or

$$F_k = ABS[\Delta(hA) + \Delta(zA)]\frac{u}{d} \tag{4.10}$$

where $\Delta(hA)$ and $\Delta(zA)$ denote the difference of area-integrated water depth and land elevation, respectively, between the local and downstream grid cells.

The water depth difference between the local and the downstream grid cells, $\Delta(hA)$ can be related to the time-area-integrated surface runoff R^* from the original model, i.e. surface runoff is the main factor to change the water depth h in its grid cell. The water depth of a studied grid cell can be expressed as

$$h = \frac{R^*}{A} \tag{4.11}$$

where R^* is defined by the model-generated surface runoff rate q^*_{over} (mms^{-1} in the model and ms^{-1} in this calculation) as

$$R^* = \int_{model\ time}\int_{over\ the\ grid\ cell} q^*_{over} dA dt \approx q^*_{over} A t \tag{4.12}$$

where t is the total model time up to the point of the adjustment. So we have the water depth difference between the local and the downstream grid cells as,

$$\Delta(hA) = \frac{R^*_l}{A_l}A_l - \frac{R^*_d}{A_d}A_d = R^*_l - R^*_d = [(q^*_{over})_l A_l - (q^*_{over})_d A_d]t \tag{4.13}$$

where the subscripts l and d denote local and downstream, respectively. Therefore, in one main direction, the lateral water flux rate to/from the local grid cell ($m^3 s^{-1}$) is

$$F_k = ABS[(q^*_{over})_l A_l - (q^*_{over})_d A_d]t + [z_l A_l - z_d A_d]\frac{u}{d} \tag{4.14}$$

After F_k is calculated in all of the four main directions, the net lateral water flux rate for the grid cell, q_{flux} (mms^{-1}), can be estimated by equation (4.4). Finally, the surface runoff rate q^*_{over} (mms^{-1}) and the infiltration rate q^*_{infl} (mms^{-1}) generated by the original model are adjusted accordingly to their new values q_{over} and q_{infl} respectively in the modified model by equations (4.1) and (4.2).

4.2 Implementation of the Modified Scheme

4.2.1 The Simple Numerical Regime in Bonan's LSM

Bonan's LSM is a very comprehensive model in terms of physics processes. But its numerical regime is very simple. It is actually a single-point one-dimensional model because it does not have any consideration of the interaction between neighboring GCM/LSM grid cells. All calculations are on its 6009 so-called subgrids.

At the beginning of the LSM run, the initial conditions are interpolated from a 128×64 regular horizontal grid system onto the 6009 irregular predefined land points, or subgrids. During the LSM integration, the model integrate and solve any equation for the 6-layer soil model point by point(of the 6009 points). When the model is asked to output, variables are again transferred onto the regular 128×64 grid system, by using gaussian weighted summation.

4.2.2 Implementation of the New Scheme

For simplicity, the implementation of the modification will follow the original numerical regime. No effort has been made to modify the numerical algorithm. A subroutine (named slp.f) was plugged into the model as seen in the flow chart(Figure 4.4) to do the adjustment of runoff and infiltration caused by topography. Functions of the subroutine slp.f are illustrated in Figure 4.5.

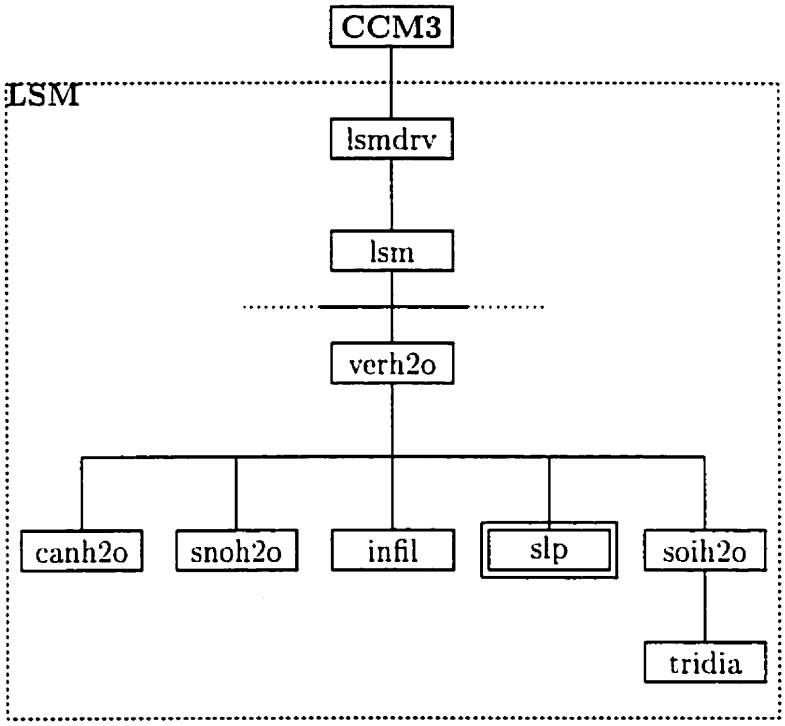

Figure 4.4: Flowing chart showing where the subroutine slp.f is plugged in.

In Figure 4.4, the big dashed frame encloses the primary subroutines related to the hydrological processes. Strings in the frames are subroutine names. The AGCM CCM3 calls Bonan's land surface model(LSM) every time step. Subroutine **lsmdrv.f** is called first by CCM3 to drive the LSM. Subroutine **lsm.f** is the main routine for LSM. Subroutine **canh2o.F** calculates canopy water: **snoh2o.F** calculates snow water: **infl.F** calculates surface runoff q_{over} and infiltration q_{infl}; **slp.F** adjusts q_{over} and q_{infl} according to the calculated lateral water fluxes caused by topography; and the adjusted q_{over} and q_{infl} are passed to subroutine **soih2o.F** to calculate soil water and sub-surface runoff / drainage by solving a tridiagonal system of equations.

As shown in Figure 4.5, subroutine **slp.F** commits several tasks. It reads in the topographic height first, which is used to calculate the slopes s between neighboring grid cells. Then flowing speeds u in the four main directions are estimated by Equation (4.6). After the water elevation difference dWE is determined, if u and dWE have the same mathematical signs, then inflow or outflow rate q_{flux} is calculated; otherwise there is no outflow from or inflow to the local grid cell, i.e., $q_{flux} = 0$. Finally, the surface runoff rate q_{over} and infiltration rate q_{infl} are modified by the calculated lateral water flux rate q_{flux} according to equations (4.1) and (4.2).

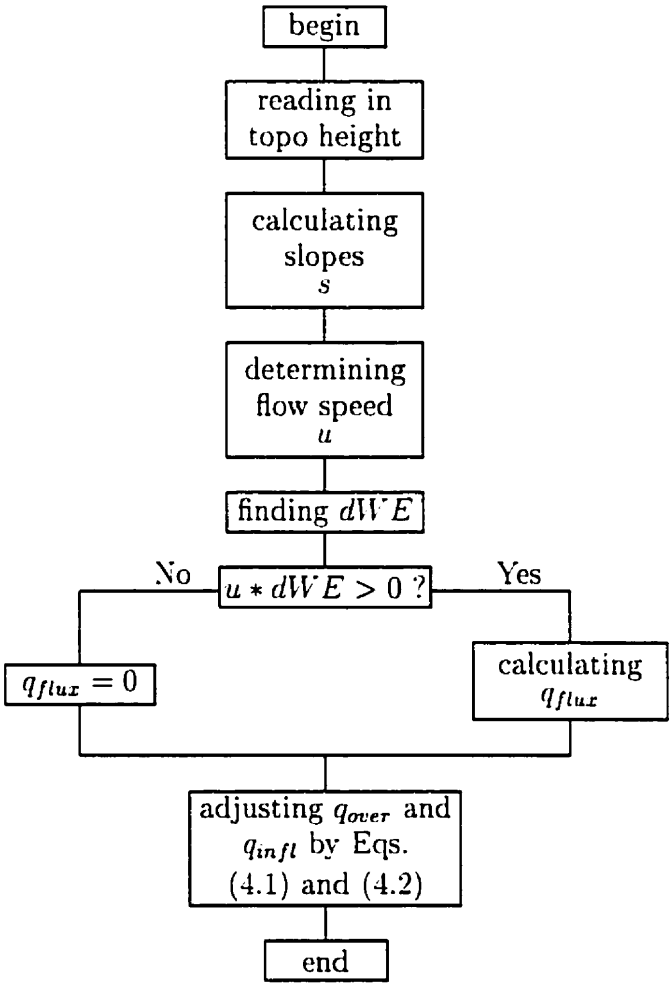

Figure 4.5: Flowing chart showing the functions of the subroutine slp.f.

Chapter 5

Impact of the Modification on Climates

After the modification was coded in the model as described in last chapter, another similar run of the modified CCM3/LSM (the modified model hereafter) was conducted. The configuration of the modified model run was exactly the same as the one in Chapter 3, except the modification on the runoff parameterization proposed in Chapter 4. Another eight-year run (1987-1994) was conducted for the modified model after the spin-up (two and half years). Comparisons will be in a regional scale (in the MRB, the base for the Canadian GEWEX) and global scale.

This chapter includes four sections. First, the impact of the modification on the land surface climate will be discussed from a regional perspective; second, the impact of the modification on the atmospheric climate from a global perspective; third, the potential impact of the modification on the environment; and the last section will be significance check on the modification by T-test and power spectrum analysis on the atmospheric waves, and comprehensive explanations of the complicated impacts the modification brought to the AGCM climates.

The first section will begin with the changes in the surface runoff introduced by the modification. And then changes in ground evaporation, infiltration and soil moisture will be discussed. The Canadian GEWEX research basin, the MRB, was chosen for the discussion in this section from a regional climate perspective. The second section will include the impacts of the modification on surface temperature, temperature in the atmosphere, atmospheric humidity and precipitation. Most of the discussion in this section will be conducted from a global perspective so that we can make proper comparison with previous research results by others to recognize improvements or deficiencies the modification introduced. Detailed point budgets analysis will also be conducted in the Andes Mountains vicinities. The third section will illustrate how the modification impacts the flux of CO_2 in the land surface model from a global perspective. To check the significance of the improvement the modification brought, T-tests on some typical variables and power spectrum analysis on basic atmospheric waves are conducted in the last section.

5.1 Impact on the Land Surface Climate

5.1.1 Surface Runoff

The first modification put into the model is on the surface runoff parameterization. Therefore it is quite natural to first check out the changes in surface runoff introduced by the modification. Figure 5.1 is a comparison plot for total surface runoff simulated by the original (upper panel) and the modified models (lower panel) for the period from January 1987 to January 1995. For all the future horizontal distribution plots in this section, the shaded background is the topographic height resolved by the CCM3 T42 resolution.

The original model gives a maximum of 70 mm near the mountain tops and another

center of 12 mm. It is very difficult to explain physically why the maxima occur at those locations. However, the modified model gives a quite terrain-following pattern of surface runoff, negative bands along the mountain tops and positive bands along the mountain feet at both sides (west and east) of the mountains, especially an over-250mm high at the east side of the mountains. This pattern is what is expected and very easy to understand. Topographic slopes cause outflows from higher topography (mountain tops) and inflows into the lower topography points (mountain feet). The surface runoff is more likely to accumulate at the mountain feet. This pattern will also improve the pattern of the total runoff which will be discussed in Figure 5.4.

5.1.2 Infiltration

Another modification made to the model is the adjustment of infiltration. The infiltration was adjusted with the same algorithm as described in Chapter 4. Figure 5.2 shows a comparison between the original and the modified model simulated infiltration. The modified model gives an overall reduced estimation of the infiltration over the whole domain and a low tongue (featured by the 3000mm contour) at the east side of the mountains. The highs over 13000mm in the original model at the west coastal area were reduced to over-11000mm in the modified model. The 4000mm contour at the east side of the mountains in the original model result was pushed to right over the mountain tops in the modified model result. This pattern is also what is expected and easy to understand. The topographic slopes make it more difficult for the water to stay on the slopes and thus less water infiltrates into the soil on the slopes.

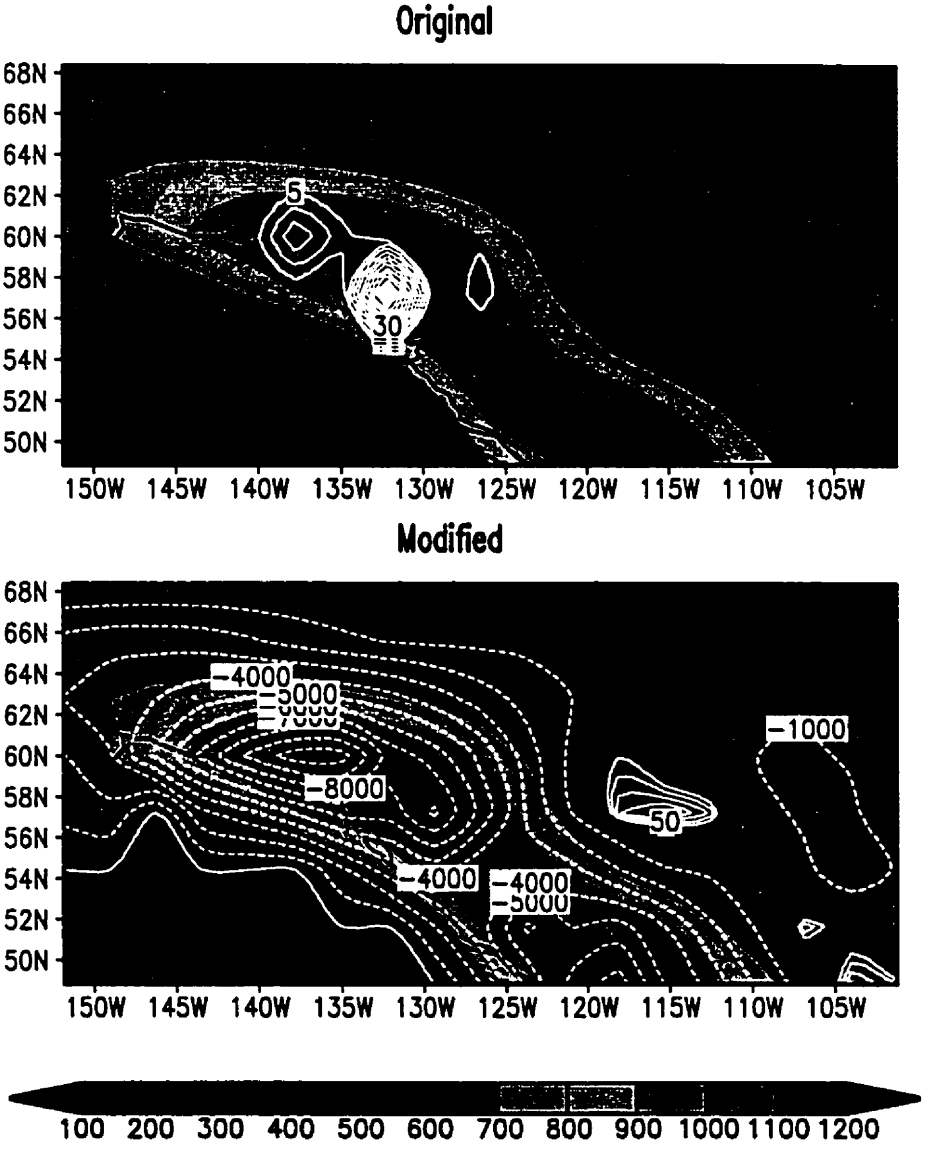

Figure 5.1: Total surface runoff(mm) simulated by the original (upper panel) and the modified models (lower panel) for the period from January 1987 to January 1995. The shaded background is the topographic height resolved by the CCM3 T42 resolution.

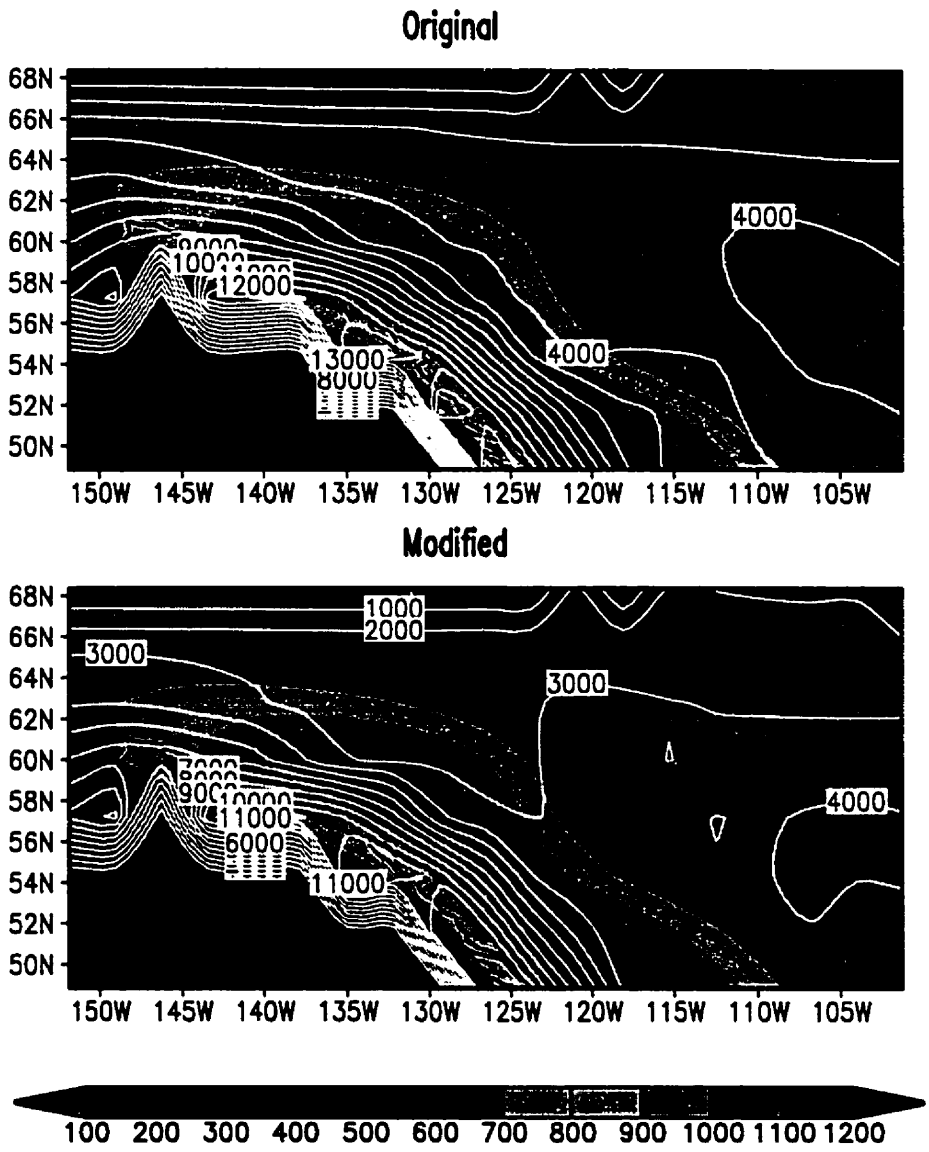

Figure 5.2: Total infiltration(mm) from January 1987 to January 1995, comparison between the simulated fields by the original and the modified models.

5.1.3 Sub-surface Runoff and Total Runoff

As described in Chapter 2, in Bonan's LSM (Bonan 1996b), infiltration was used as the boundary condition to solve the soil hydraulic properties including the sub-surface runoff and soil moisture we are most interested in. In this section, let's first discuss how the changes in the surface runoff and infiltration will affect the sub-surface runoff and then the total runoff.

A comparison of the sub-surface runoff /drainage simulated by the original and modified models is plotted in Figure 5.3. Similar to the infiltration pattern in Figure 5.2, the low band at the east side of the mountains was widened and extends more north-westward than in the original model result, and with a larger magnitude at the low center (400mm) than in the original model result (200mm). Meanwhile, the maxima at the west coast were reduced from 12000mm to 11000mm at similar locations. The northwestward extension of the low band at the east slope of the mountains is mainly due to the low tongue of infiltration there (Figure 5.2) introduced by the modification. Infiltration is used as the boundary conditions in the six-layer soil model to solve the soil hydraulic properties, especially the sub-surface runoff. One can easily find this by comparing the horizontal distribution pattern of the sub-surface runoff and that of the infiltration, which are very similar. More precisely, infiltration was used by the six-layer soil model as the only water supply into the soil column from the interface between the atmosphere and the soil. Therefore, it is quite straight forward that the decrease of infiltration means decrease of water input into the soil model, which results in less sub-surface runoff/drainage; or vise versa.

Total runoff is simply the sum of surface runoff and sub-surface runoff. As plotted in Figure 5.4, the original model gives a low band at the east side of the mountains. And the runoff increases with the topographic height to the mountain tops. This pattern is not quite physically consistent with the topography as discussed in the

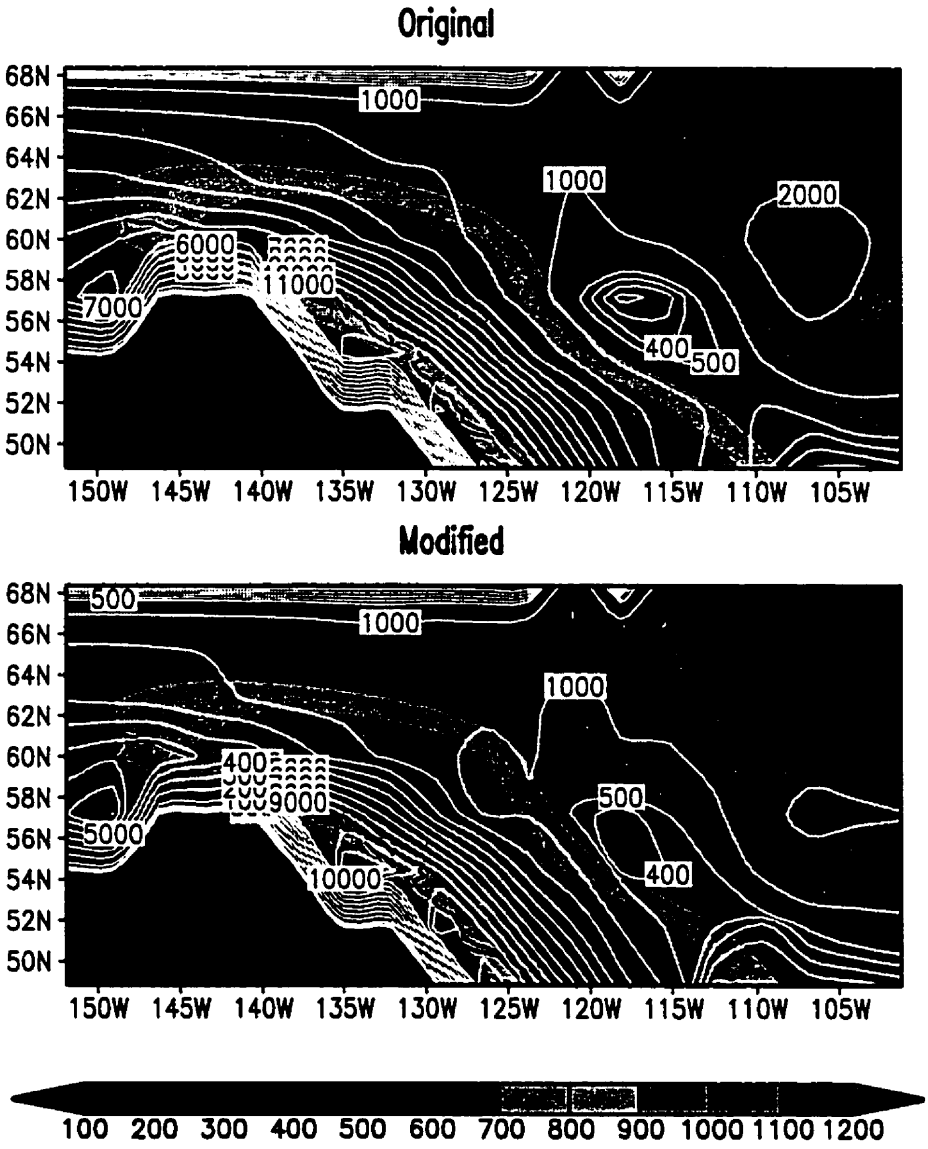

Figure 5.3: Total drainage/ sub-surface runoff (mm) for the period from January 1987 to January 1995, comparison of the simulated fields by the original and the modified models.

verification results in Chapter 3.

The modified model generated a quite different pattern for the total runoff compared with that from the original model. High bands at the mountain feet at both west and east sides and a low band along the mountain tops. The low band at the east side of the mountains in the original model becomes a wide high band in the modified model. The maxima of over 12000mm at the west coast from the original model were reduced to about 10000mm. These decreases are due to the decrease in the subsurface runoff. The low band along the mountain tops is mainly due to the negative band in surface runoff at the same locations caused by the topography-introduced lateral outflows at the surface. This pattern is what is expected.

Comparing the horizontal distribution pattern of total runoff given by the modified model with the diagnosed (Figure 3.8) and the observed (Figure 3.9) patterns, one should be convinced that the modified model can generate a horizontal distribution pattern of total runoff, which is much closer to the diagnosed and the observed, and which is much more consistent with topography and thus very easy to explain physically.

5.1.4 Evaporation

The above analysis on runoff has concluded that the modification improved the runoff simulation in the model. The changes in runoff and infiltration must have an impact on ground evaporation, another important variable in both climatology and hydrology.

Ground evaporation is very season sensitive. For more season-sensitive variables, analysis will be conducted in two representative seasons, summer and winter, which will be represented by August and January, respectively in this study. A general discussion on sensitivity of the modification to time scales will be given in section 5.2.3.

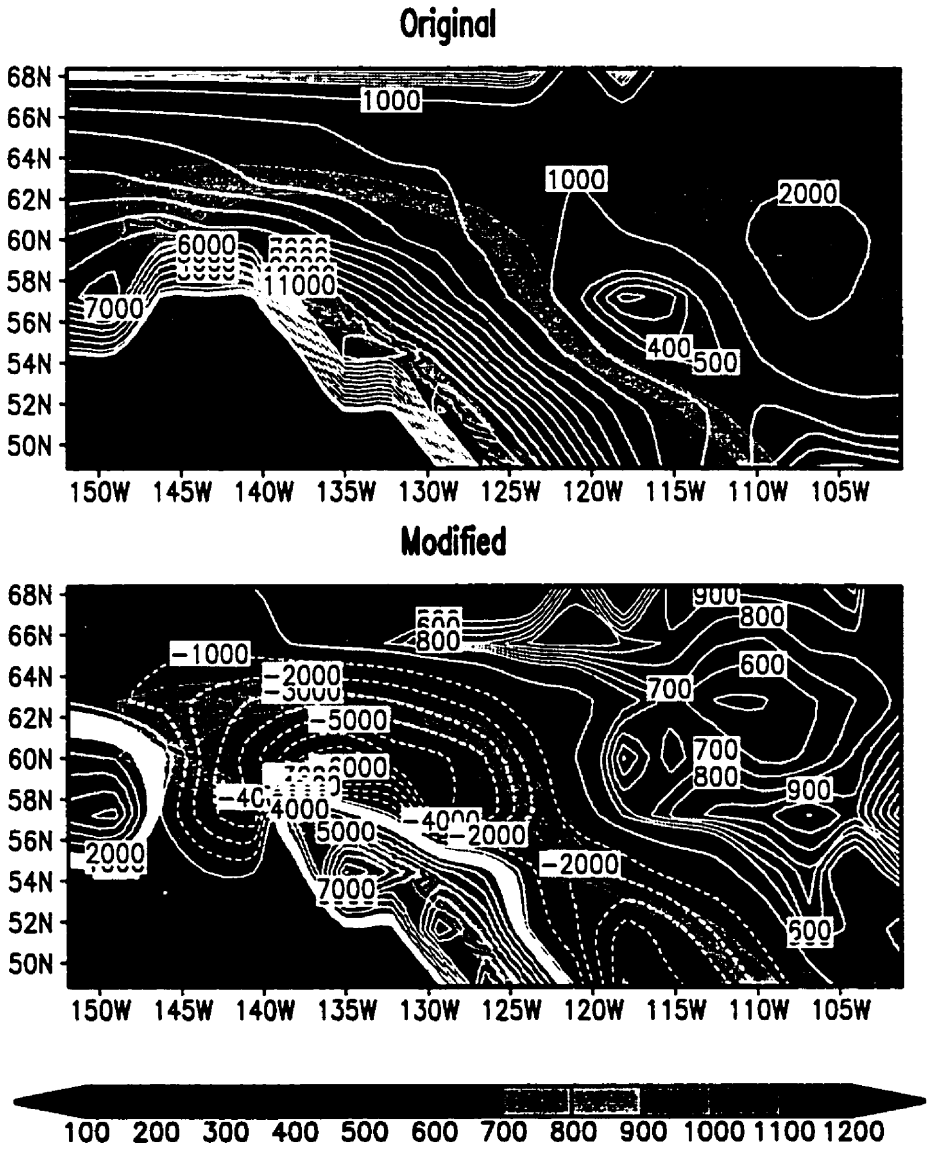

Figure 5.4: Total runoff (mm) for the period from January 1987 to January 1995, comparison of the simulated results by the original and modified models.

Plotted in Figure 5.5 is the ground evaporation in the summer of 1994. Little difference can be found at the west coast between the results simulated by the original and the modified models. However, at the lee side of the mountains, the high band extends more to the northwest with a higher center (over 100 W/m^2) compared with the original model result (over 80 W/m^2). The ground evaporation along the mountain tops is substantially reduced by over $20Wm^{-2}$ in the modified model result. This is mainly due to the drier soil at the mountain tops and slopes (Figure 5.7) in the modified model. While in winter (Figure 5.6), ground evaporation slightly increased along the mountain tops possibly due to the warmer temperature in corresponding area in the modified model than in the original model (Figure 5.12) when the soil wetness was not changed much (Figure 5.8). The most significant increase in winter was found at the east side of the mountains with a maximum of over $60Wm^{-2}$ in the modified model result, whereas it is $55Wm^{-2}$ in the original model result. There are two reasons for this increase: more water accumulation at the mountain foot increased the soil moisture; the warmer temperature in the corresponding area in the modified model than in the original model is favorable for evaporation (Figure 5.12). Meanwhile, the evaporation at the west coast is also slightly increased by the modified model due to more water accumulated at the mountain foot.

5.1.5 Soil Moisture

Changes in infiltration will definitely affect the soil moisture. The first variable we will check is the evaporation soil wetness, which is a very good indicator for the first soil layer wetness (Bonan 1996b). Plotted in Figure 5.7 and 5.8 are the evaporation soil wetness for the summer and winter seasons, respectively.

In summer (Figure 5.7), the first soil layer is much drier over the areas, where the infiltration is substantially reduced in the modified model (Figure 5.2) than in

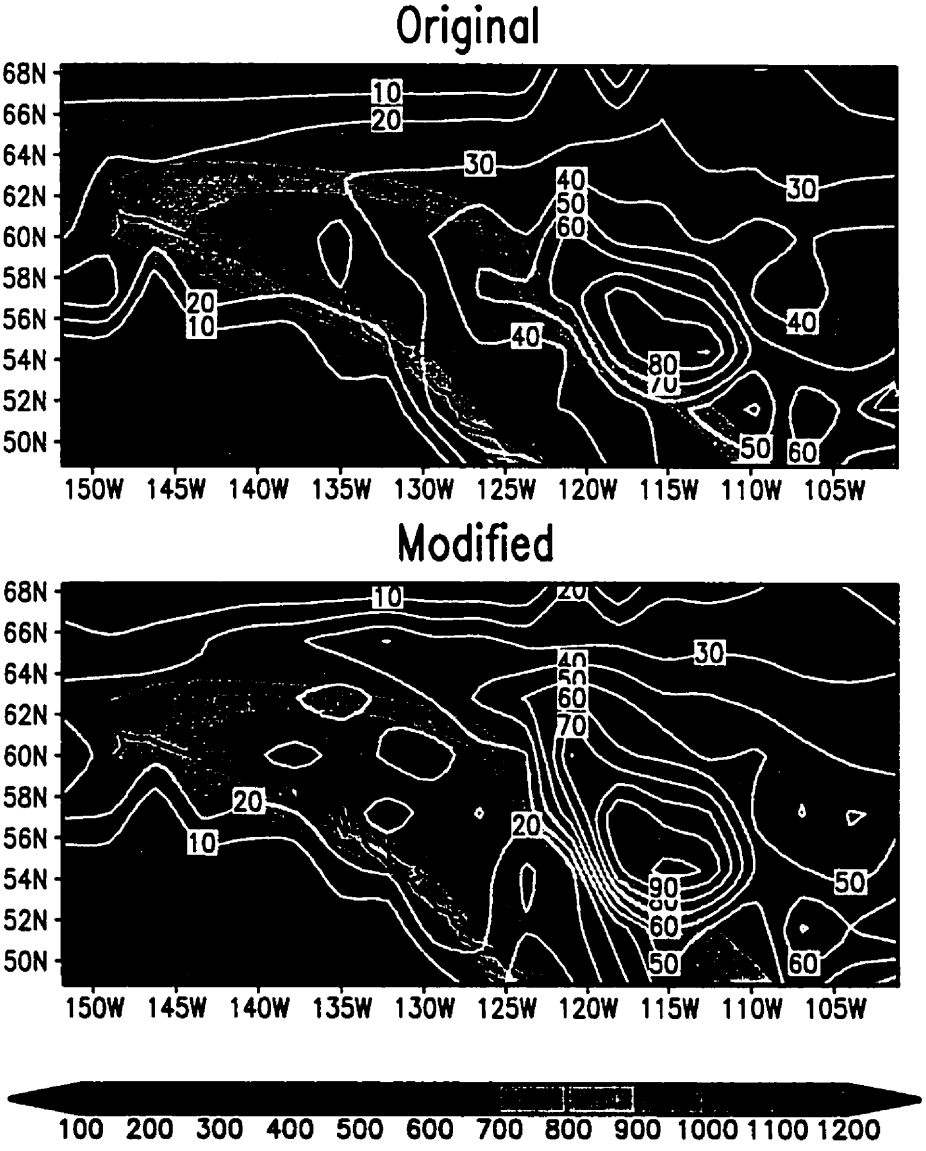

Figure 5.5: Ground evaporation(Wm^{-2}) in August 1994, comparison between the simulated fields by the original and the modified models.

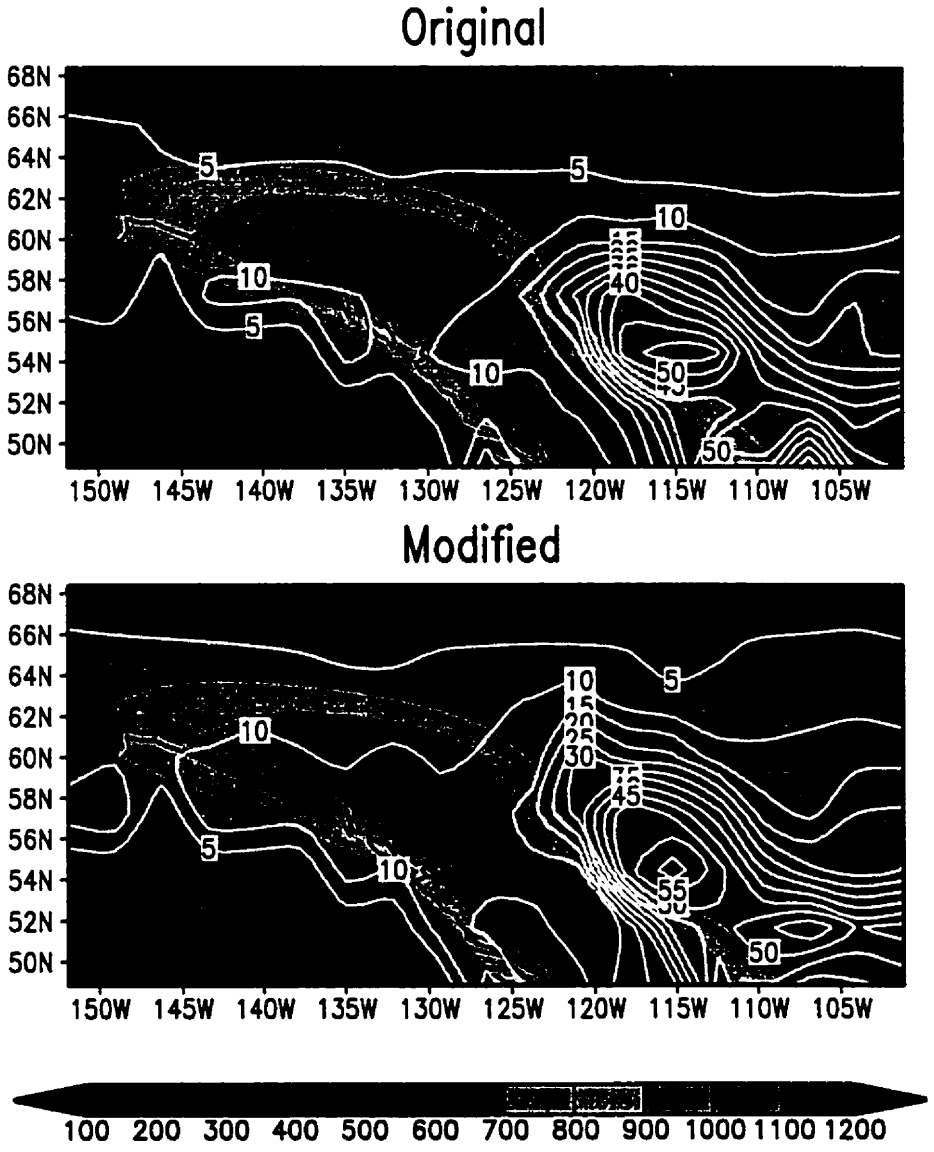

Figure 5.6: Ground evaporation(Wm^{-2}) in January 1995, comparison between the simulated fields by the original and the modified models.

the original model. The modified model gives a very obvious dry band along the mountain tops and the on the slopes, and wet bands along the mountain feet at each side of the mountains. However, nearly no difference can be found in the horizontal distribution of the soil wetness in winter (Figure 5.8), except that the wet center at the east side of the mountains has a 0.1 higher value and, slightly wetter soil is found at the south-east corner of the domain. The most possible reason for the slight changes in winter is that the soil is frozen in this area during winter.

Another variable previous researchers usually checked is the root soil water, which is an integral of the total water content in a soil column. However, Figures 5.9 and 5.10 show very slight difference (featured by the 0.3 contour) between the modified model result and the original model result. This means that the modification does significantly affect the soil wetness at shallow soil layers (Figure 5.7), but does not affect the total water content in the soil column as a whole. This seems a puzzle. But it is very easy to understand when one compares the infiltration and drainage/subsurface runoff (Figures 5.2 and 5.3). The increased infiltration into the soil at the top of the soil column generated more drainage out of the soil at the bottom of the soil column, which keeps the total water content in the soil column nearly unchanged. This is determined by the mechanism of the soil model.

All the above conclusions will be further confirmed by the point budgets analysis presented in subsection 5.2.2.

The above analysis on horizontal distribution has concluded that the modification in the runoff parameterization can generate a runoff horizontal distribution pattern, which is much closer to both of the observed and the diagnosed patterns than the original model did. Along the higher topography (especially on slopes), infiltration was reduced, and thus the soil moisture in the top soil layer was reduced too. But the integral water content in the whole soil column was not changed because the

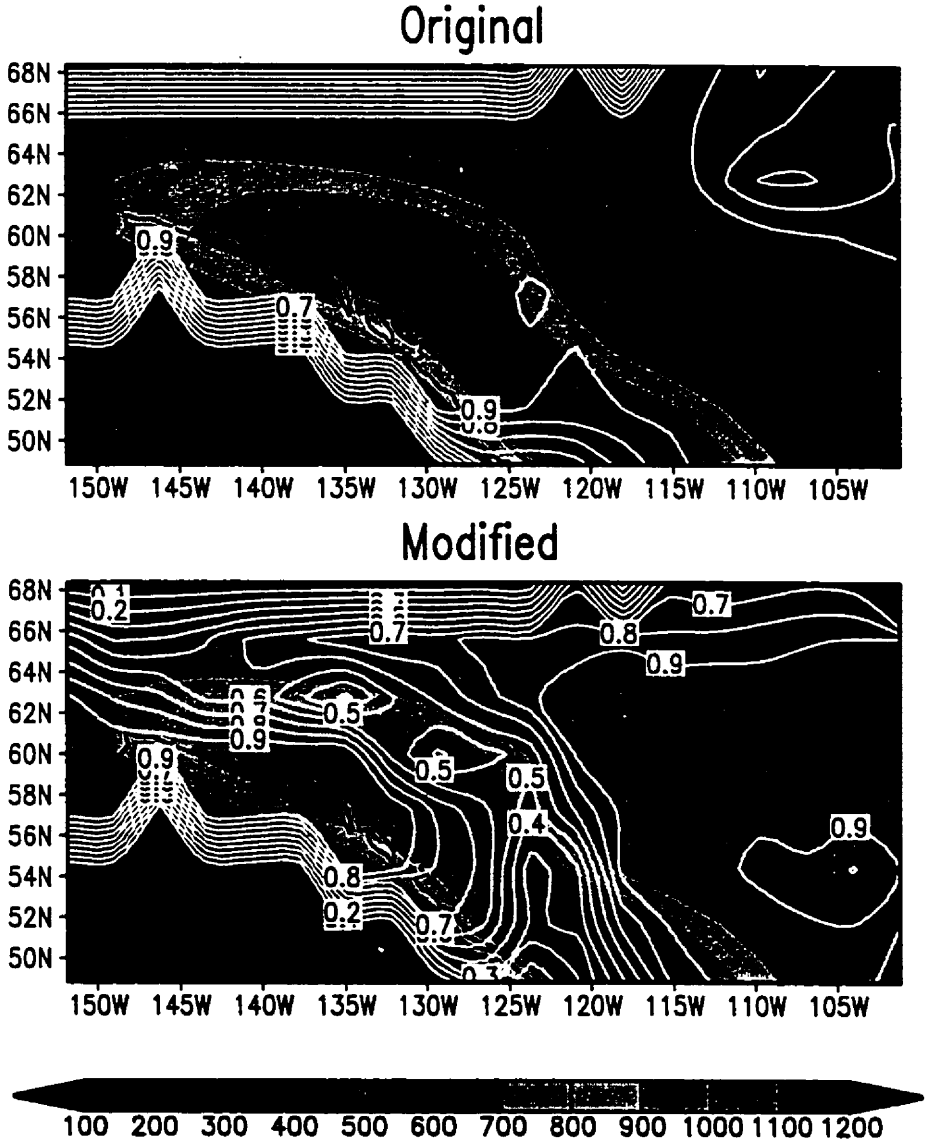

Figure 5.7: Evaporation soil wetness (fraction) in August 1994, comparison between the simulated fields by the original and the modified models.

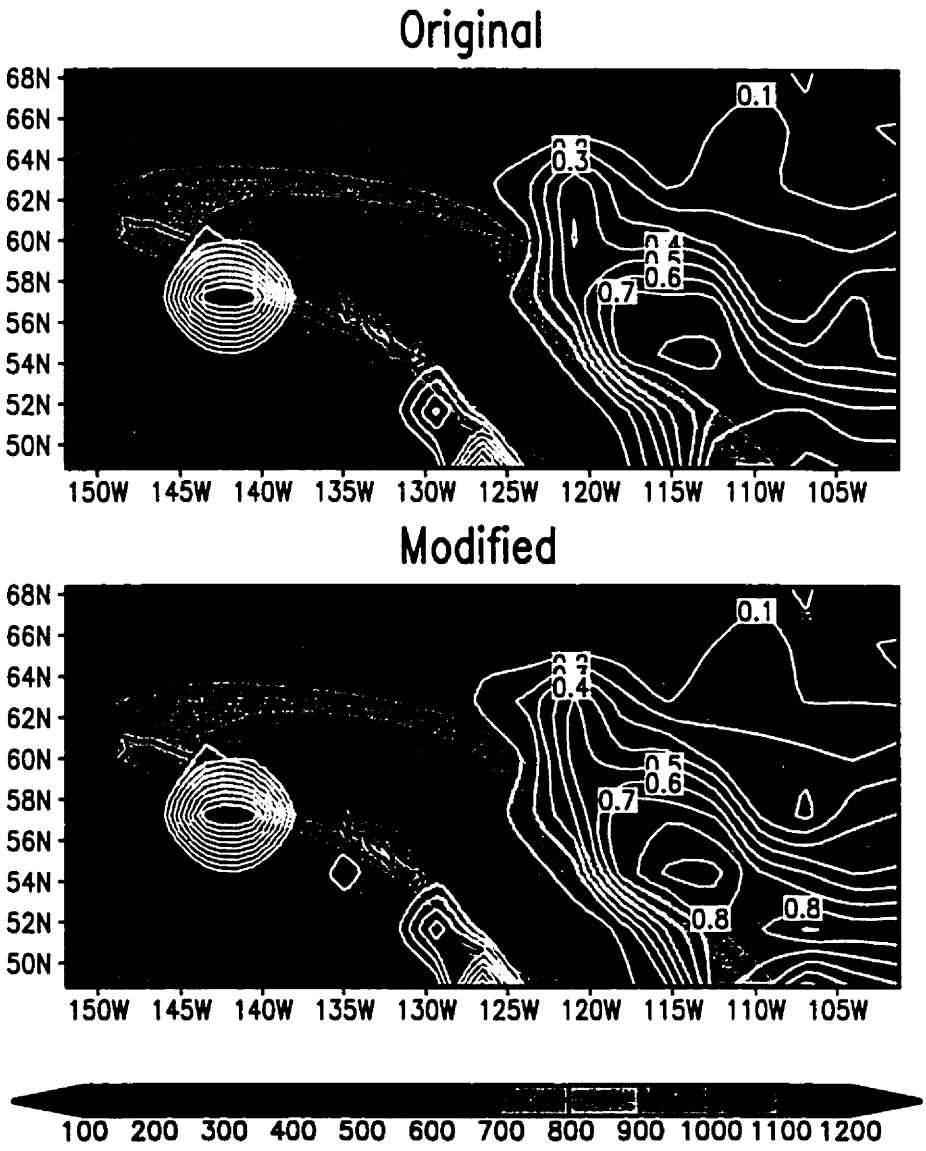

Figure 5.8: Evaporation soil wetness (fraction) in January 1995, comparison between the simulated fields by the original and the modified models.

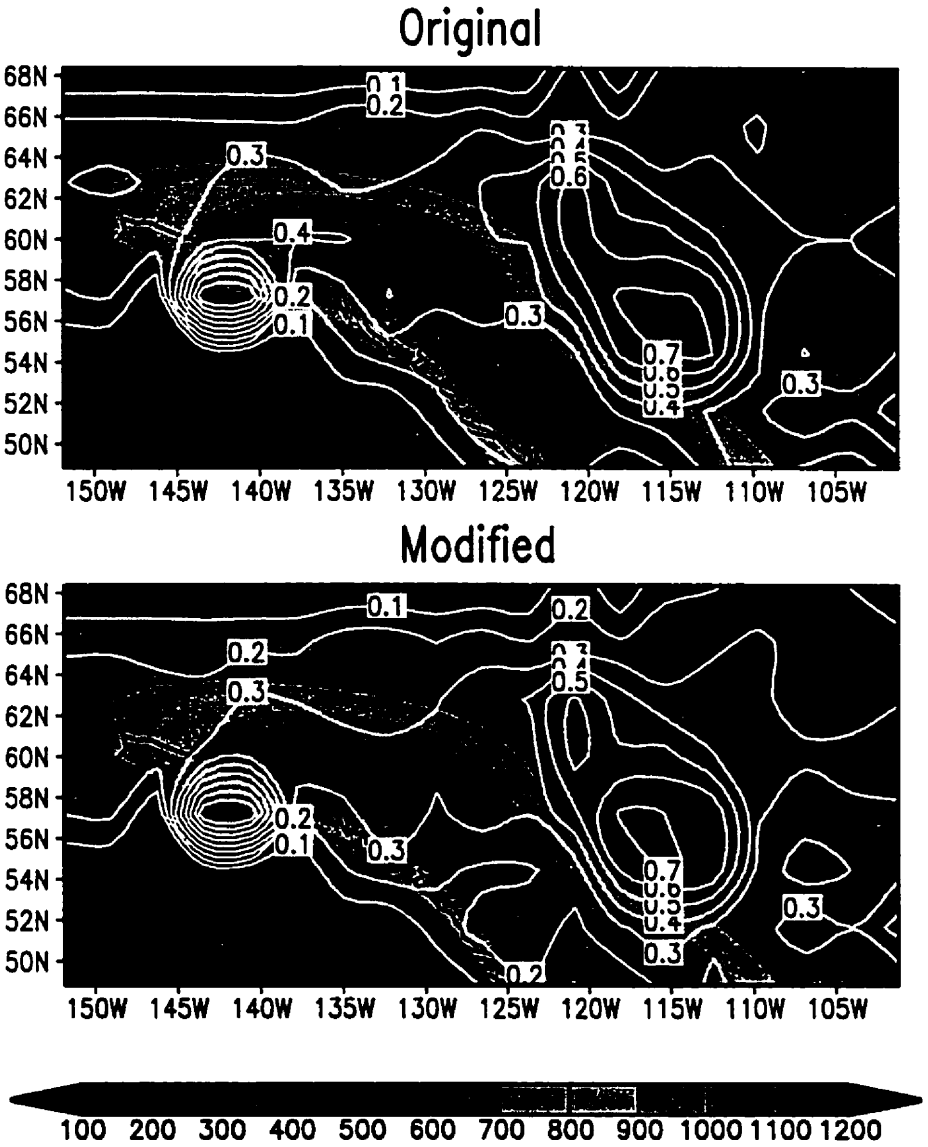

Figure 5.9: Root soil water(fraction) in August 1994, comparison between the simulated fields by the original and the modified models.

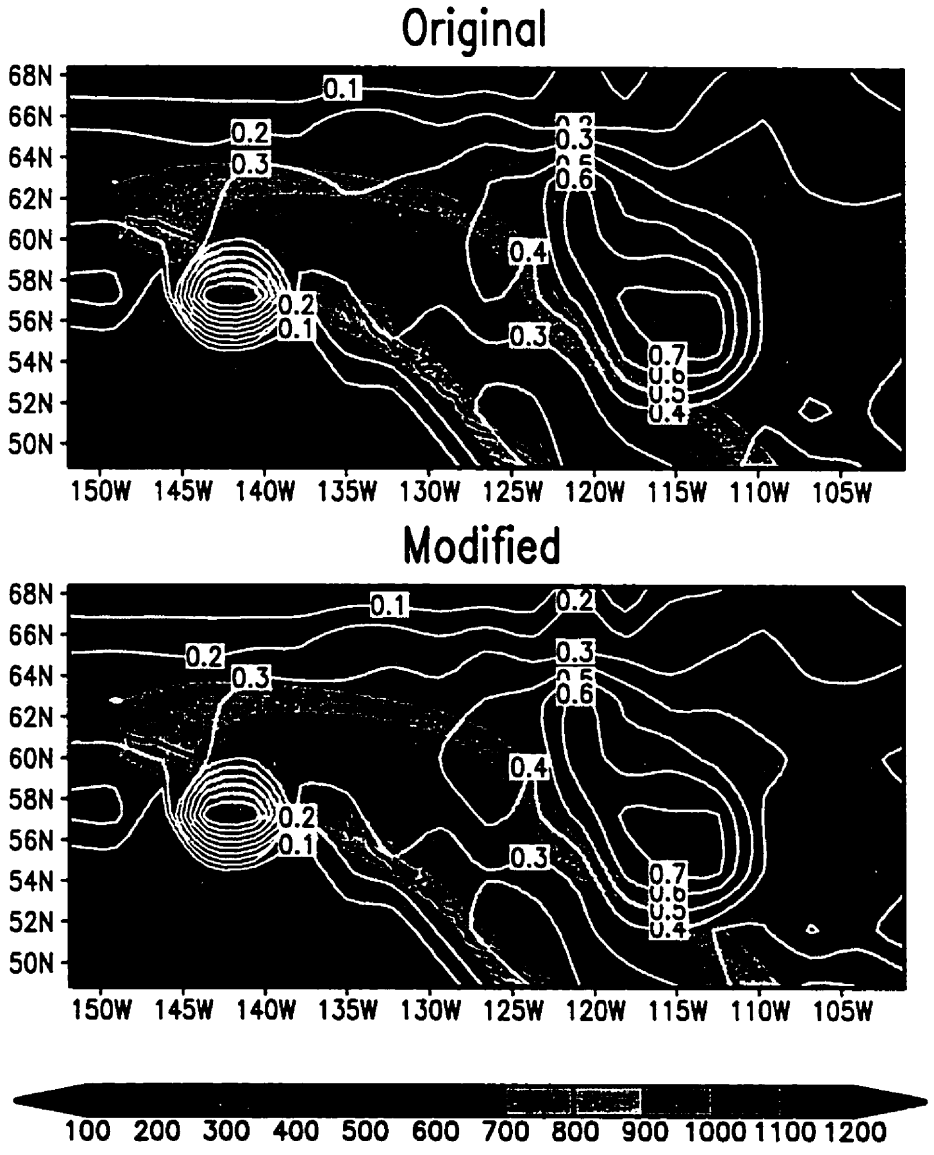

Figure 5.10: Root soil water(fraction) in January 1995, comparison between the simulated fields by the original and the modified models.

increase (decrease) of the drainage out of the soil at the bottom of the soil column balanced the increase (decrease) of the infiltration into the soil at the top of the soil column. Corresponding changes were found in ground evaporation, i.e., in areas where infiltration reduced, evaporation reduced; in areas where infiltration increased, evaporation increased too.

Now it is time to ask how these changes affect the atmosphere. In next section, changes in the atmospheric climate caused by the modification will be discussed. Some of the conclusions will explain the conclusions in this section. For example, the ground evaporation also depends on the ground temperature except the soil moisture; i.e. keeping the soil moisture as a constant, the warmer the ground, the higher the ground evaporation; or vise versa. Readers will find that the conclusions from this section and those from the next section are consistent with each other.

5.2 Impact on the Atmospheric Climate

5.2.1 Surface Temperature

As in other studies (Bonan 1996a, and many others), we begin the comparison with the surface temperature. In summer (Figure 5.11), the modified model significantly warmed up the mountain tops and even the lee side of the mountains. This can be found by comparing the 278K and 284K contours between the original and the modified model results. As a result, at the east side of the mountains the warm ridge was strengthened. In winter (Figure 5.12), significant warm-up can also be found along the mountain tops and the north part of the domain. The warm-up along the mountain tops is featured by the 261K and 264K contours.

One of the directly related variables to the surface temperature is the latent heat flux from the ground. In Figures 5.13 and 5.14 are the latent heat flux comparisons

between the original and the modified models at the same times. It is quite obvious in summer (Figure 5.13) that the modified model substantially reduced the latent heat flux along the mountain tops where the surface temperature was warmed up by the modified model.

These conclusions are consistent with Bonan's general conclusions in Bonan (1996a), i.e., "infiltration reduced, resulting in drier soil and less latent heat flux and thus warmer ground surface." While in his Table 6, conflict data were presented for the Mackenzie River basin: for the four seasons, the surface temperature in winter, and fall decreased, unchanged in summer and slightly increased in spring, and the annual average decreased. As an explanation for this conflict, he just mentioned that, in basins where soil was very wet (Mackenzie, Yukon Kolyma), infiltration decreased and the soil dried. Latent heat flux decreased during the summer, but the soils were wet enough that surface air temperatures did not significantly increase (Bonan 1996a). Higher consistency of our data with Bonan's general conclusion implies that the modification made in this study did improve the LSM's performance. This will be more clearly confirmed by the point budget analysis in the next subsection.

However, in winter (Figure 5.14), nearly no changes were found in the latent heat flux between the modified and the original model results, but the surface temperature was still warmed up by the modified model along the mountain tops. This reminds one that surface soil wetness and latent heat flux are not the only two factors affecting the surface temperature. Of course, the upper atmospheric structure and general atmospheric circulations also play an important role on the surface fields. One will find out in section 5.4 that this winter warm-up is very possibly related to the changes in the general atmospheric waves caused by the modification.

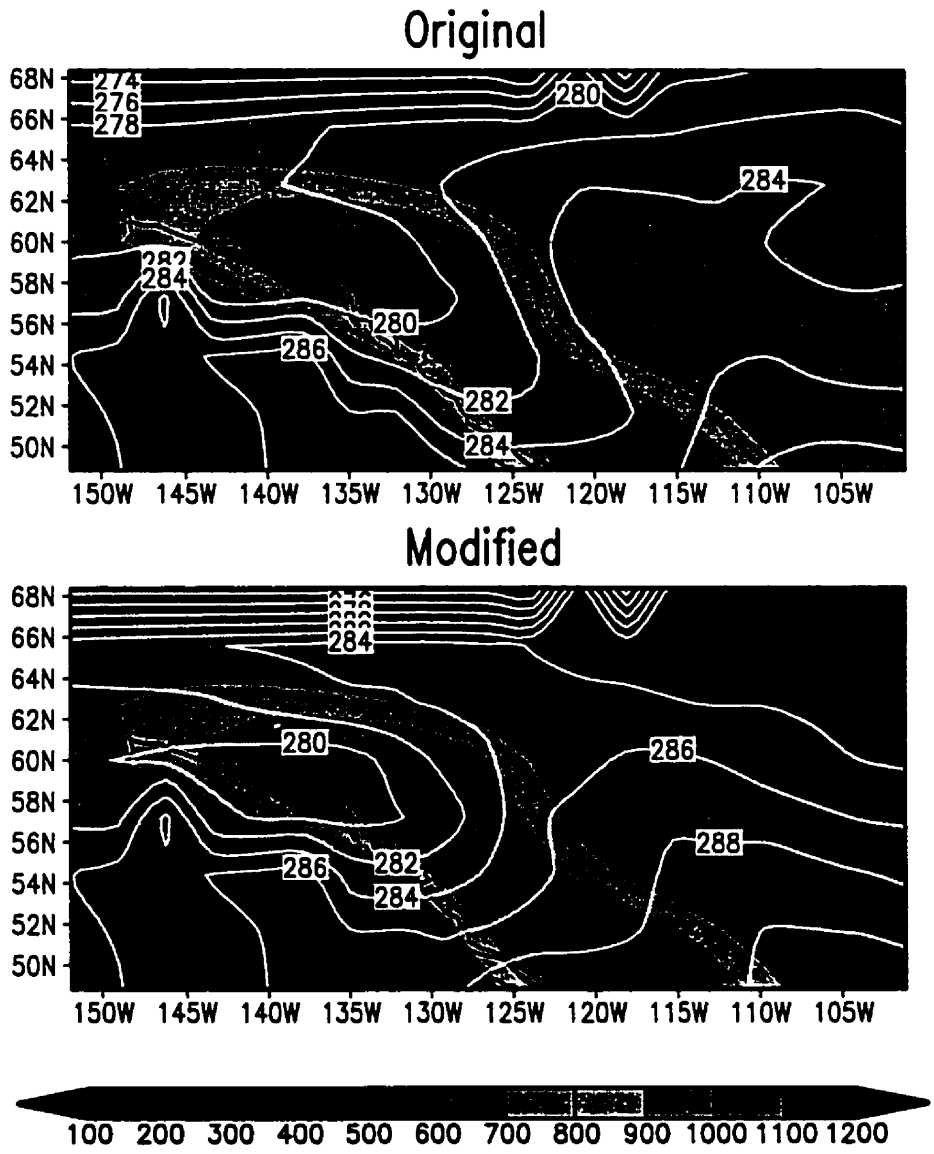

Figure 5.11: Surface temperature(K) in August 1994, comparison between the simulated fields by the original and the modified models.

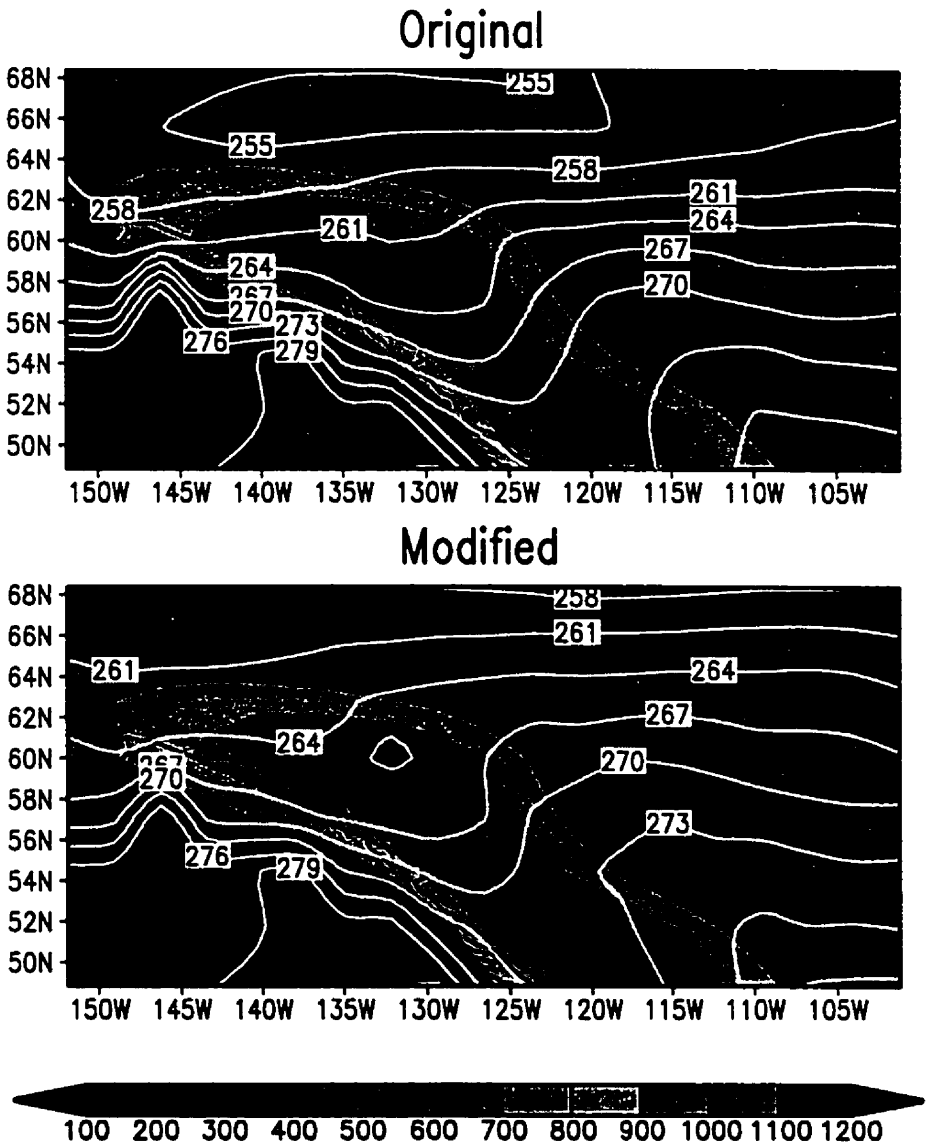

Figure 5.12: Surface temperature(K) in January 1995, comparison between the simulated fields by the original and the modified models.

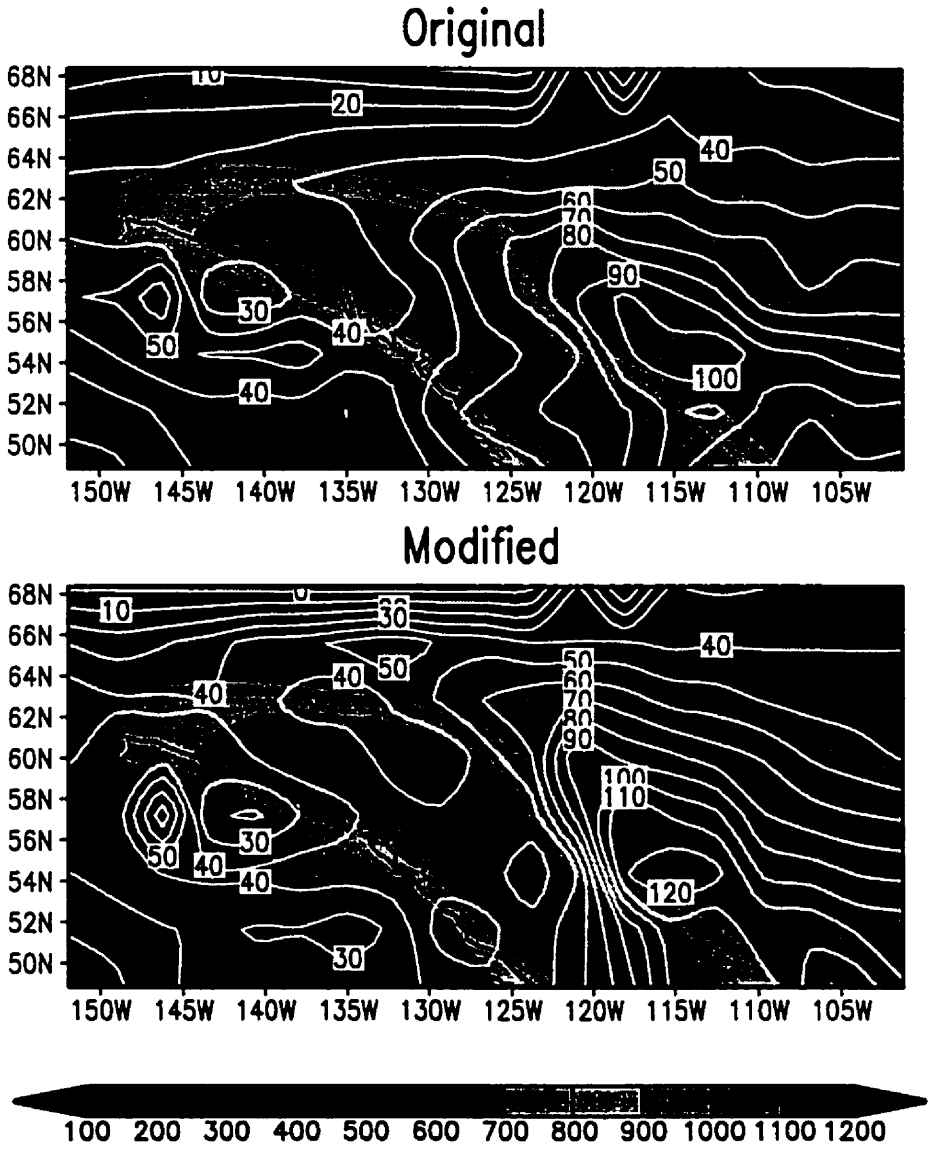

Figure 5.13: Surface latent heat flux (Wm^{-2}) in August 1994, comparison between the simulated fields by the original and the modified models.

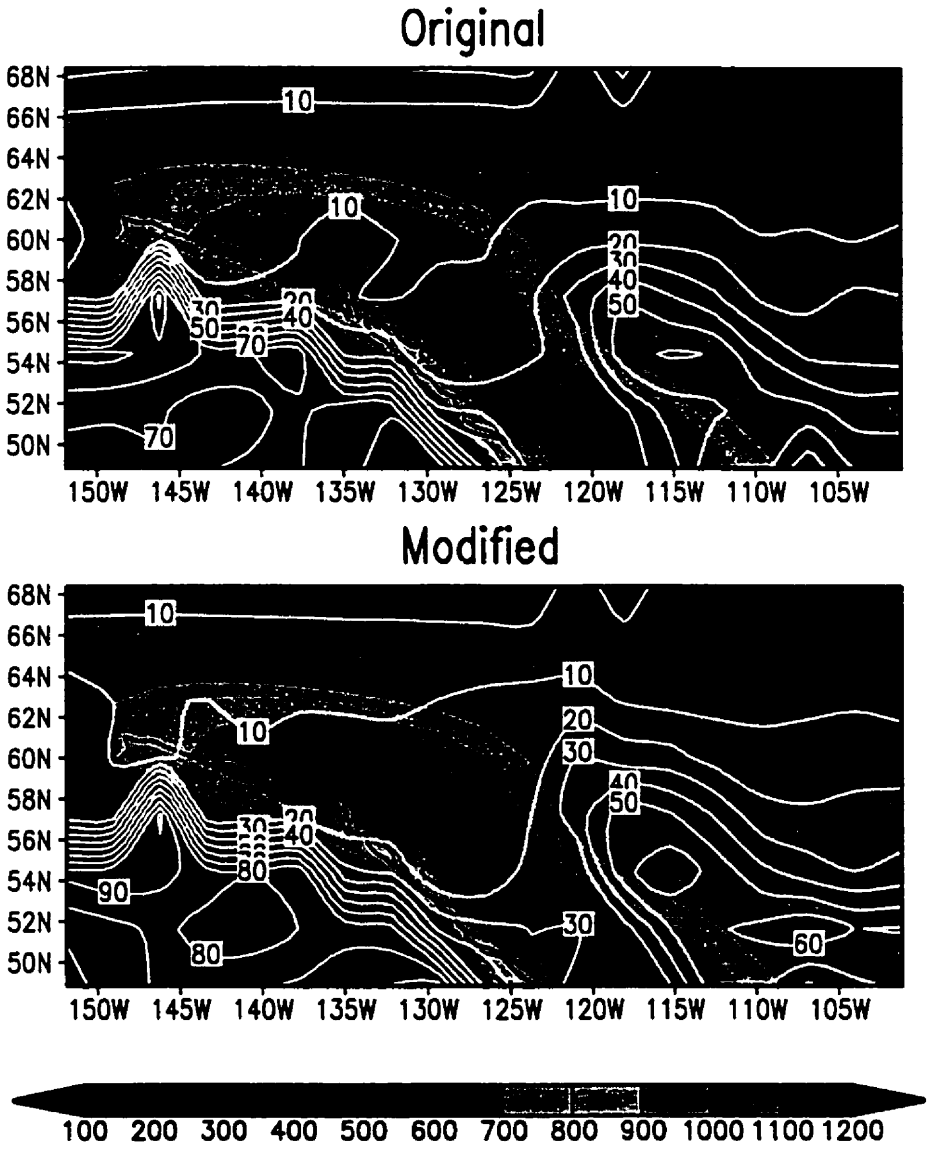

Figure 5.14: Surface latent heat flux (Wm^{-2}) in January 1995, comparison between the simulated fields by the original and the modified models.

Table 5.1: Locations and topographic features of the three points chosen for point budgets analysis.

Points	Location	Latitude	Longitude	Topographic Height (m)
A	at mountain top	20.93S	67.5W	3075.69
B	on lee slope	20.93S	64.7W	2301.85
C	at mountain foot	20.93S	59.1W	32.57

5.2.2 Point Budgets Analysis

To further clarify the conclusions obtained from the horizontal distribution analysis in last subsection, surface energy and moisture budgets analysis will be conducted for single points. Three points in the Andes Mountains vicinities in South America are chosen for the point budgets analysis for the next three reasons. Firstly, significance test shows that changes brought by the modification in this region are much more significant than in the MRB region (Figure 5.43); secondly, the Andes Mountains have a much simpler geographic features, with a narrow east-west extension and an almost south-north line, which is most suitable to explain the physical mechanism of the modification; and finally, analysis of more regions can be supplementary proof of improvements the modification brought.

The three points were chosen along the latitude where the highest topography of Andes occurs, and where the changes by the modification are significant. Their locations and topographic features are listed in Table 5.1. Point A is at the Andes Mountain top with the highest topographic height of 3075.69m; Point C is at the mountain foot with the lowest topographic height of 32.57m; and point B is at the middle of the lee slope with a topographic height of 2301.85m.

The mean values for the four three-month seasons and for the year are calculated

for the important budget terms responsible for changes in surface energy and moisture. They are listed in Tables 5.2, 5.3 and 5.4 for points A, B, and C, respectively. The first 6 columns are for surface moisture budget analysis; and the last three columns are for surface energy budget (or temperature) analysis. Note, not all the budget terms are configured to be output in the model runs. Terms listed in these tables are based on available model outputs.

At point A (Table 5.2), because of the lateral water outflow caused by its higher topography than its neighbouring grid cells, infiltration and total runoff are significantly reduced by the modification for all seasons and the annual average. The most reduction in infiltration occurred in the Southern Hemisphere Summer (DJF) by about 5 mm/day. In the soil water budget equation in Bonan's LSM (Bonan 1996b), infiltration is a dominant term for water supplies to the soil; therefore, the significant reduction of infiltration caused significant reduction in root zone soil water (RSW column). More significant reduction was found in the first soil layer wetness (SW1 column). The dried soil by the modified model resulted in less ground evaporation (EVA column). The reduction of precipitation is definitely related to the reduced ground evaporation, but it is also related to other complicated upper atmospheric processes.

Surface latent and sensible heat fluxes are the most important terms in the surface temperature calculation by the surface energy budget equation in Bonan's LSM (Bonan 1996b). Bonan (1996a, 1998) gave the reduced latent heat flux as the only reason for the warmer surface temperature. Besides the consistency with Bonan's previous result on "reduced infiltration causes drier soil and less latent heat flux and thus warms up the surface", here we added another reason for the warmer surface temperature: the increased sensible heat flux (SHX column). These resulted in about a 1 - 2K warmer surface temperature at point A.

Table 5.2: Point A at the mountain top: mean infiltration (INF, mm/day), total runoff (RUN, mm/day), ground evaporation (EVA, mm/day), total precipitation (PRE, mm/day), root zone soil water (RSW, fraction), the first soil layer wetness (SW1, fraction), latent heat flux (LHX, mm/day), sensible heat flux (SHX, mm/day), and the surface temperature (TSA, K) for the four three-month seasons. Top numbers are for the original model; bottom numbers are for the modified model.

	INF	RUN	EVA	PRE	RSW	SW1	LHX	SHX	TSA
DJF	8.16	0.45	2.19	9.02	0.28	0.82	4.09	1.87	286.87
	2.74	-6.65	1.13	5.72	0.15	0.44	2.75	2.93	288.16
MAM	6.42	3.82	2.60	6.95	0.35	0.99	3.51	1.04	285.04
	3.23	-6.61	1.81	7.19	0.26	0.74	2.74	1.50	285.62
JJA	1.21	2.71	1.23	1.23	0.23	0.54	1.37	0.67	279.77
	0.08	-6.54	0.23	0.53	0.19	0.10	0.41	1.20	281.33
SON	1.03	0.88	0.95	1.11	0.20	0.26	1.34	2.35	283.79
	0.17	-6.64	0.15	0.59	0.17	0.04	0.57	2.86	285.60
Annual	4.21	1.96	1.74	4.58	0.26	0.65	2.58	1.48	283.87
	1.56	-6.61	0.83	3.51	0.19	0.33	1.62	2.12	285.18

On the contrary, at point C (Table 5.4) at the mountain foot, because of the lateral water inflow caused by its lower topography than its neighbouring grid cells, infiltration and total runoff are significantly increased by the modification for all seasons and the annual average. The most increases in infiltration and runoff occurred in the Southern Hemisphere Winter (JJA) by about 1.1 mm/day, probably due to the increased precipitation in this season. Except this season, precipitation in other seasons and the annual average are slightly reduced (by 0.1 mm/day for the annual mean). Changes in the root zone soil water are minor at this point probably due to

the fact that soil at this low topography has higher water content (or higher water table) at most of the time. Somehow, this can be verified by the smaller magnitude of changes in the infiltration and runoff than at point A. Again more significant increases can be found in the first soil layer wetness (SW1). Increased soil wetness caused increases in ground evaporation.

As a result of the increased ground evaporation, latent heat flux increased, and together with the slightly reduced sensible heat flux (SHX), cools down the surface temperature at this mountain foot point, by 1 - 2K for most seasons and 1.1K for the year.

Terms listed in Table 5.3 for point B generally have the same features as those for point A but with smaller magnitudes of changes. This is determined by its geographic location, between points A and C, but closer to A. Point B receives inflows from upstream grid cells (including A) and generates outflows to the downstream points (including C). The results in Table 5.3 shows that in most seasons and the annual average point B gives net lateral water outflows as point A. Therefore, all conclusions for point A are also applicable to point B.

In summary, the point budgets analysis conducted in this section more clearly confirmed the conclusions we got from the horizontal distribution analysis at another geographic location. And our conclusions are consistent with previous works (Bonan 1996a; 1998) but with a more detailed explanation.

5.2.3 Sensitivity to Time Scales

So far, the analysis on the surface temperature is mainly based on the monthly means output from the models. Now, before any further discussions on the impact of other climate variables, it is useful to check out at which time scale(monthly, seasonal or annual) the model is most sensitive to the modification.

Table 5.3: As in Table 5.2, but for Point B on the mountain slope.

	INF	RUN	EVA	PRE	RSW	SW1	LHX	SHX	TSA
DJF	14.82	7.01	2.25	15.80	0.34	1.00	4.00	1.02	289.04
	10.12	-5.25	2.41	15.66	0.31	0.96	4.37	1.25	289.82
MAM	9.32	9.35	2.12	9.88	0.28	0.96	3.06	0.88	287.83
	6.44	2.24	1.95	10.62	0.29	0.92	2.90	0.98	287.93
JJA	1.43	2.42	1.29	1.50	0.22	0.65	1.50	0.63	283.53
	0.16	-3.96	0.26	0.74	0.20	0.13	0.49	1.20	284.67
SON	2.97	0.79	2.07	3.16	0.20	0.64	2.59	1.28	286.70
	1.39	-5.09	0.99	2.89	0.18	0.29	1.59	1.99	288.76
Annual	7.14	4.89	1.93	7.58	0.26	0.81	2.78	0.95	286.78
	4.52	-3.02	1.40	7.47	0.25	0.57	2.33	1.35	287.80

Table 5.4: As in Table 5.2, but for Point C at the mountain foot.

	INF	RUN	EVA	PRE	RSW	SW1	LHX	SHX	TSA
DJF	5.06	0.23	3.80	5.23	0.31	0.69	3.80	1.92	301.79
	5.57	1.04	4.16	4.90	0.32	0.75	4.34	1.66	301.69
MAM	3.07	0.41	2.73	3.27	0.31	0.62	3.10	1.75	301.30
	3.85	1.22	3.25	3.22	0.32	0.75	3.62	1.26	299.77
JJA	0.56	0.49	0.63	0.61	0.28	0.30	0.91	1.65	293.54
	1.66	1.35	1.48	0.88	0.29	0.59	1.78	1.00	290.81
SON	2.58	0.31	1.94	2.75	0.29	0.52	2.26	2.01	295.72
	2.45	1.27	2.35	1.75	0.28	0.56	2.65	1.76	295.46
Annual	2.81	0.36	2.28	2.96	0.30	0.54	2.56	1.83	298.08
	3.39	1.22	2.81	2.69	0.31	0.66	3.10	1.42	296.93

We still take the surface temperature as an example and compare the seasonal means (Figure 5.15) and the annual means (Figure 5.16) with the monthly means (Figures 5.11 and 5.12) given in the last section.

Compared with the monthly means shown in Figure 5.11, the seasonal means, taking summer for an example, give the same pattern with weaker warm-up. But significant difference can still be found between the original and the modified model results at seasonal time scale. The least difference was found in the annual averaged surface temperature (Figure 5.16), in which one can find nearly no difference between the original and modified model results, except the 260K and the 262K contours at the north-east corner of the domain.

Therefore, from a regional scale perspective, the model is most sensitive to the modification at the monthly time scale, less sensitive at seasonal scale and least sensitive at the annual time scale.

Comparisons between the two models' results for consecutive years' annual averages (not shown) show that the impact of the modification is getting weaker when time scale increases. However, the impact still visibly exists. This implies that, from a regional scale perspective, the modification does changed the model climate at even seasonal and annual time scales. The changes at monthly time scale are not noises.

From the T-test results in section 5.4, one can easily find that, in a global view, even the annual averaged surface temperature (for 8 years) is significantly changed by the modification in many regions, especially in vicinities of high topography.

5.2.4 Atmospheric Temperature

In last section, from a regional scale perspective, the model result analysis has convinced that the modification in the runoff parameterization does have important impact on the surface climate. Now, from a global perspective, let's see what happened

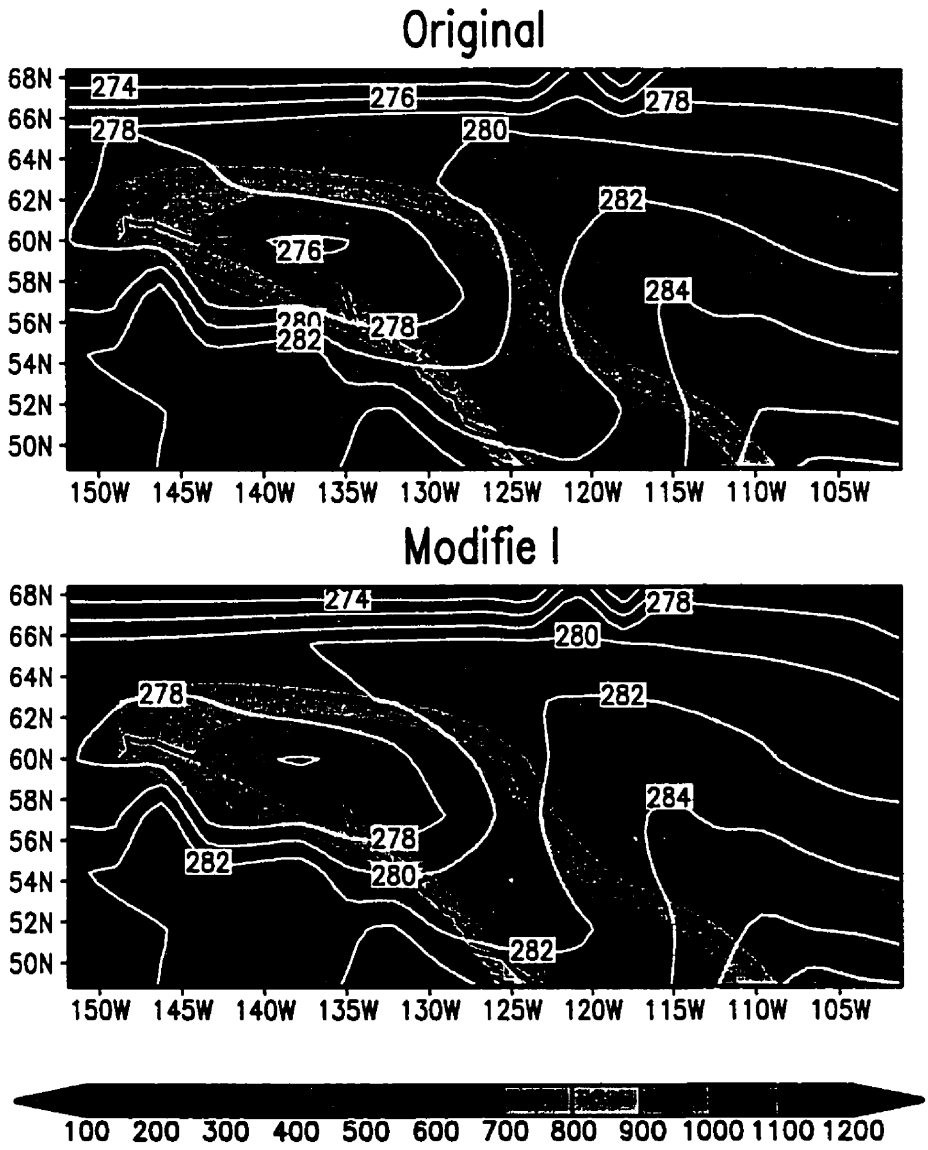

Figure 5.15: Seasonal surface temperature (K) for summer (June, July and August. JJA hereafter), comparison between the simulated fields by the original and the modified models.

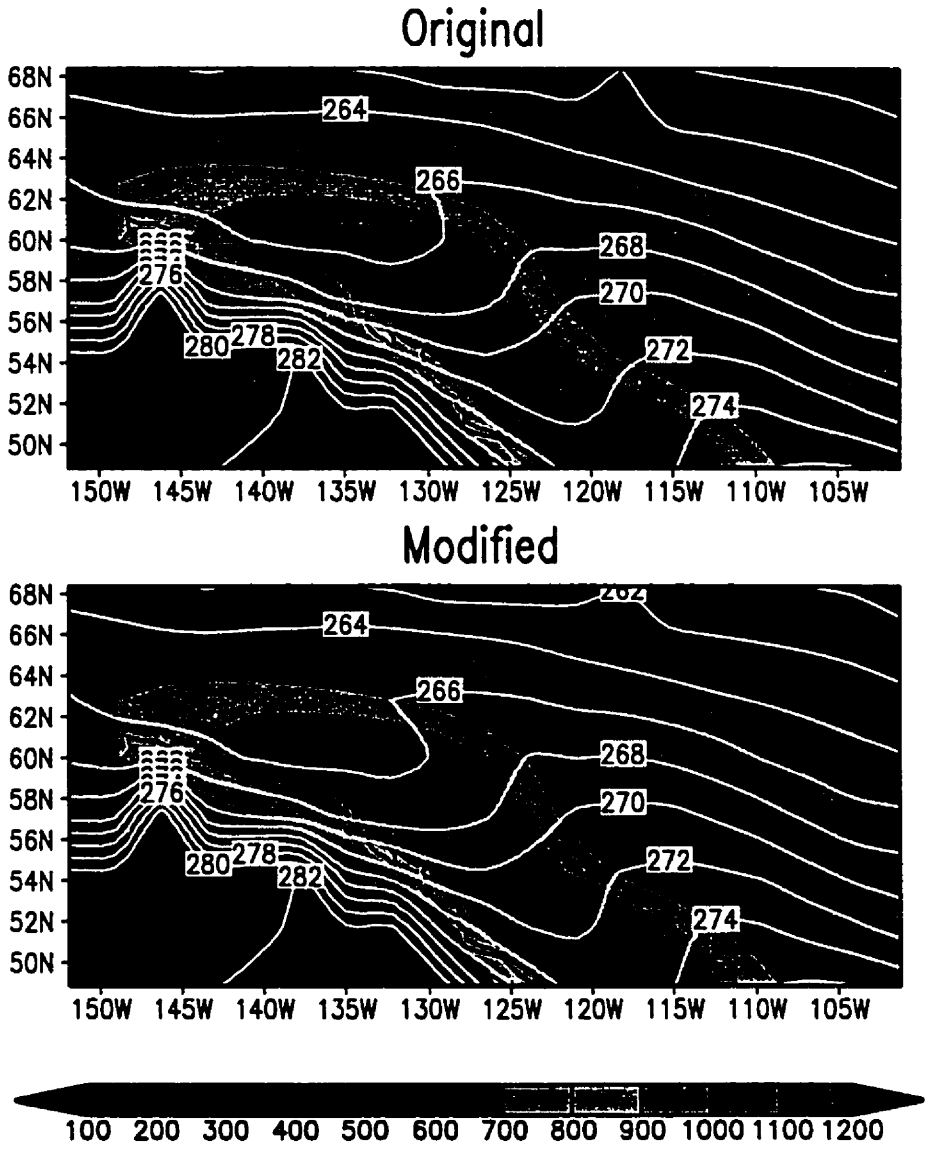

Figure 5.16: Annual average surface temperature (K), comparison between the simulated fields by the original and the modified models.

to the basic thermodynamic structure after the modification is added into the model by checking the zonal averages of atmospheric temperature and specific humidity.

Two of the most basic of all climate properties are the structures of the temperature and water vapor fields. To interpret the simulation quality of these fields, Hack et al. (1998) compared them (from the original CCM3/LSM) to the NCEP/NCAR global reanalyses (Kalnay et al. 1996). As a continuation of his studies, we will compare our modified model result to Hack's results (Hack et al. 1998) to recognize improvements or deficiencies of the modified model.

Figure 5.17 shows the original CCM3/LSM seasonal winter (December, January and February, DJF hereafter) and summer (JJA) zonal averages of temperature difference from the respective NCEP climatology. As Hack et al. (1998) concluded, overall, the original CCM3/LSM does a very good job of reproducing the analyzed thermal structure, where the simulated temperatures are within 1-2K of the analyzed field for the domain bounded by the 50N and 50S and 200mb. The original CCM3/LSM exhibits a weak warm bias in the low to middle portion of the tropical troposphere; and it poorly simulates polar tropopause temperatures which can be 10-14 K colder than analyzed. Cold polar tropopause simulations have been documented to be a pervasive problem in atmospheric general circulation modeling (Boer et al. 1992). Tropical upper troposphere temperatures are also poorly simulated by the original CCM3/LSM. Both seasons exhibit a zonal-mean cold bias of between 3K and 4K at the tropical tropopause. And the simulated temperatures at high latitudes in the lower troposphere are colder than analyzed.

In the comparison between our modified model simulated temperatures and the original model simulated temperatures (Figure 5.18), in winter, the modified model improved much on the simulated temperature at middle and high latitudes in the whole troposphere, by giving a over 1.2K warmer center at the lower troposphere and

another over 1.2K warmer center at the upper troposphere. At the upper troposphere (around 60N, 100mb), the modified model reduced the warm bias in the original model by 0.2K. In the tropical upper troposphere, the modified model improved the temperature simulation by 0.4K. Another improved area is in the middle troposphere between 30N and 30S, where the modified model slightly cools down the warm bias in the original model, with the most significant correction (0.2K) at 30S between 600hPa and 250hPa. A slight warming can also be found in the middle troposphere at the south polar area, where the modified model reduced the cold bias in the original model by over 0.2K. But the modified model slightly increased the cold bias in the upper troposphere at the south polar region by about 1K.

In summer, similar with in winter, the most significant improvement is found again in the north polar region but in the middle and lower troposphere, with a maximum correction of over 0.6K. Another over 0.6K correction is found in the upper troposphere at the south polar area, where the modified model reduced the cold bias in the original model by about 0.6K. The warm bias in the middle and lower tropical troposphere was also slightly reduced by the modified model by 0.1-0.2K, again with a maximum at 30S between 600hPa and 200hPa as in winter. The most exciting point here is that the 0.6K correction at the upper troposphere at the south polar area shows that the modified model also corrected the "cold polar tropopause simulation" by 0.6K, a pervasive problem in many AGCMs claimed by Boer et al. (1992). This correction is at an over 80% significance level as shown in section 5.4. However, the modified model slightly increased the cold bias in the lower troposphere at the south polar region.

The T-test results shown in section 5.4 will show that most of the changes mentioned above are significant.

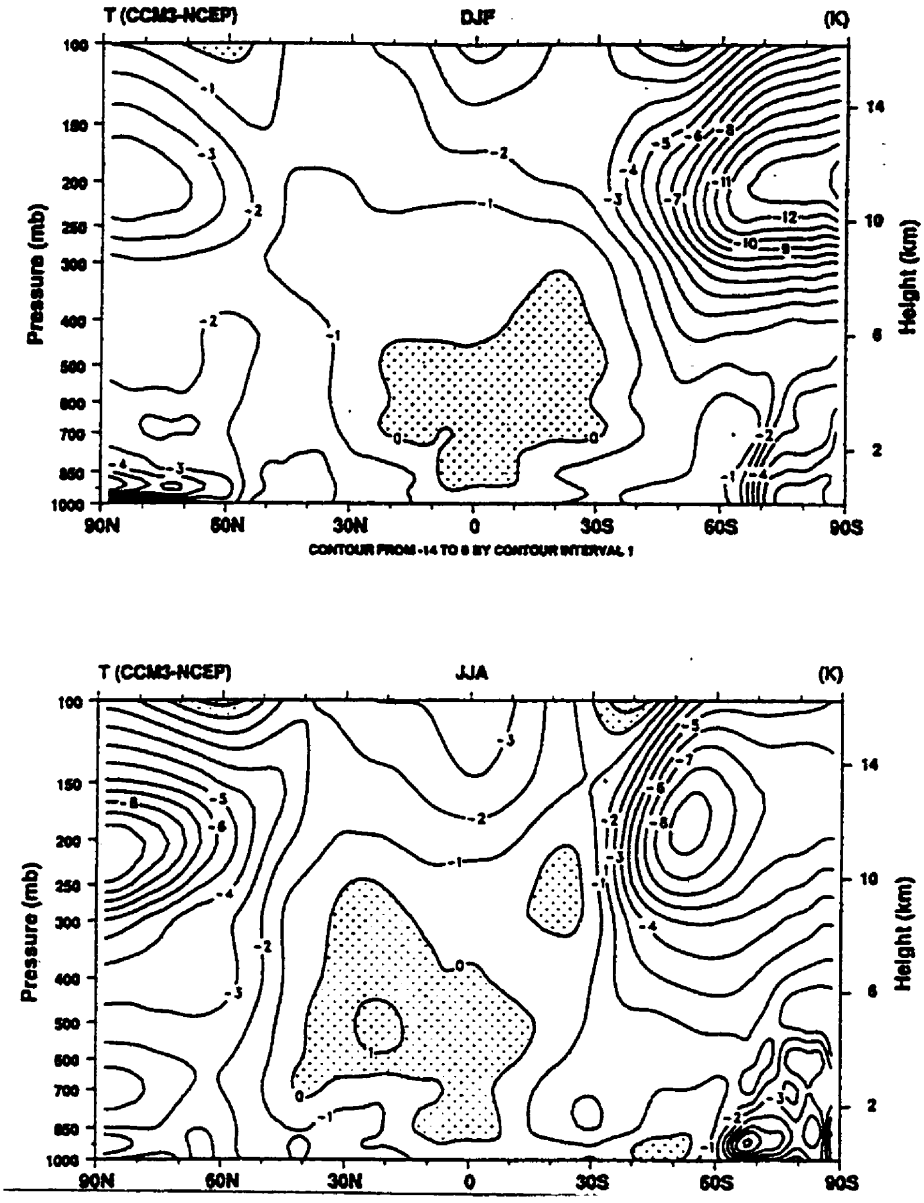

Figure 5.17: Cross section of the seasonal zonal averages of atmospheric temperature(K) for winter (DJF) and summer (JJA), plotted is the difference between the original CCM3/LSM result and NCEP/NCAR reanalyses. (Courtesy of Hack et al. 1998)

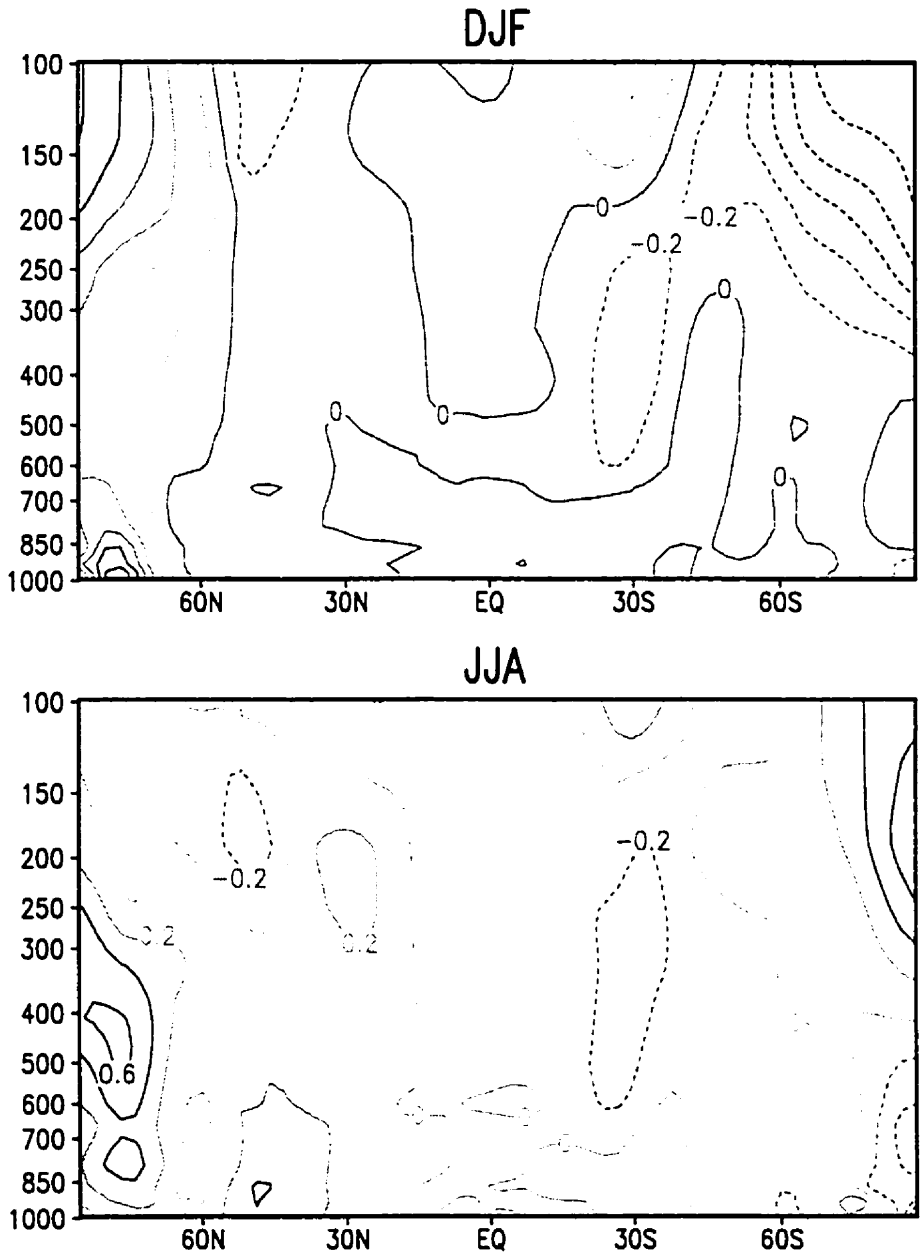

Figure 5.18: Cross section of the seasonal zonal averages of atmospheric temperature(K) for winter (DJF) and summer (JJA), plotted is the difference between the original CCM3/LSM result and the modified model result, i.e. $MODEL_{modified} - MODEL_{original}$.

5.2.5 Atmospheric Humidity

The zonally averaged cross sections of specific humidity differences between the original CCM3/LSM and the NCEP/NCAR reanalyses climatology are shown in Figure 5.19. When compared against the NCEP analysis, the original CCM3/LSM simulated moisture distribution appears to be in a reasonably good agreement. There is evidence of a meridionally broad low-level dry bias on the order of 1 g/kg in both DJF and JJA, with a weak moist bias in the ITCZ. The largest difference appears poleward of 30N during JJA where a pronounced dry bias extends up through the middle troposphere, with maximum values of 3.5 g/kg at 35N near the surface (Hack et al 1998).

Figure 5.20 shows the zonally averaged cross sections of specific humidity differences between the original and the modified CCM3/LSMs. In winter (DJF), the most obvious improvement is found between 15S and 30S at lower troposphere, where the modified model reduced the moist bias in the original model by over 0.15g/kg. Between the equator and 30N the modified model also slightly reduced the moist bias at the lower troposphere. A slight reduction of the dry bias in the original model can also be found at the polar regions. However, the modified model slightly increased the moist bias at the middle tropical troposphere.

In summer (JJA), the modified model reduced the moist bias up to 0.15 g/kg over the equator and the area between 20S and 30S at the lower troposphere. The dry bias at (10S, 600 hPa) and (15N, 850 hPa) is also reduced by the modified model by over 0.03 g/kg. At regions around (50N, 700 hPa) and (75N, 850 hPa), the modified model reduces the dry bias by over 0.06 g/kg. However, the modified model presents no correction on the big dry bias between 30N and 60N in the original model.

Significance check results on these changes in specific humidity brought by the modification can also be found in section 5.4.

Because of the uncertainties in any single analysis of the water vapor field as described in Hack et al. (1998), he also compared the original CCM3/LSM with the National Aeronautics and Space Administration (NASA) Water Vapor Project (NVAP) precipitable water climatology, the vertical integral of the specific humidity. Figure 5.21 shows the zonal- and seasonally averaged precipitable water for the original CCM3/LSM, CCM2/LSM, NVAP and NCEP (Hack et al. 1998). This figure shows a similar meridional bias in the JJA meridional distribution of water vapor, where a pronounced Northern Hemisphere dry bias is clearly indicated by the NVAP data, exceeding $5kgm^{-2}$ (or 5 mm) over most of the region between the equator and 40N.

Because the precipitable water is defined as the vertical integral of the specific humidity, changes in the vertical structure of specific humidity made by the modified model do not necessarily result in much difference in the zonal- and seasonally averaged precipitable water between the modified model and the original model (Figure 5.22). But slight improvement is still visible. In winter, the modified model simulated precipitable water is closer to the NVAP climatology at poleward of 20N, between 5 and 15S, and between 50N and 70N. In summer, the modified model gives better result at regions of poleward of 45N, ITCZ, and between 30S and 50S.

The horizontal distribution of the precipitable water simulated by the original model, and its difference from the NVAP dataset are shown in Figure 5.23 and 5.25 for DJF and JJA respectively. The CCM3/LSM produces relatively minor seasonal changes in the precipitable water distribution except over Amazon Basin, central Africa, and in vicinity of the Indian subcontinent. These seasonal excursions of the meridional maximum in precipitable water are primarily responsible for the meridional shifts seen in the zonal mean. Despite relatively good agreement in the zonal mean values, there are some significant regional differences between the original model

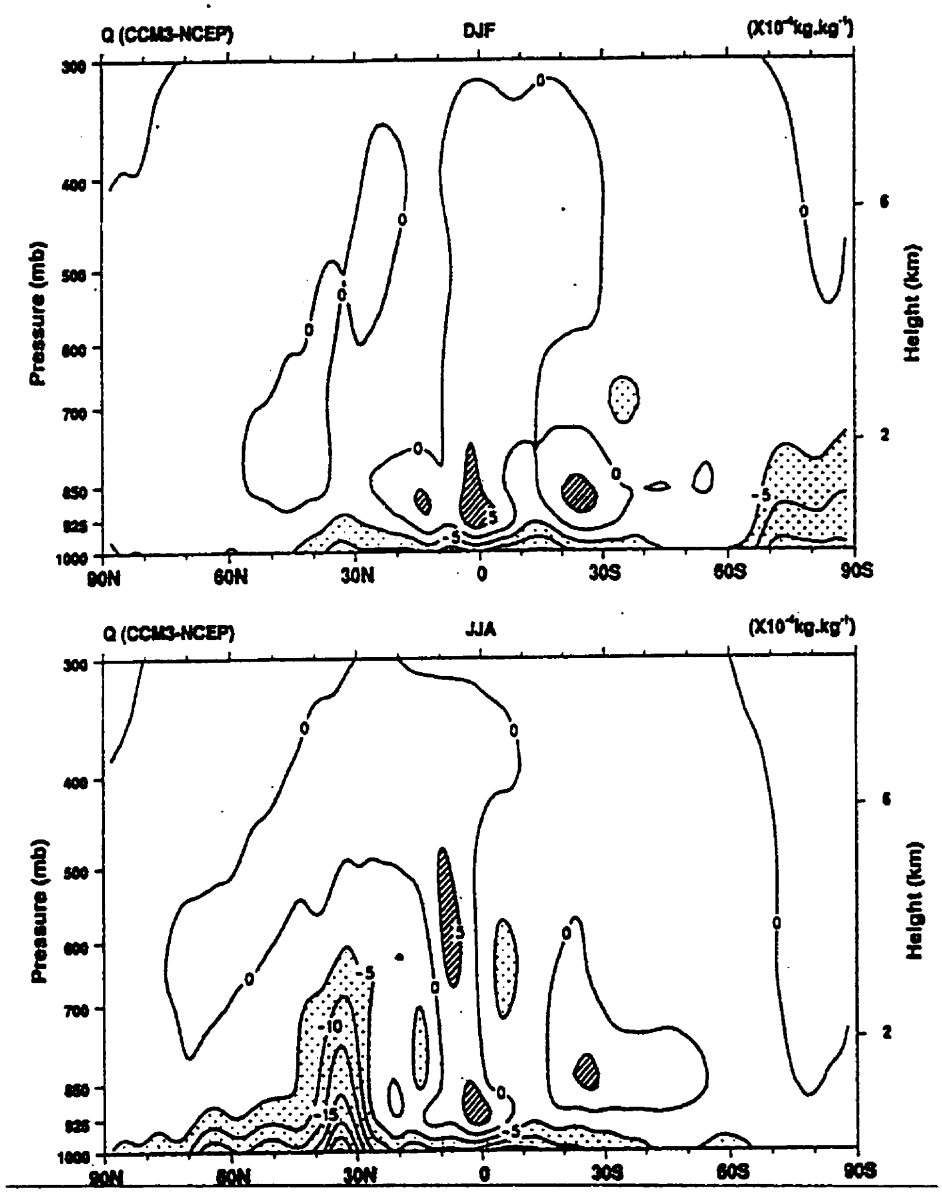

Figure 5.19: Cross section of the seasonal zonal averages of specific humidity ($\times 10^{-4}$ Kg/Kg) for winter (DJF) and summer (JJA), plotted is the difference between the original CCM3/LSM result and NCEP/NCAR reanalyses. (Courtesy of Hack et al. 1998)

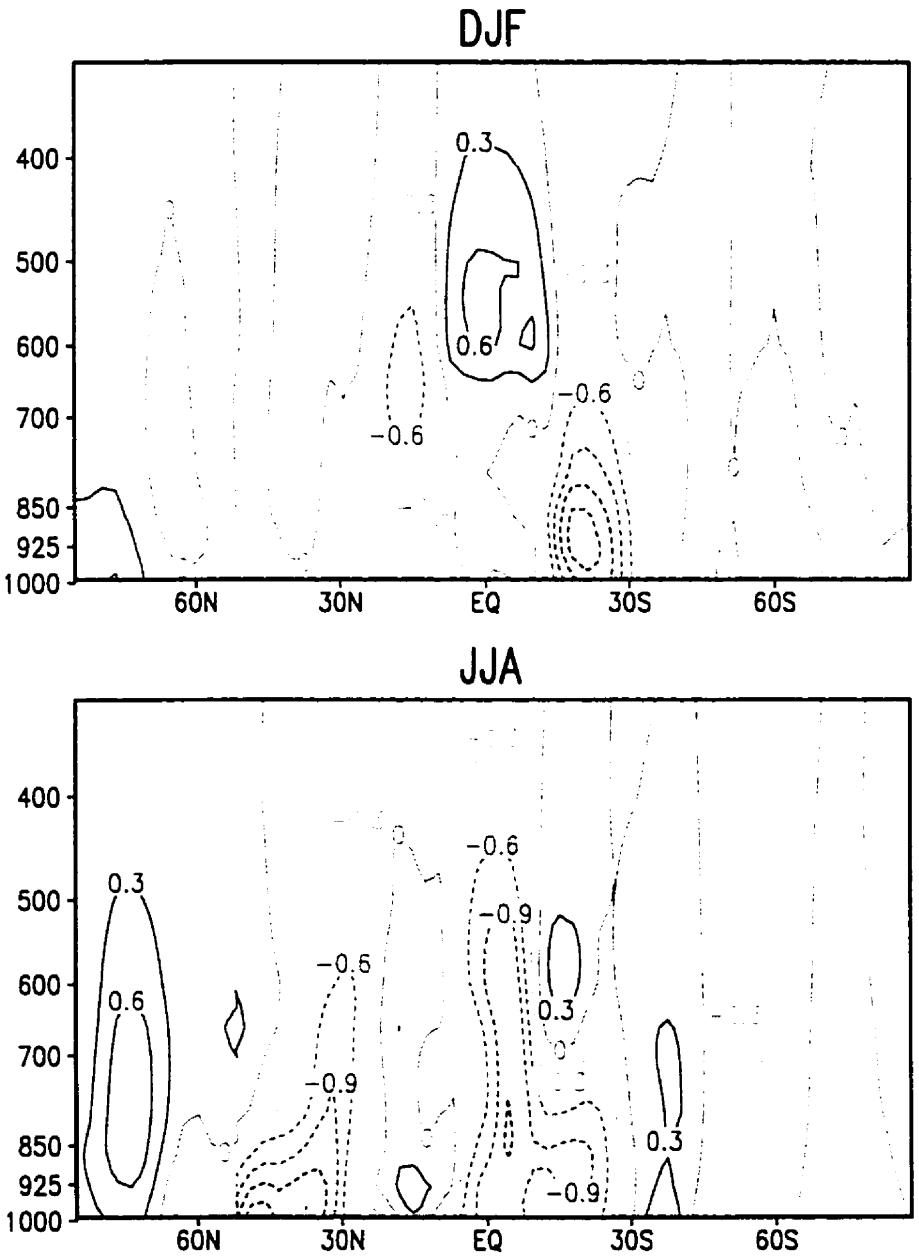

Figure 5.20: Cross section of the seasonal zonal averages of specific humidity ($\times 10^{-4}$ Kg/Kg) for winter (DJF) and summer (JJA), plotted is the difference between the original CCM3/LSM result and the modified model result, i.e. $MODEL_{modified} - MODEL_{original}$.

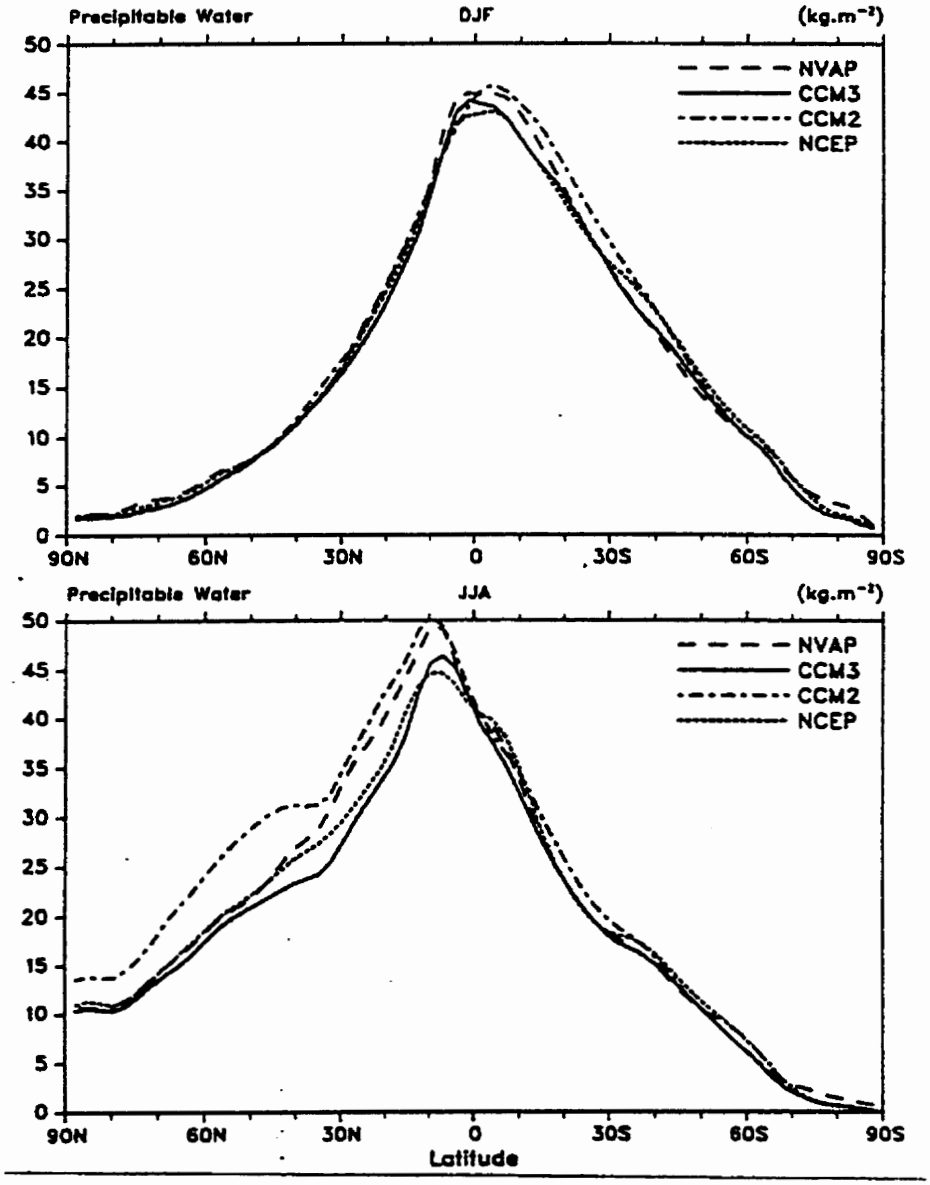

Figure 5.21: zonal- and seasonally averaged precipitable water (Kgm^{-2}) for the original CCM3/LSM, CCM2/LSM, NVAP and NCEP for winter (DJF) and summer (JJA). (Courtesy of Hack et al. 1998)

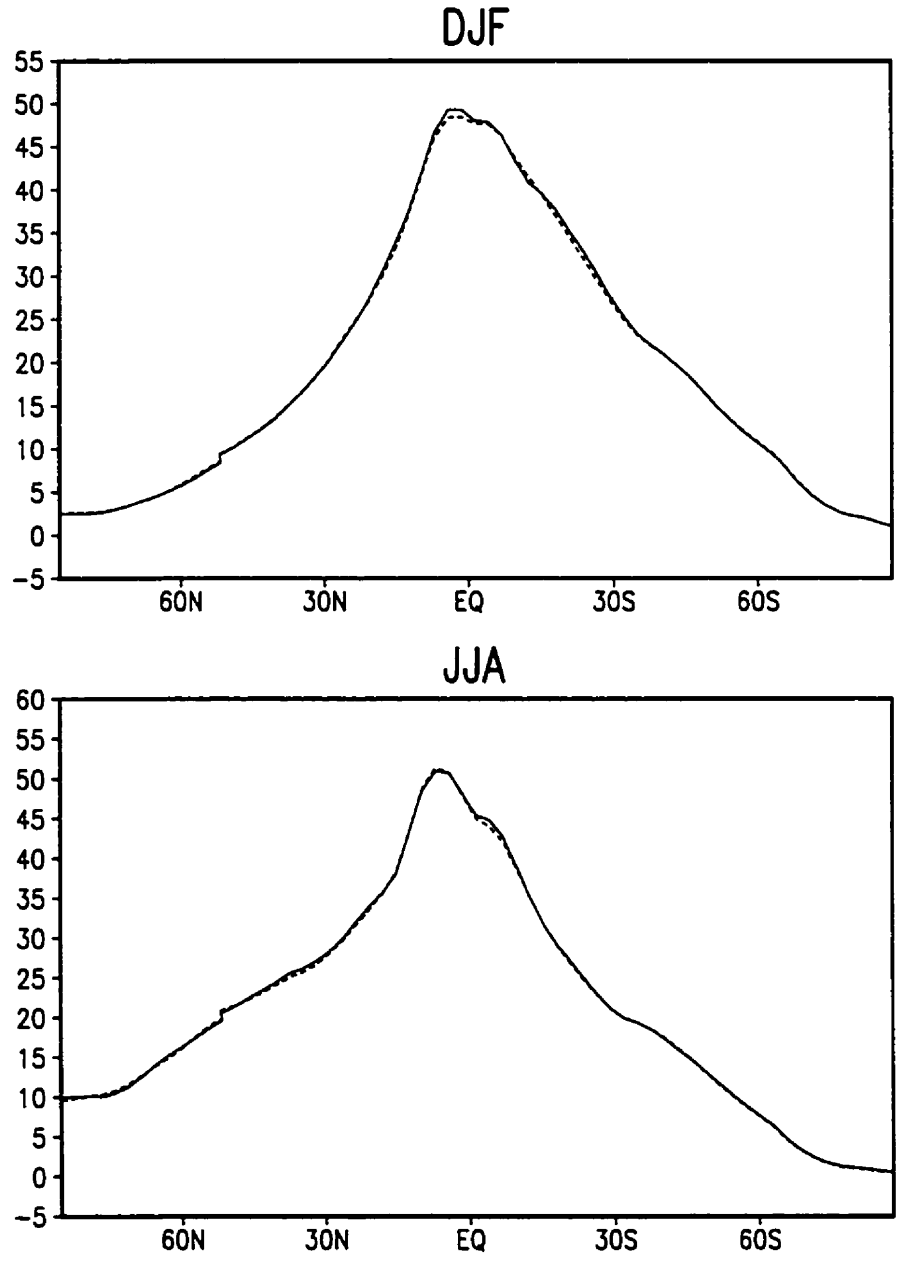

Figure 5.22: zonal- and seasonally averaged precipitable water (Kgm^{-2})for winter (DJF) and summer (JJA), the solid line is for the original CCM3/LSM and the dashed line is for the modified model.

simulated water vapor field and the NVAP. The DJF simulation shows a large spatially coherent dry region stretching from the southern Indian Ocean eastward through the South Pacific convergence zone (SPCZ), and a second feature extending across the equatorial Atlantic, Northern Africa, and into Northern India. These differences typically exceed 6 mm, representing approximately a 15% - 20% error. Similar, but more severe, regional differences are seen in the JJA simulation. The atmosphere over warm continental surface appears to be systematically dry, exceeding 10 mm over large areas, where these differences represent local errors of 30% or more. Even oceanic regions exhibit a significant dry anomaly, as seen in JJA over much of the western Pacific.

The horizontal distribution of the precipitable water simulated by the modified model, and its difference from the original model simulation are shown in Figure 5.24 and 5.26 for DJF and JJA respectively. In the DJF simulation, the most significant improvement can be found in Australia by about 2.5mm, and the vicinities of the Tibet Plateau by 1mm. There are also some slight improvements in other areas. In the summer simulation, the difference between the modified and the original models appears larger than in the winter simulation because the modification is directly related to precipitation. The modified model gives very obvious correction in North America at the east coast of the United States, in China - Russia area, especially at the vicinity of the Tibet Plateau, in Central Africa, east part of Amazon basin and slight correction at the central equatorial area. These corrections reduce the errors discussed in the original model.

From the above two graphs, especially the JJA precipitable water plot, one can easily find that the modified model basically gives less precipitable water over high topography (the Rockies, Andes, and Tibet Plateau) and more precipitable water at the feet of these high topography. Changes in other areas, especially over the ocean,

might be related to the changes in the atmospheric general circulations, which will be discussed in section 5.4.

5.2.6 Evaporation and Precipitation

The evaporation and precipitation fields illustrate the properties of water exchange between the atmosphere and the underlying surface. The zonally and annually averaged evaporation rate and $E-P$ are shown in Figure 5.27 (where a comparable global observational dataset does not exist). For this period (1987-1994), the evaporation curves show that the most vigorous transfer of water to the simulated atmosphere occurs between 30S and 70N, with maxima around 50N, the ITCZ and 20S. This pattern is slightly different from a typical pattern from a long-term CCM3 simulation , which exhibits well-pronounced evaporation maxima near 20N and 20S (Hack et al. 1998). However, the consistency between this study and previous studies on the precipitation horizontal distribution for this period will convince readers that the model performs properly (see the simulated ENSO response section). The modified model reduced the evaporation between 50N and 30S. The enhanced suppression of evaporation in the vicinity of ITCZ convection is a more realistic feature of the CCM3/LSM simulation, showing good agreement with corresponding oceanic estimates (e.g., see Oberhuber 1988; Doney et al. 1998; Kiehl 1998).

Because of the reduced evaporation, the modified model also reduced the zonal annually averaged $E-P$ (bottom panel in Figure 5.27) while keeping the same pattern as from the original model. The regions 20N - 70N and 15N - 30N are well-defined source regions of total water, where the deep Tropics and extratropics represent regional sinks of total water. The modified model slightly reduced the source regions of total water.

The zonally and annually averaged precipitation rate is shown in Figure 5.28

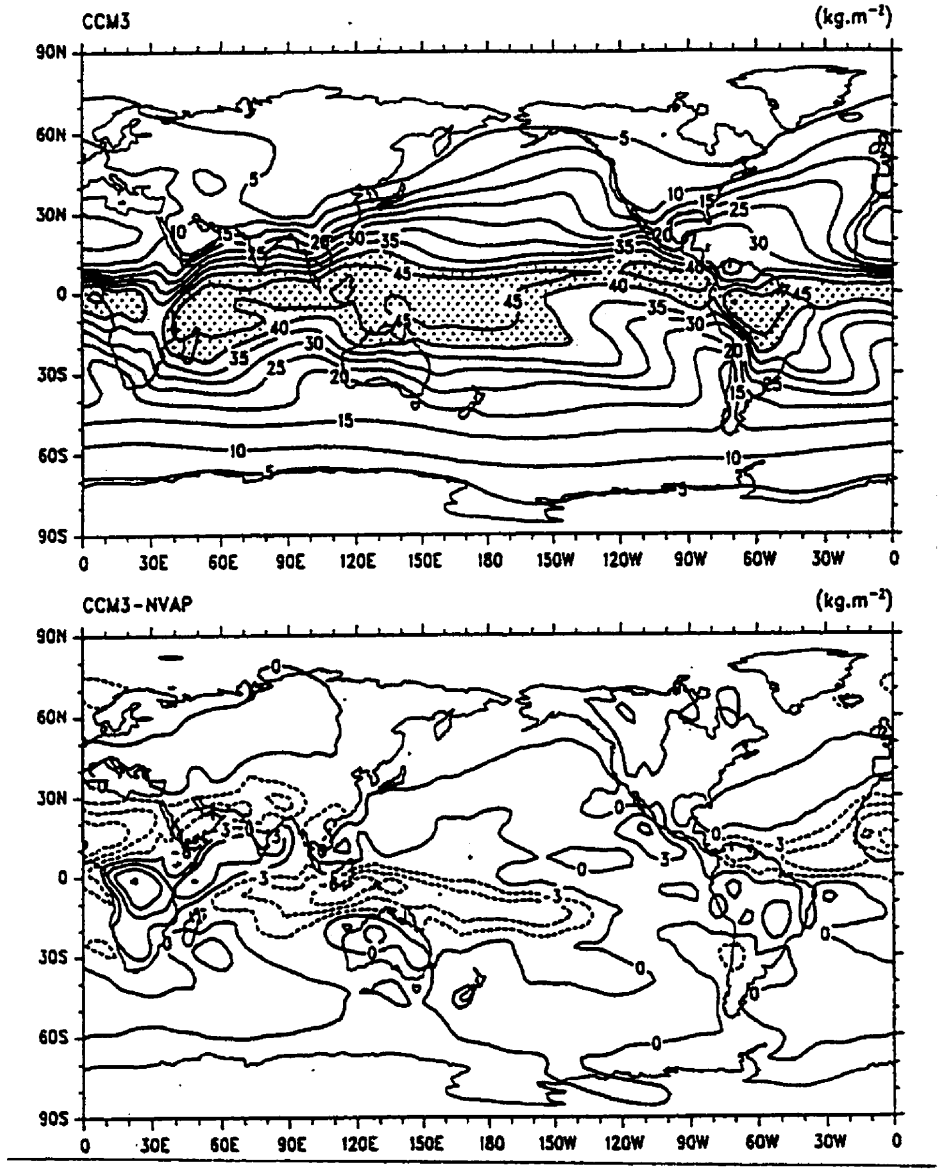

Figure 5.23: Global distribution of precipitable water (Kgm^{-2}) simulated by the original CCM3/LSM, for DJF (top panel) and the difference with respect to the NVAP analysis. (Courtesy of Hack et al. 1998)

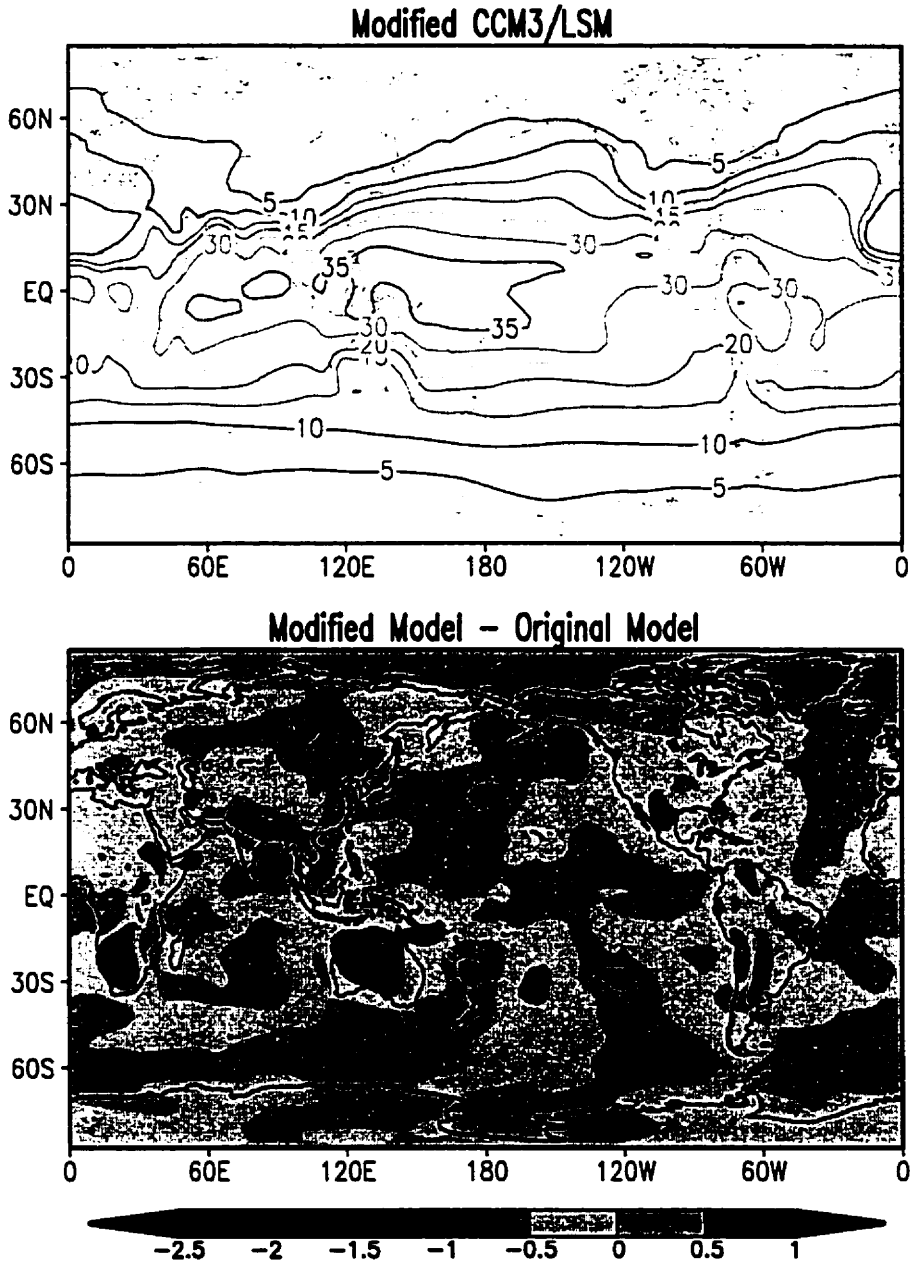

Figure 5.24: Global distribution of precipitable water (Kgm^{-2}) simulated by the modified CCM3/LSM (top panel), and the difference with respect to the original model result, i.e. $MODEL_{modified} - MODEL_{original}$ (bottom panel), for DJF.

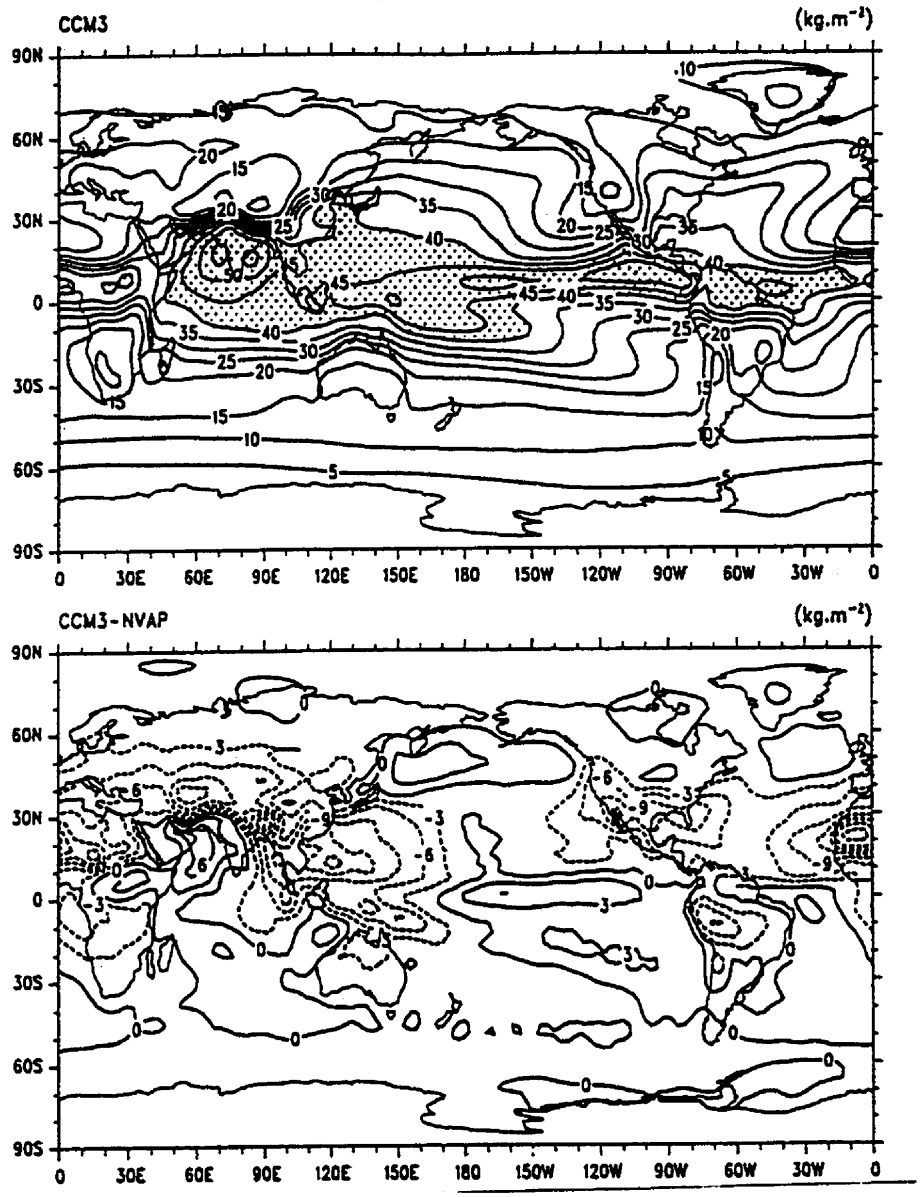

Figure 5.25: Global distribution of precipitable water (Kgm^{-2}) simulated by the original CCM3/LSM, for JJA (top panel) and the difference with respect to the NVAP analysis. (Courtesy of Hack et al. 1998)

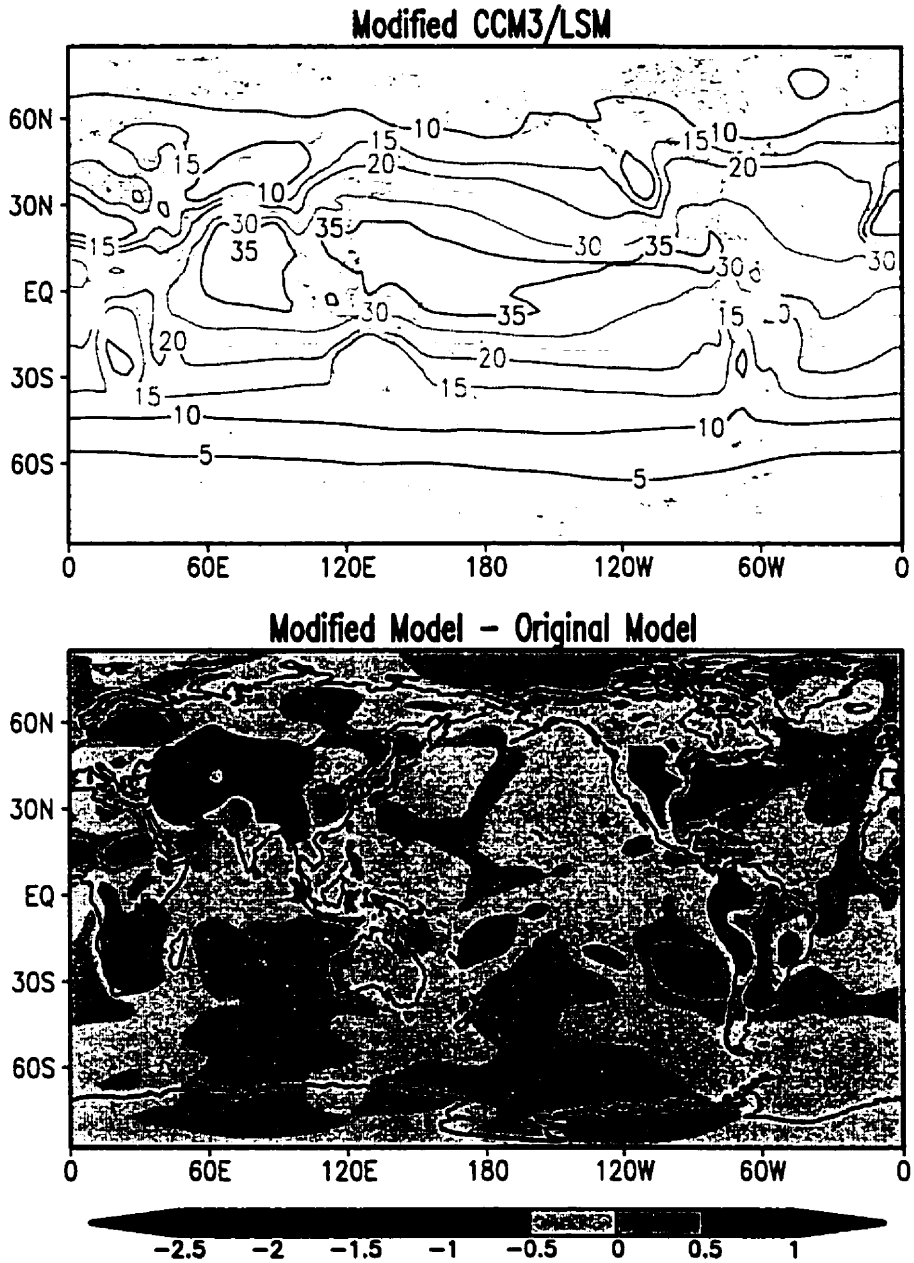

Figure 5.26: Global distribution of precipitable water (Kgm^{-2}) simulated by the modified CCM3/LSM (top panel), and the difference with respect to the original model result, i.e. $MODEL_{modified} - MODEL_{original}$ (bottom panel), for JJA.

for the original CCM3/LSM, modified CCM3/LSM and the Xie and Arkin (1996) analysis. Generally the original CCM3/LSM overestimates the precipitation rate except at the ITCZ as shown in the upper panel. While the modified model drags the curves closer to the Xie and Arkin (1996) analysis at most of the Northern Hemisphere and some areas in Southern Hemisphere, as shown in the lower panel. The most significant improvement can be found between 15N and 60N, and between the equator and 60S.

As seen in the seasonal mean(Figure 5.29), the modified model significantly reduced the evaporation between 20S and 30S, at the ITCZ, and between 10N and 40N in DJF, and between 30N and 60N in JJA, where the maxima occur for corresponding seasons. This figure also shows some difference from Hack et al (1998). The evaporation in the tropics is small for both seasons, especially in the JJA, when the peak is between 30N and 60N.

The seasonal zonal averages of precipitation rate (Figure 5.30) shows similar patterns with the annual mean (Figure 5.28) with slightly bigger difference than that between the original CCM3/LSM and the Xie and Arkin (1996) analysis. The original model simulated precipitation rates are generally overestimated in most regions, especially in the midlatitude storm track regions. The modified model slightly improves the patterns by increasing (decreasing) the precipitation rate at the underestimated (overestimated) areas by the original model (Figure 5.31). In DJF, the modified model improved the precipitation rate in most of the region between 30S and 30N. In summer, besides for the tropics, improvement can also be found in the midlatitude storm track areas.

The changes to both evaporation and precipitation produce differences in the seasonal distribution of the net water exchange ($E - P$) at the surface between the modified and the original models (see Figure 5.32). Both the original and the modified

models produced a weaker source of total water between 15S and 35S during the Northern Hemisphere winter months and a very strong source region between 30N and 75N during the Northern Hemisphere summer months. The modified model slightly reduced the strength of the source regions of total water where maxima occur.

Figures 5.33 and 5.35 show the DJF and JJA global distribution of precipitation for the Xie and Arkin climatology and the original CCm3/LSM simulation (Hack et al. 1998). The comparison between the original and the modified models is shown in Figures 5.34 and 5.36. Overall, the original CCM3/LSM does a very credible job of simulating the principal features of the observed precipitation distribution (see details in Hack et al. 1998). However, a number of significant biases are apparent in the original model simulated seasonal structures. In Figure 5.33, the original model gives an anomalous precipitation maximum in the DJF pattern, in the western tropical Pacific, positioned well north of the observed precipitation maximum. The modified model corrected it by about 3 mm/day (Figure 5.34). Vigorous ITCZ convection extends too far east in the Pacific Ocean, and convection in the Indian Ocean is positioned too far to the north with evidence of a double ITCZ not reflected in the observational data, where the modified model corrected it again by 1 - 2 mm/day. Western Pacific convection extends too far south into northwestern Australia, where the modified model corrected it by 3 mm/day. And the original model tends to lock precipitation over the Andes Mountains, a problem in many other AGCMs (Hack et al. 1998). But the modified model corrected it by 2 mm/day. This improvement is directly related to topographic effects, and illustrates that the modified LSM with more detailed topographic effects included gives a more realistic AGCM climate. Other improvements can also be found at other locations, such as the overestimate tail in the southern Indian Ocean.

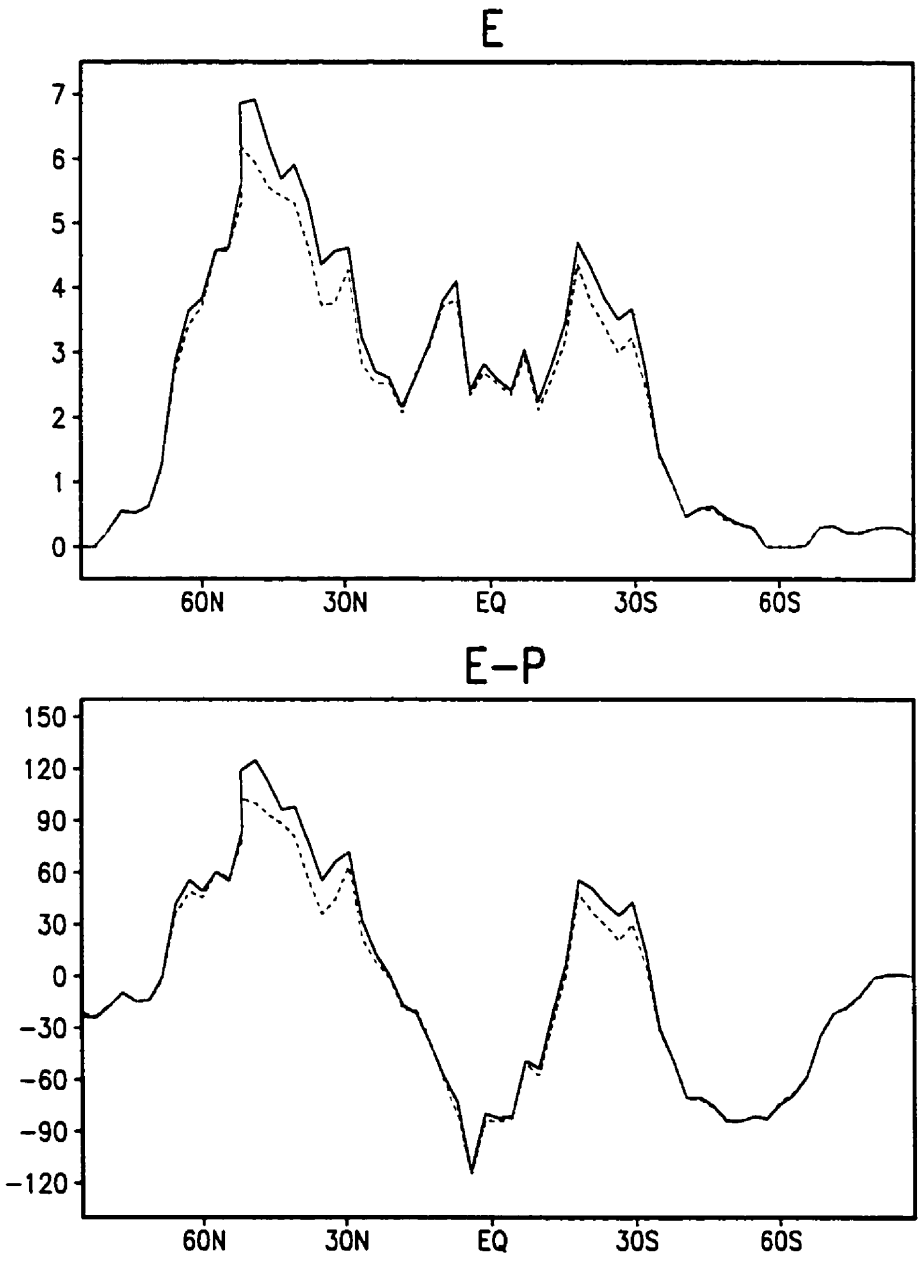

Figure 5.27: Zonally annually averaged evaporation rate (mm/day) (upper panel) and $E - P$ ($W\ m^{-2}$) (lower panel) simulated by the original(solid line) and the modified models.

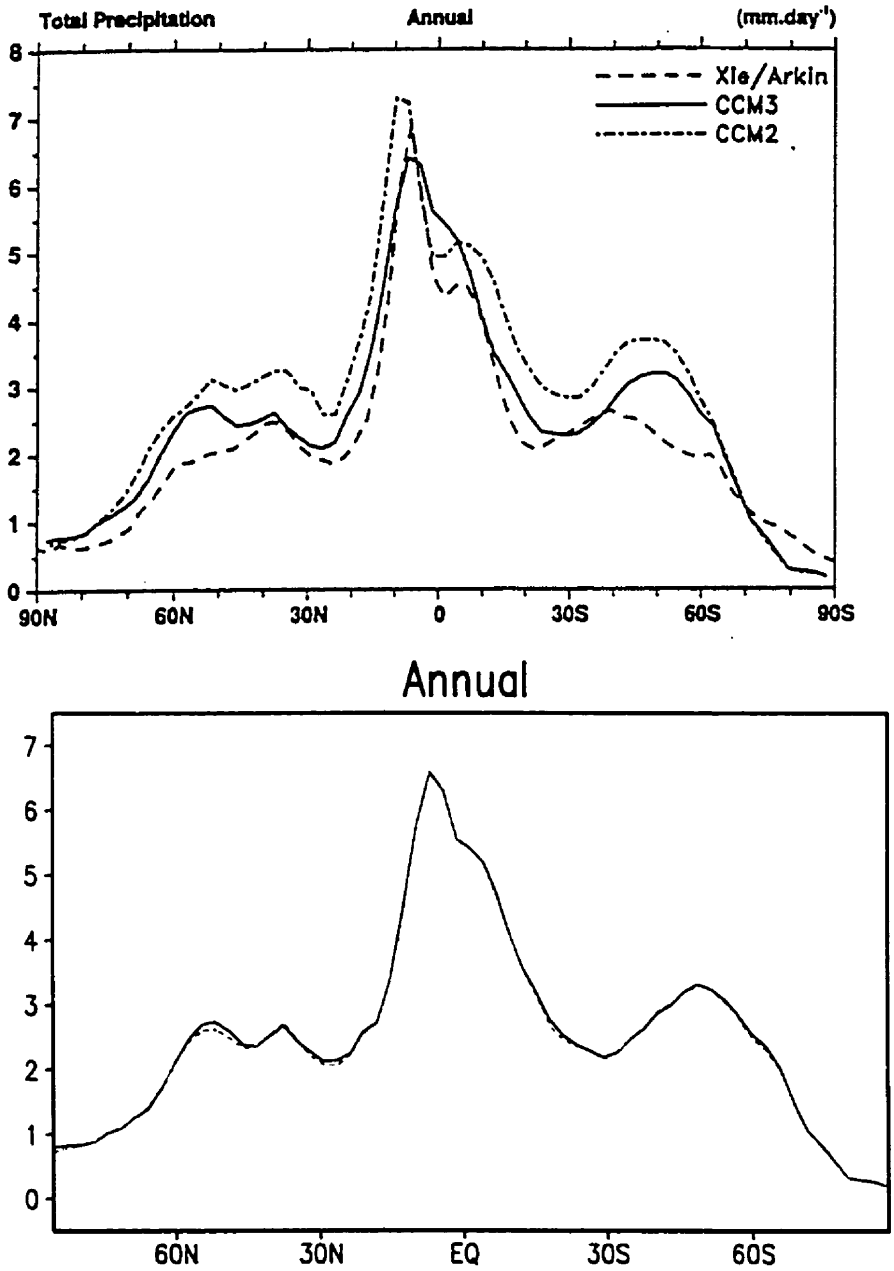

Figure 5.28: Zonally annually averaged precipitation rate (mm/day) for the original CCM3/LSM and Xie and Arkin (1996) (Courtesy of Hack et al. 1998), and the comparison between the original (solid line) and modified models (lower panel).

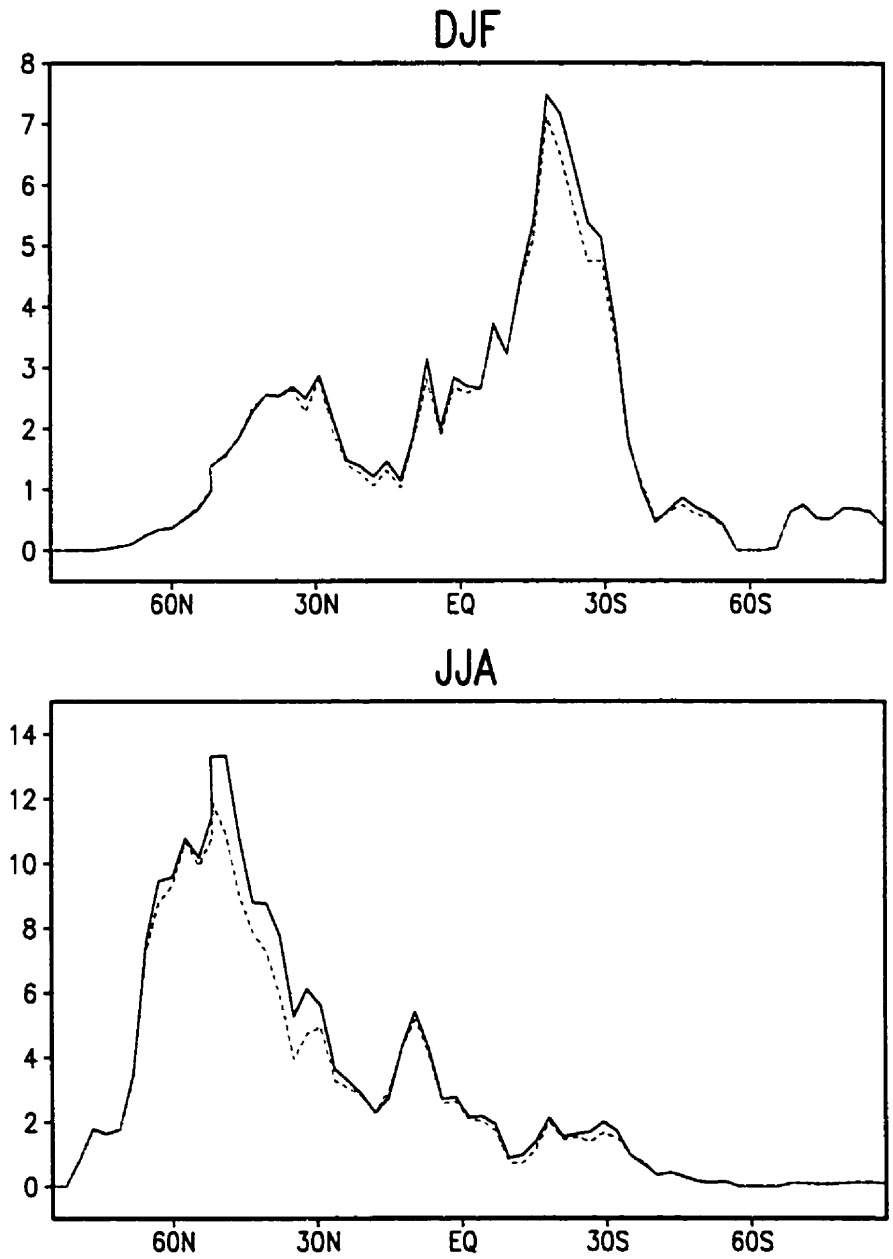

Figure 5.29: Zonally and seasonally averaged evaporation rate (mm/day) for DJF and JJA simulated by the original (solid line) and the modified models.

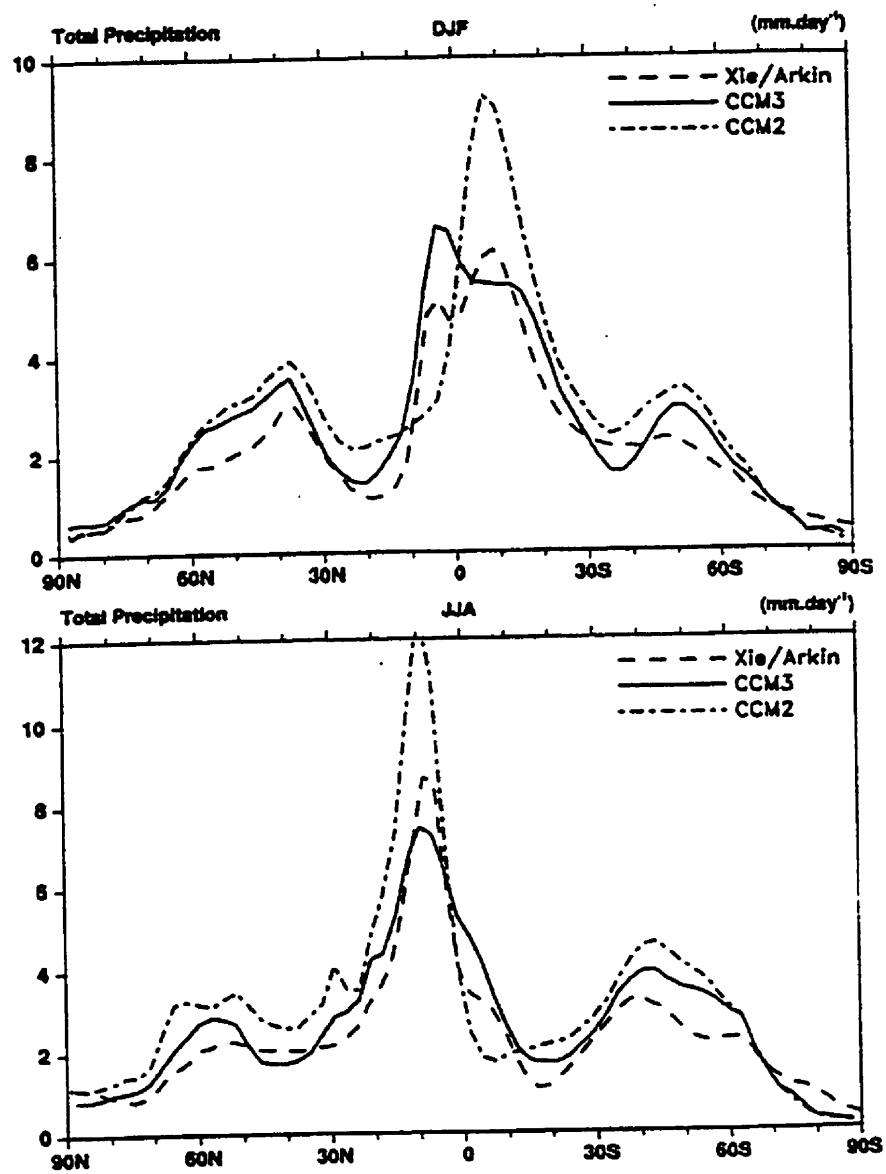

Figure 5.30: Zonally and seasonally averaged precipitation rate (mm/day) in DJF and JJA, for the original CCM3/LSM and Xie and Arkin (1996) (Courtesy of Hack et al. 1998).

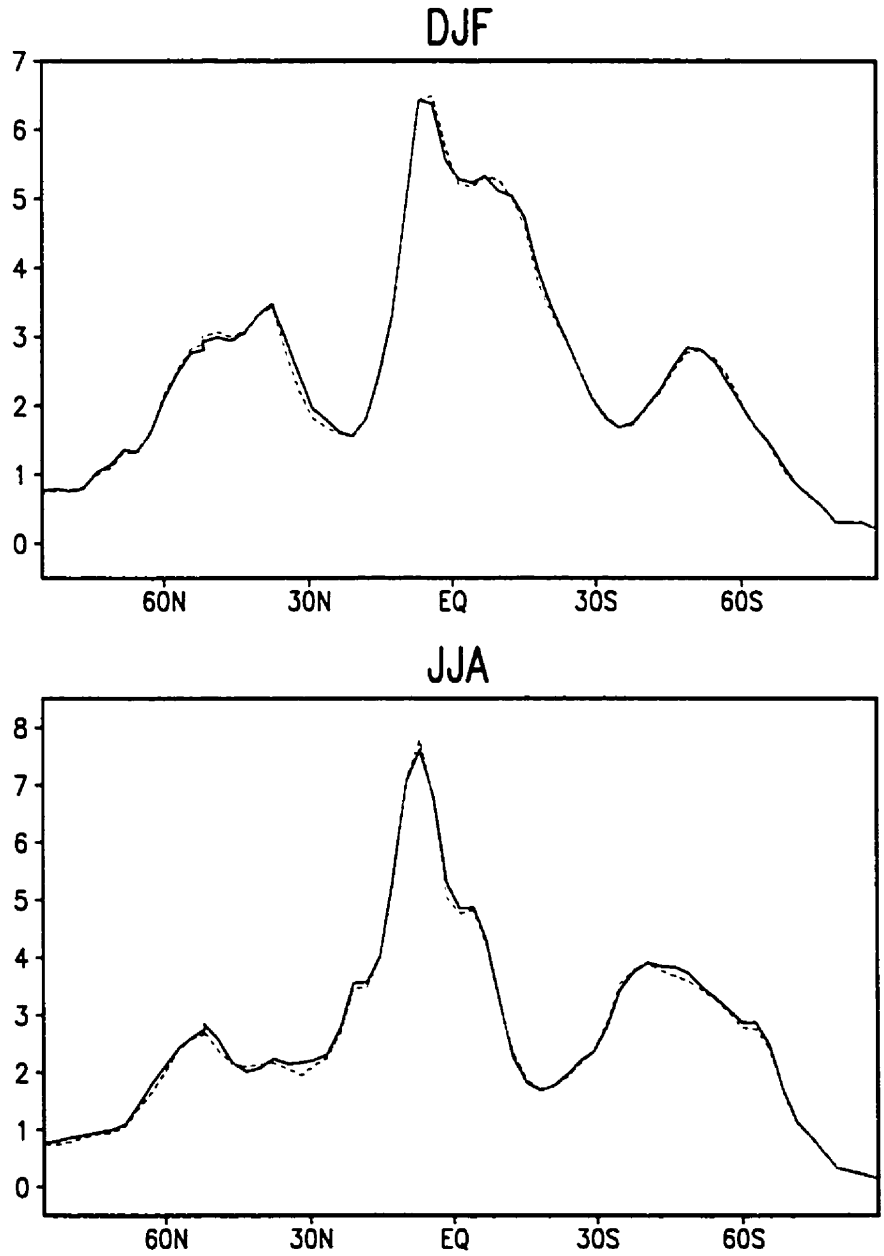

Figure 5.31: Zonally and seasonally averaged precipitation rate (mm/day) in DJF and JJA, for the original CCM3/LSM (solid line) and the modified model.

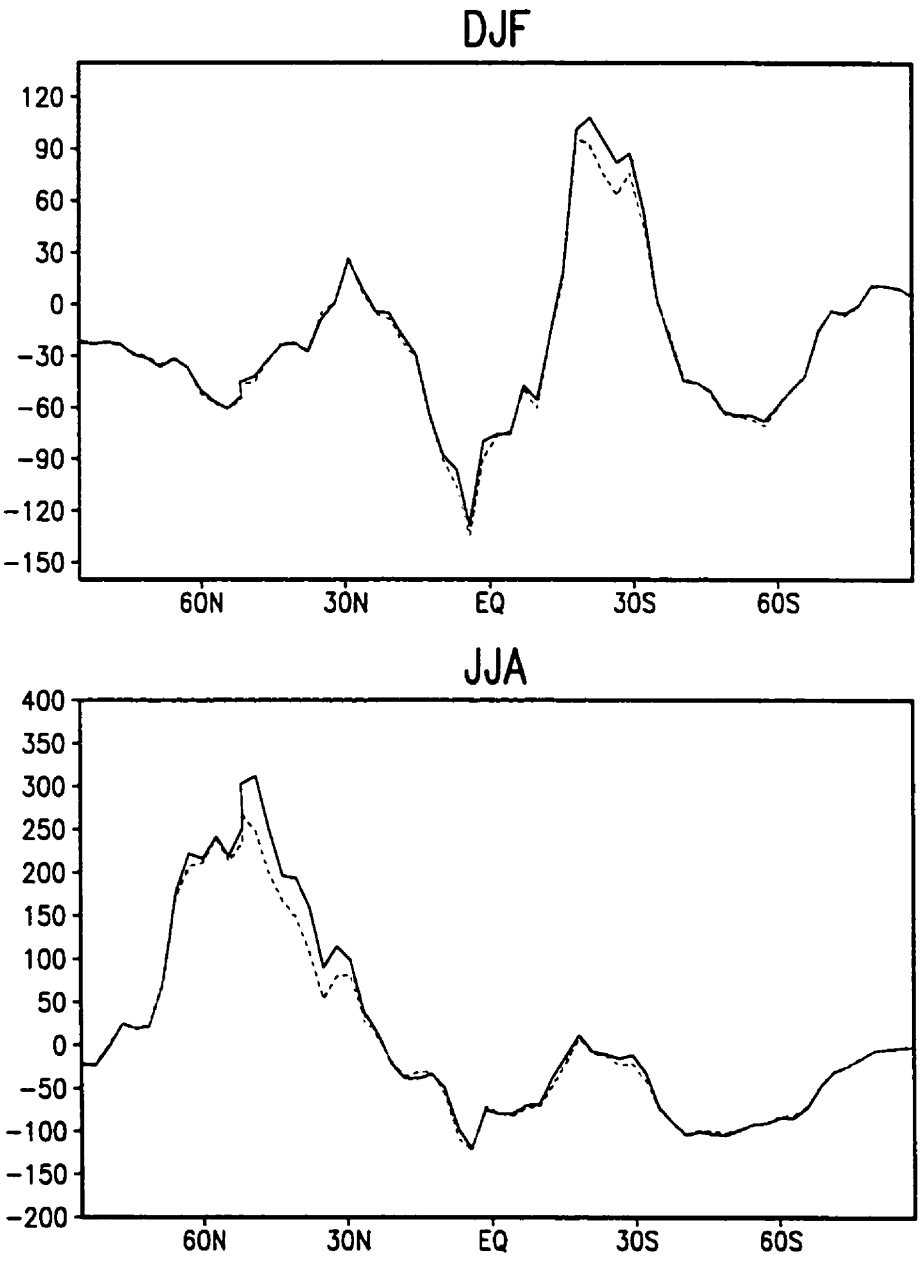

Figure 5.32: Zonally and seasonally averaged net water exchange rate$(E-P)$ (Wm^{-2}) for DJF and JJA simulated by the original (solid line) and the modified models.

In the original model simulation, the JJA distribution (Figure 5.35) shows excessive convective activity over central America erroneously extending eastward into the Caribbean, with weaker than observed precipitation in the eastern Atlantic. Slight improvement can be found in the modified model with a magnitude of about 1-2 mm/day at these locations (Figure 3.38). There is also an anomalous precipitation maxima over the Arabian Peninsula in the original model simulated precipitation, where the modified model corrected it by about 2 mm/day. The modified model also corrected the unrealistic meridional separation of the ITCZ in the west-central Pacific given by the original model, by a long high band of up to 3 mm/day in Figure 5.36 (lower panel). The anomalous precipitation maximum in the north subtropical central Pacific was corrected by the modified model by about 2 mm/day. Another improvement can be found around the Tibet Plateau, where the original model gives an anomalous precipitation maximum, and the modified model corrected it by about 2 mm/day, and gives more precipitation at the east side of the Plateau. This pattern is closer to the observed one. This is another example illustrating that the inclusion of topographic effects into the LSM makes the AGCM more realistic.

5.2.7 Simulated ENSO Response

The AGCM simulated ENSO response can be illustrated by examining the longer-term average precipitation differences between a warm and cold event, an analysis technique that helps to maximize the observed response (Hack et al. 1998). Figure 5.37 shows the seasonal differences between DJF 1987 and DJF 1989 (i.e., warm minus cold event) for the Xie and Arkin precipitation data and the original CCM3/LSM result (Hack et al. 1998). And the modified model result and the differences between the modified and the original models are shown in Figure 5.38. Comparison between

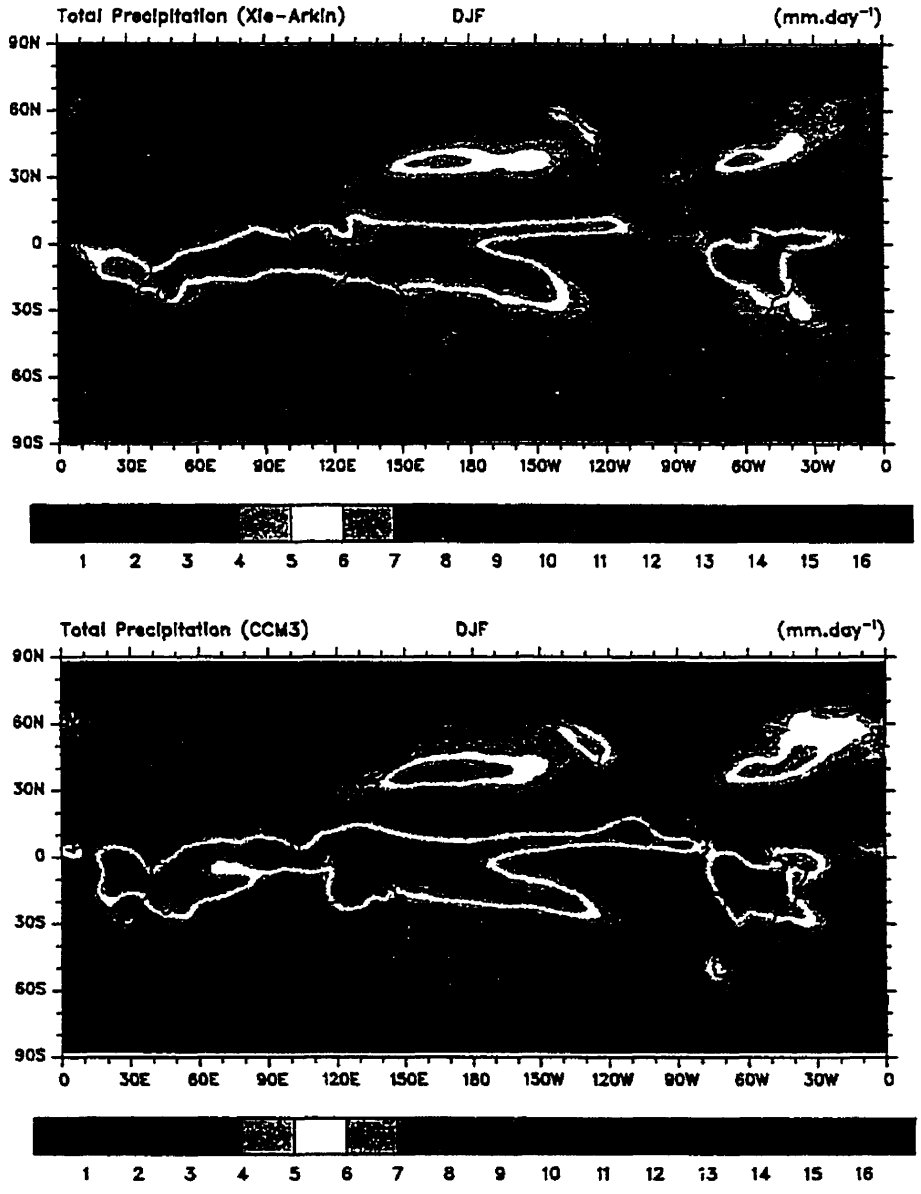

Figure 5.33: Global DJF distribution of precipitation rate (mm/day) for the Xie and Arkin (1996) precipitation climatology, and as simulated by the original CCM3/LSM. (Courtesy of Hack et al. 1998)

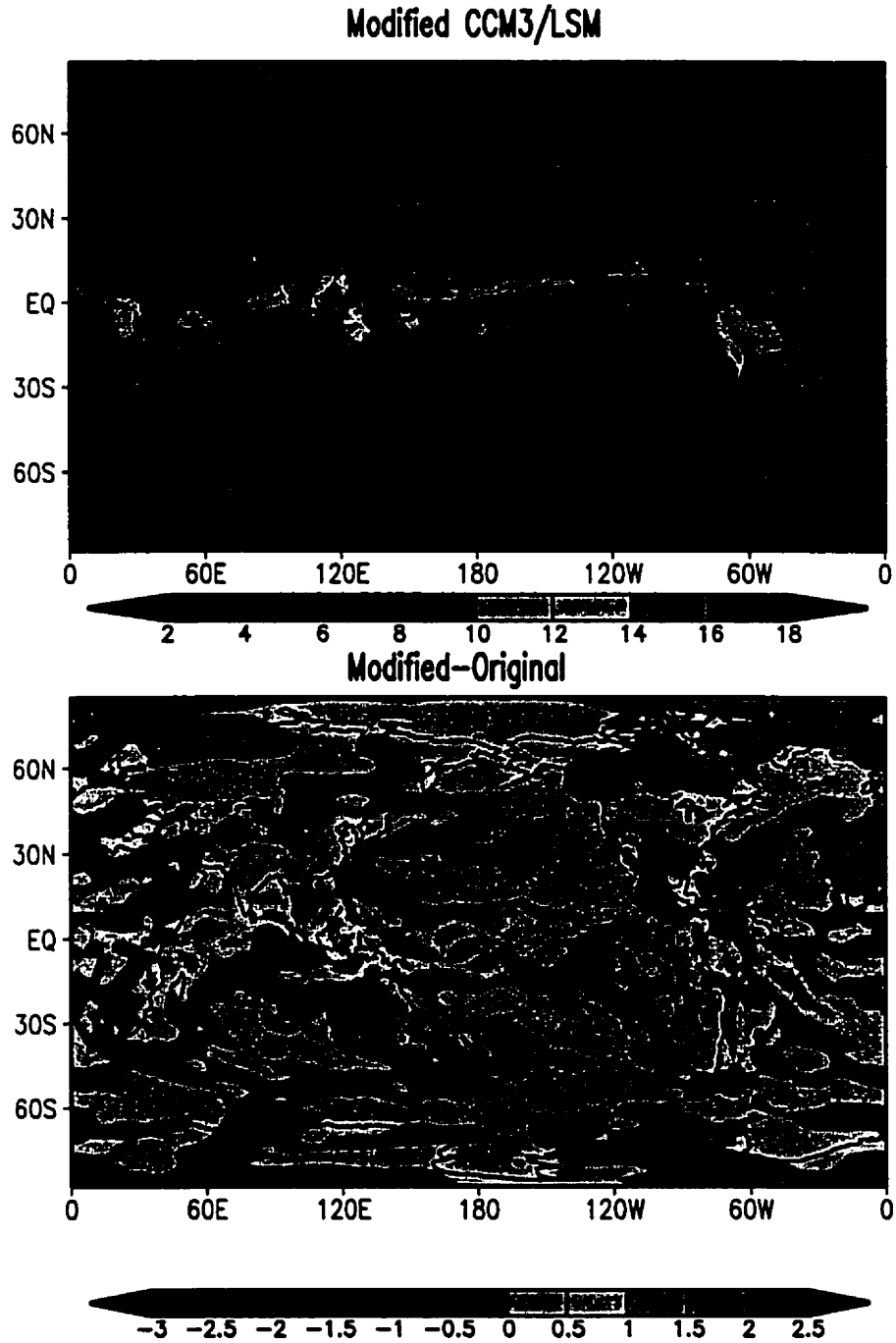

Figure 5.34: Global DJF distribution of precipitation rate (mm/day) for the modified model and the difference between the modified and the original models (lower panel).

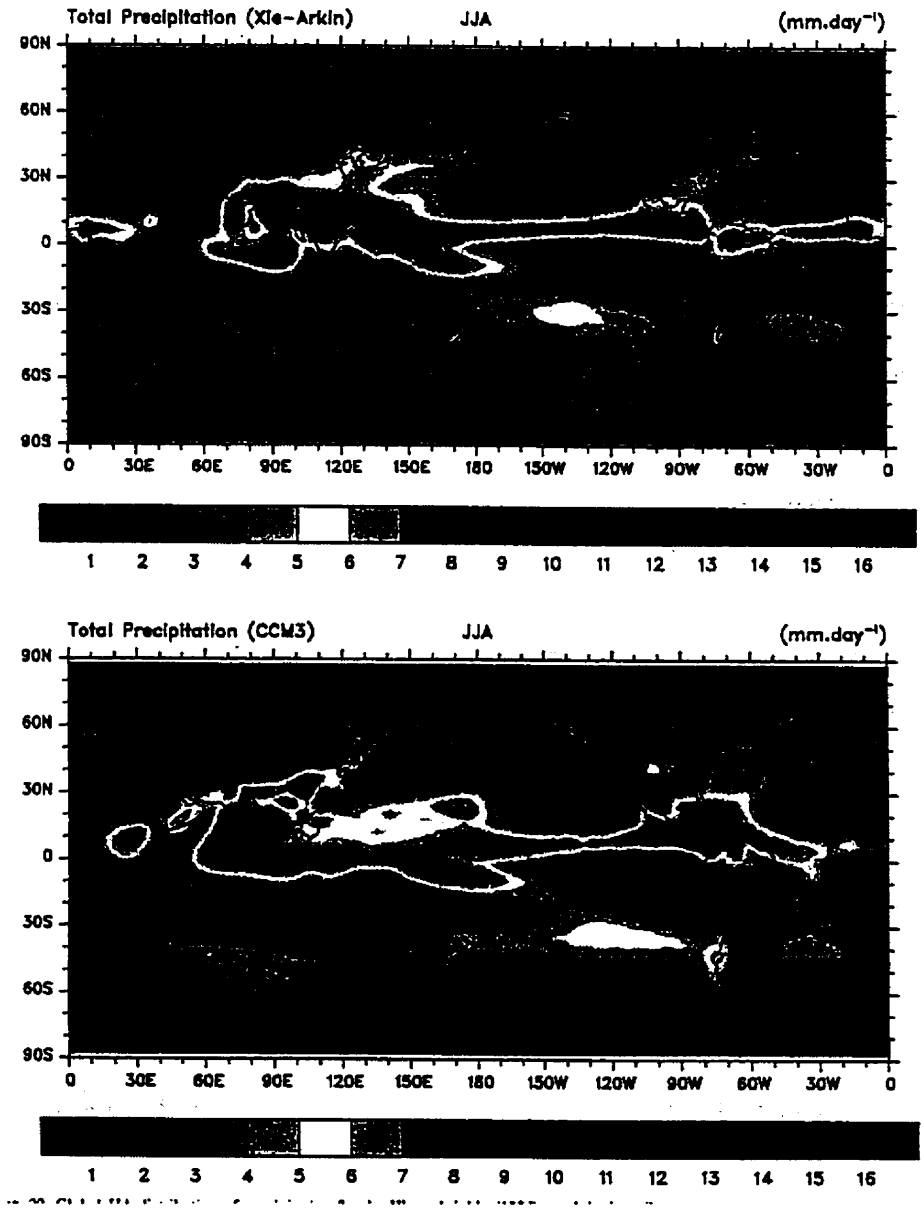

Figure 5.35: Global JJA distribution of precipitation rate (mm/day) for the Xie and Arkin (1996) precipitation climatology, and as simulated by the original CCM3/LSM. (Courtesy of Hack et al. 1998)

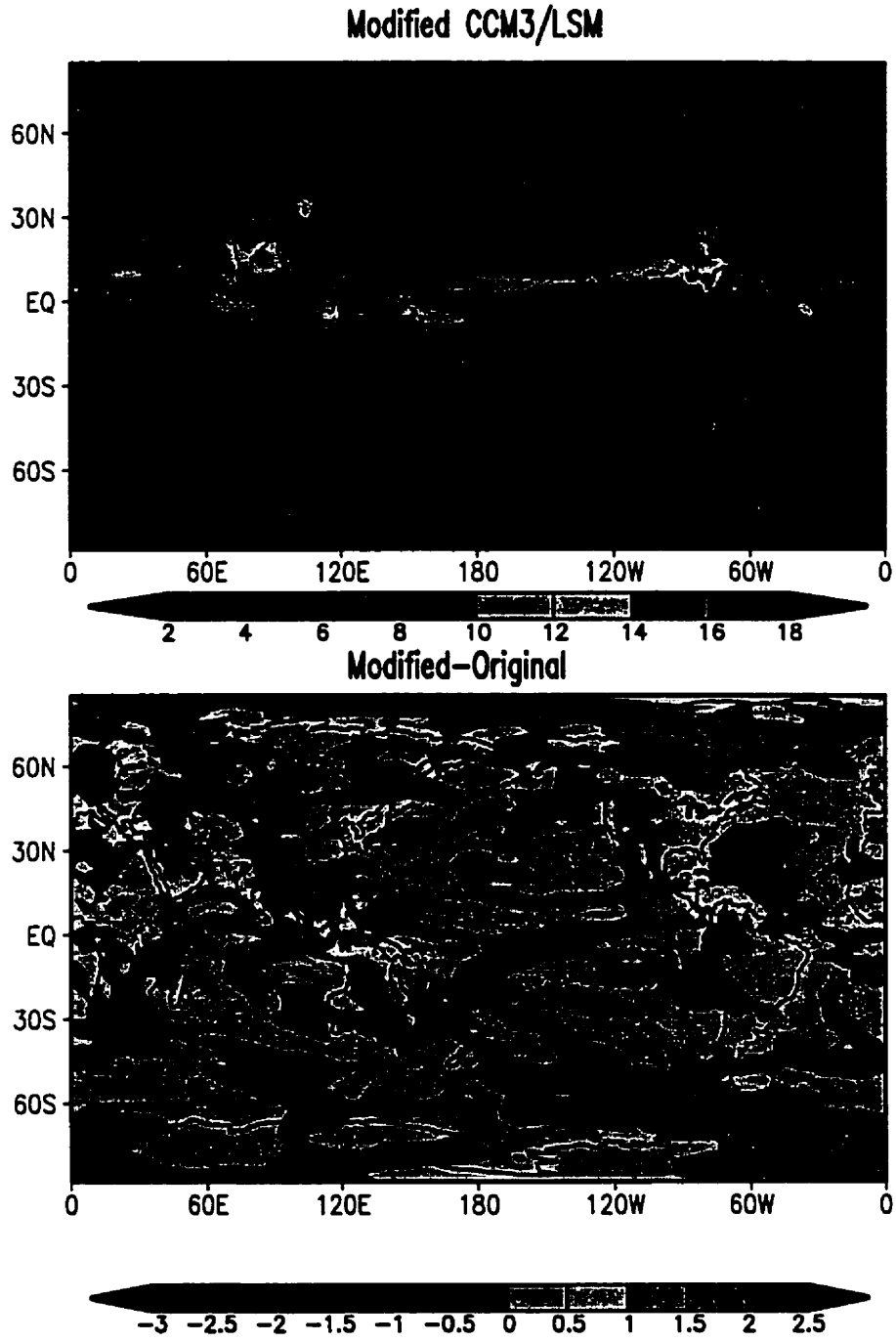

Figure 5.36: Global JJA distribution of precipitation rate (mm/day) for the modified model and the difference between the modified and the original models (lower panel).

the top panels of Figures 5.37 and 5.38 shows that the modified model can still reproduce the main features of this ENSO event as the original model does. This implies that the modification is physically consistent with other processes in the original model and, the modified model performs properly. The most obvious improvement by the modified model was found in the Indian Ocean. The original model gives a high there, while the modified model gives a low as in the observation.

5.2.8 Annual Hydrologic Cycle

Figure 5.39 shows the annual cycle of globally averaged precipitable water (representing the storage of water vapor in the atmosphere), precipitation, and the difference between the evaporation and precipitation, for CCM2/LSM, the original CCM3/LSM and the corresponding observational estimates (Hack et al. 1998). The estimates of precipitation rate are taken from Xie and Arkin (1996), who have constructed global distributions of monthly precipitation by combining data from gauge observations, several different satellite retrieval estimates and predictions from ECMWF operational forecast model. Observational estimates of precipitable water are taken from the NVAP, which combines water vapor retrievals from TIROS-N Operational Vertical Sounder (TOVS) and the Special Sensor Microwave/Imager (SSM/I) platforms with radiosonde observations (Randel et al. 1996).

The CCM3/LSM simulation is systematically drier than the NVAP estimates. In all cases, the global annual cycles shown in the first panel of Figure 5.39 are dominated by a stronger seasonal cycle in precipitable water over the Northern Hemisphere. The seasonal cycle in precipitable water is fueled by an imbalance in the globally averaged evaporation and precipitation, where the precipitation term exhibits a similar seasonal peak during the Northern Hemisphere summer months. The imbalance responsible for the annual cycle in precipitable water turns out to be very small, measured in fractions

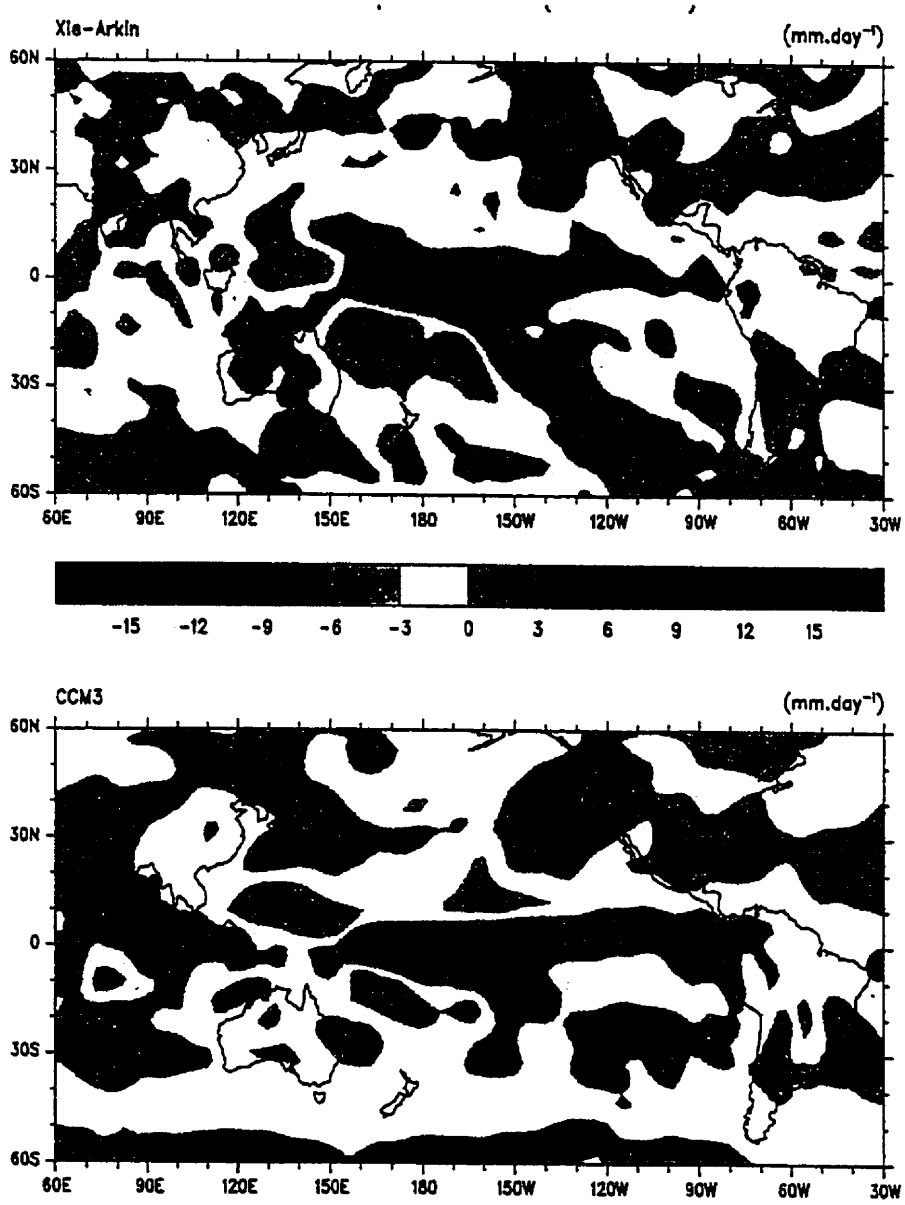

Figure 5.37: DJF87-DJF89 (warm-cold) precipitation rate anomalies (mm/day) for the Xie and Arkin (1996) precipitation climatology (top panel), and as simulated by the original CCM3/LSM. (Courtesy of Hack et al. 1998)

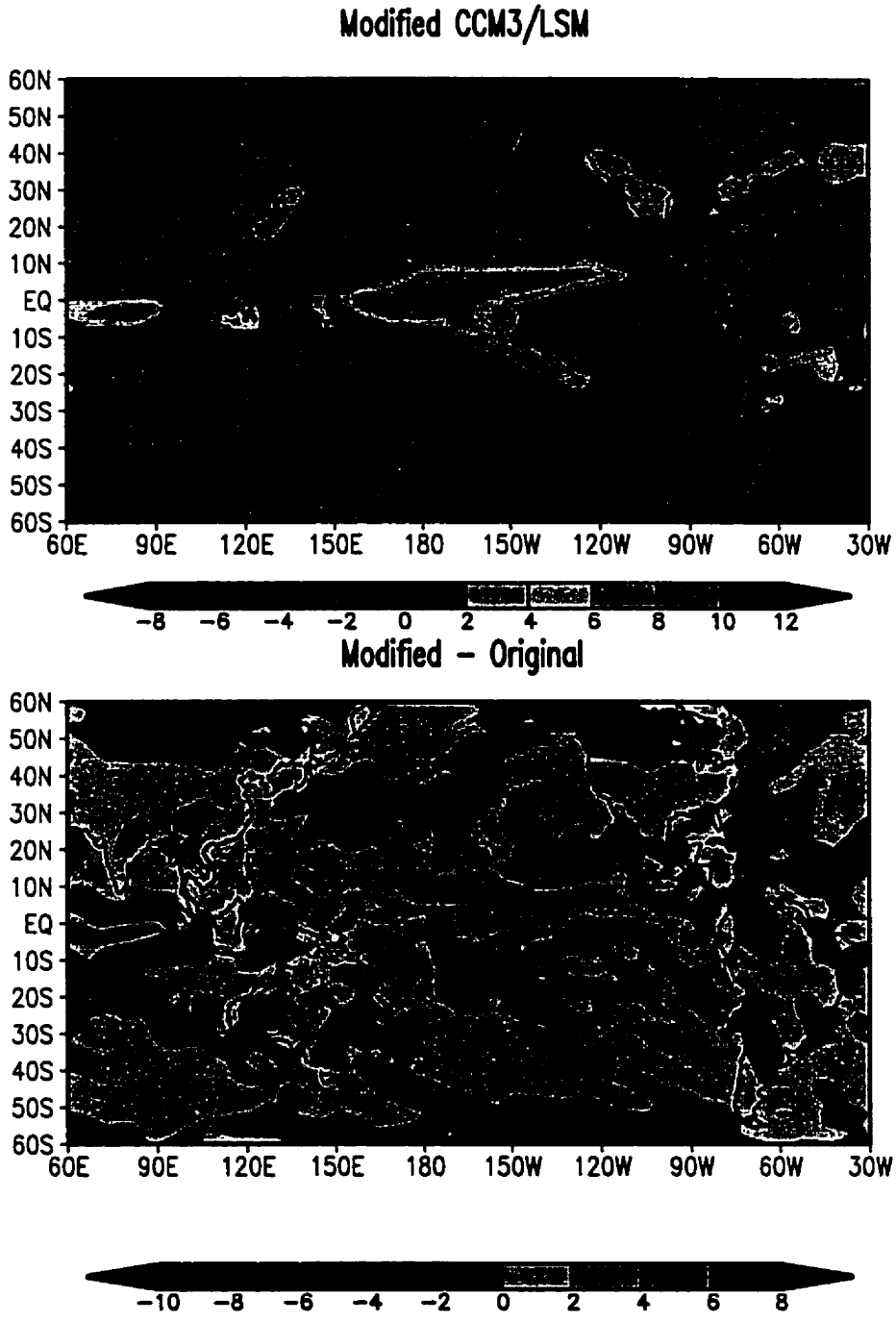

Figure 5.38: DJF87-DJF89 (warm-cold) precipitation rate anomalies (mm/day) for the modified model and the difference between the modified and the original models (lower panel).

of a watt per square meter, as shown in the third panel in Figure 5.39 (where the curve labeled OBS is derived from the NVAP and Xie and Arkin datasets).

The comparisons between the modified and the original model simulations of the annual cycles are shown in Figure 5.40. The annual cycles in this figure are very similar with those shown in Figure 5.39, with slight differences. For example, the maximum for the precipitable water for this study is in August and September, instead of July and August in Figure 5.39. The maximum of precipitation is in August for this period, instead of July in Figure 5.39, which was derived from a 15-year run (1979-1993). And consequently, the turning point from source of total water to sink of total water was located in August, instead of July in Figure 5.39. All these slight differences are most possibly due to the shorter sample length (8 years) from the new simulations than Hack's (15 years). However, shorter time simulation can reflect the climatology of that specific period, while longer time simulation can be used to derive more general climatology.

The first panel in Figure 5.40 shows strong annual cycle in the precipitable water with a maximum in August. The modified model slightly improved the original model between September and October, while it failed to improve the original model in other months. This is possibly due to the modification in the runoff parameterization is more effective when there is more surface water supplies during summer and fall. The annual cycle of precipitation rate (middle panel) has its maximum in July and August. While keeping the observed pattern from Xie and Arkin (1996), the modified model slightly improved the original model on the annual cycle simulation of precipitation through the whole year except October. Interestingly, Bonan (1998) himself compared his CCM3/LSM simulated precipitation with Legates and Willmott (1990), instead of Xie and Arkin (1996), which claims substantial differences from Legates and Willmott (1990). The patterns of precipitation and evaporation determined the pattern of the

net water exchange $E - P$ (third panel). The imbalance between evaporation and precipitation is a little bit larger than that presented in Hack's long time integration (Figure 5.39). And the pattern is very similar with that in Figure 5.39 with the turning point between water source and sink moved to August by the precipitation peak. However, the modified model again improved the $E-P$ annual cycle throughout the whole year.

5.3 Potential Impact on the Environment

The LSM simulates the exchange of CO_2 from plant growth (photosynthetic CO_2 uptake: maintenance and growth CO_2 loss) and CO_2 loss from microbial respiration (i.e. decomposition) (Bonan 1996b). This is a very complicated process related to many biochemical processes. In this short section, we are not going to discuss the detailed mechanism of the CO_2 flux in the model, instead, we just want to find out the changes in the net CO_2 flux between the land surface and the atmosphere the modification may introduced, compared with the original model result. Bonan (1998) and Craig et al. (1998) have concluded the efficiency and the importance of the inclusion of CO_2 flux into LSM coupled to AGCMs.

Note, only the net CO_2 exchange between the land surface and the atmosphere, not the atmospheric CO_2, will be discussed because we did not have the output of the atmospheric CO_2 from our AGCM. Craig et al. (1998) has addressed the impact of the net CO_2 exchange between the land surface and the atmosphere on the atmospheric CO_2 simulation. After finding out the changes the modification may introduced, compared with the original model result, we can try to figure out the potential impact of the modification on the atmospheric CO_2, and thus on the carbon cycle in our environment.

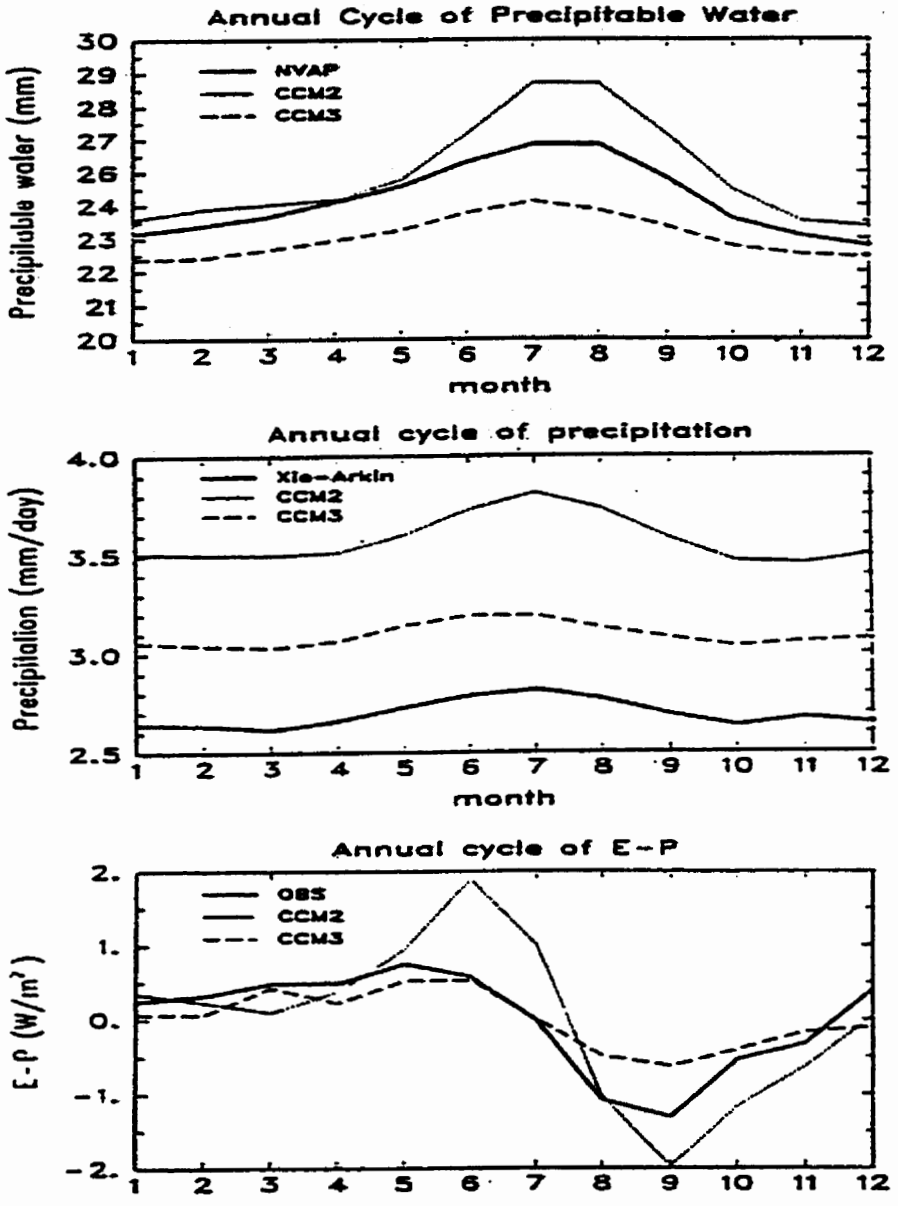

Figure 5.39: Annual cycle of globally averaged precipitable water (mm), precipitation rate (mm/day), and the difference between the evaporation and precipitation (E-P) (Wm^{-2}), for the original CCM3/LSM, CCM2/LSM, and corresponding observational estimates. (Courtesy of Hack et al. 1998)

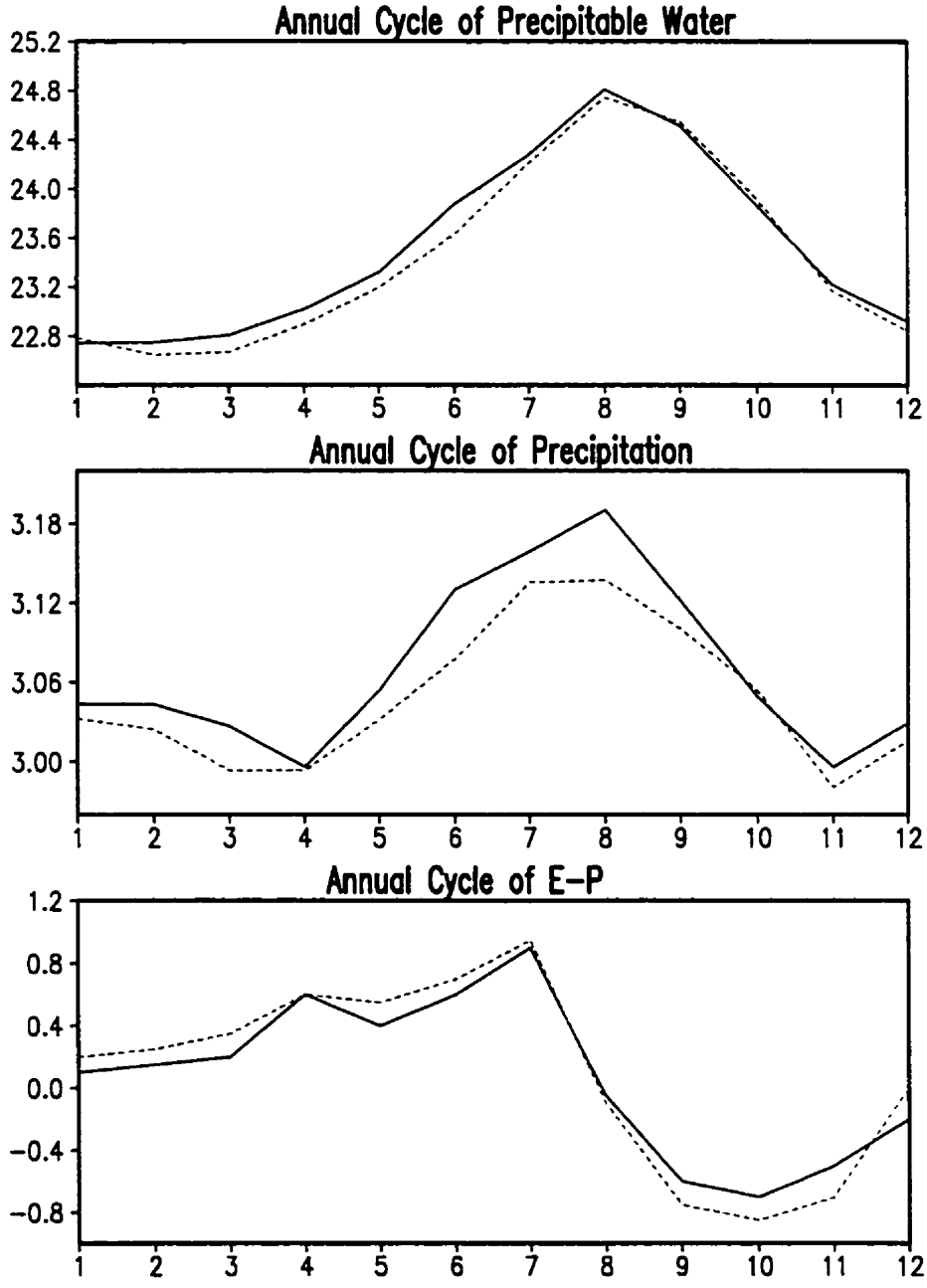

Figure 5.40: Annual cycle of globally averaged precipitable water (mm), precipitation rate (mm/day), and the difference between the evaporation and precipitation (E-P) (Wm^{-2}), the solid line is for the original CCM3/LSM and the dashed line is for the modified model.

Figure 5.41 shows the annual cycle (top panel) and the zonal- annually averages of net CO_2 flux($\mu molm^{-2}$) derived from the simulation for the period from January 1987 to January 1995, for the original (solid line) and the modified (dashed line) models. The inclusion of the topographic effects into the LSM generates more CO_2 flux into the atmosphere for the whole year cycle and on the whole globe, with the general patterns unchanged for either the annual cycle or the zonally annual average. The poleward zero values are due to the calculation of the CO_2 flux in the LSM is done only on land, not on ocean surfaces or frozen surfaces where no plants grow. This can be found in the seasonally averaged CO_2 flux horizontal distribution in Figure 5.42.

Plotted in Figure 5.42 is the difference of the simulated CO_2 flux between the original and the modified models. In the Northern Hemisphere winter (DJF), the modified model produces about 0.5 $\mu molm^{-2}$ more CO_2 flux than the original model in most regions. At the mean time, the modified model produced more CO_2 flux than the original model at some areas in Amazon basin, the top of the Andes Mountains (up to 3 $\mu molm^{-2}$), and some areas in the Central Africa (up to 2 $\mu molm^{-2}$); And it produced less CO_2 flux than the original model at the northeast of Australia (about 1 $\mu molm^{-2}$), the east coast of south Africa (by about 2 $\mu molm^{-2}$), and at the lee side of the Andes in South America (about 2.5 $\mu molm^{-2}$).

More significant changes can be found in the Northern Hemisphere summer (JJA) horizontal distribution (bottom panel in Figure 5.42). The modified model substantially reduced the CO_2 flux in the eastern U.S. by about 1.5 $\mu molm^{-2}$; at the downstream side of the Amazon and the lee side of the Andes by 1.5 $\mu molm^{-2}$; Other reduced areas (around 1 $\mu molm^{-2}$) can be found at the Mackenzie River basin in North America, Russia, around the Tibet Plateau, the Yellow River area, North Australia, and in Africa, etc. The most significant increase of the CO_2 flux given by the modified model is at the south foot of Himalayas and over the south portion of the

Rocky Mountains, by about 4 $\mu molm^{-2}$; Other increased areas are some areas in the upstream of the Amazon, and in the ALPS mountain areas in Europe.

In summary, compared with the original model result, the modified model produced more CO_2 flux over higher topographic areas, less CO_2 flux over lower topographic areas, when the modification on the runoff parameterization affects more on the model climate in corresponding hemisphere. And changes in the net CO_2 between the land surface and the atmosphere must have an impact on other lower boundary layer variables through very complicated biochemical mechanism (Bonan 1996b; Bonan 1998), and further have an impact on the atmospheric CO_2 distribution (Craig et al. 1998), thus must affect the carbon cycle in the global environment.

Craig et al. (1998) concluded that errors in temperature and precipitation simulations cause anomalies in the atmospheric CO_2 field. Our analysis on temperature and precipitation simulation in last section shows many very encouraging improvements in these two fields, i.e., the modified model reduces the errors in the temperature and precipitation simulations. Therefore, the modified model may improve the atmospheric CO_2 simulation. More work on atmospheric CO_2 simulation is needed to verify this point.

5.4 Significance Check on the Modification

Many improvements have been claimed in previous sections. To further confirm these improvements, in this section, we are going to do some significance tests on some typical variables first. To get a comprehensive explanation, the impact of the modification on the basic atmospheric waves will be examined in the second subsection.

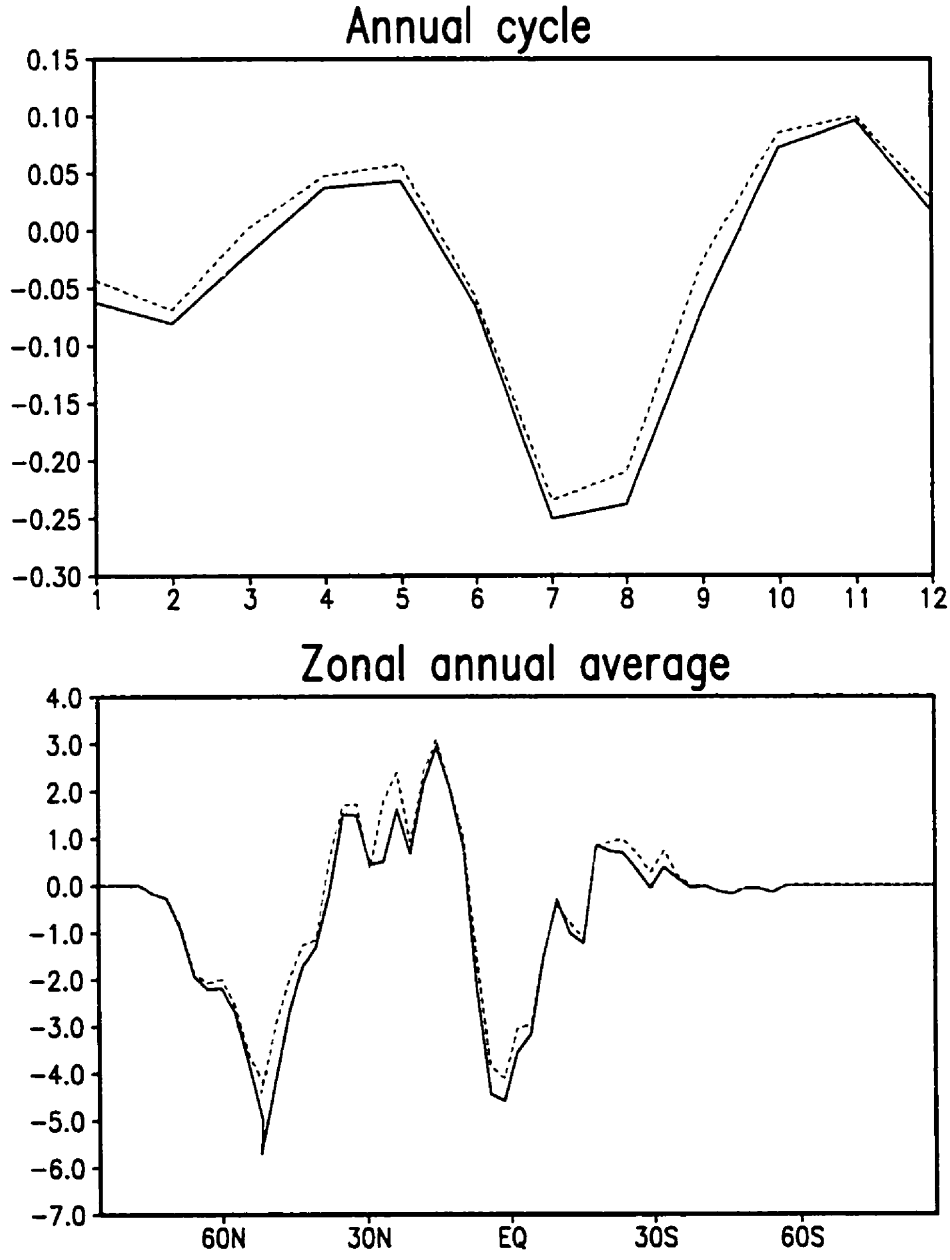

Figure 5.41: The annual cycle (top panel) and the zonally annual average of CO_2 flux($\mu molm^{-2}$) derived from the simulation from January 1987 to January 1990, for the original (solid line) and the modified (dashed line) models.

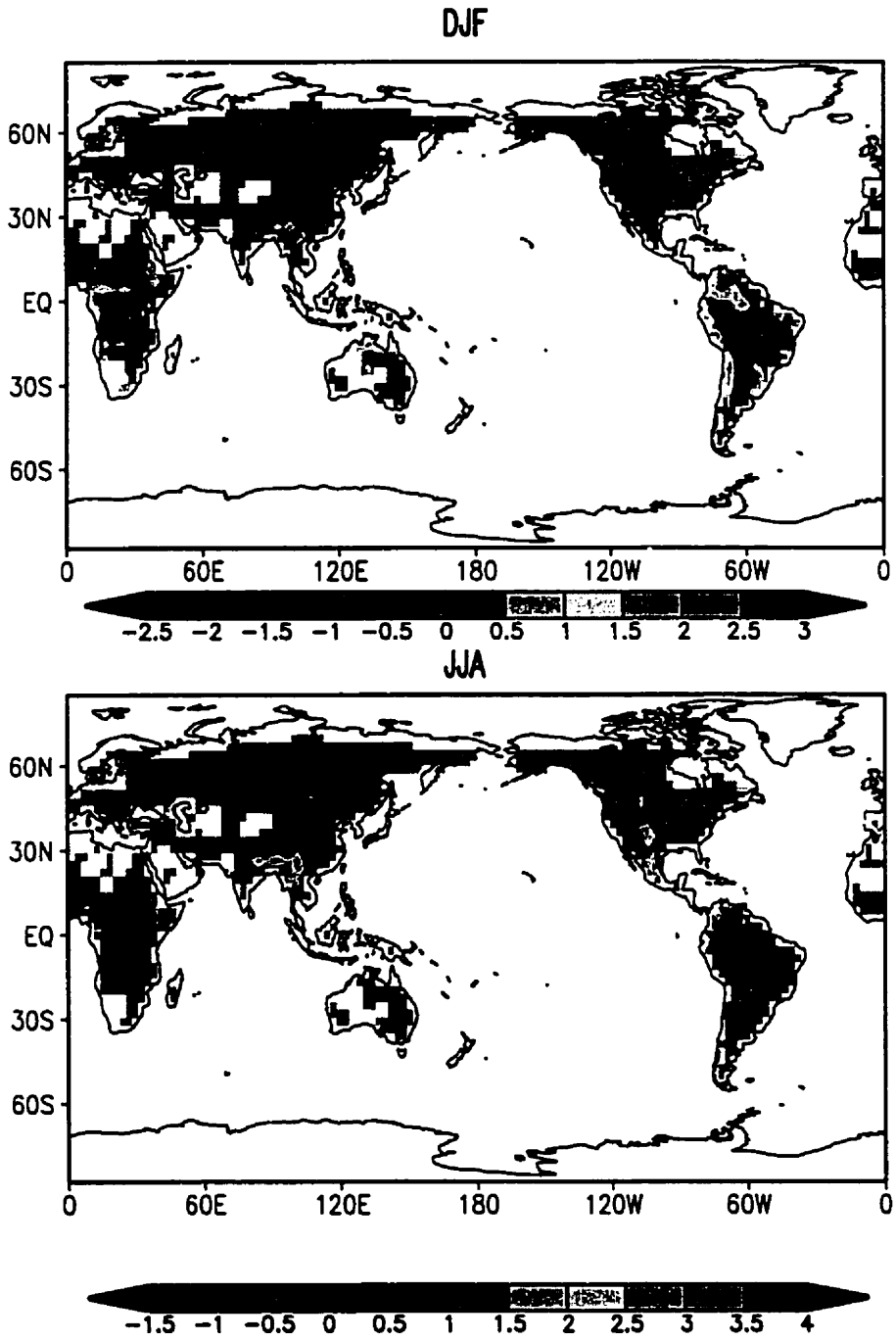

Figure 5.42: Global distribution of net CO_2 flux($\mu molm^{-2}$) for DJF (top panel) and JJA. Plotted is the difference of the simulated net CO_2 flux between the original and the modified models, i.e., $MODEL_{modified} - MODEL_{original}$.

5.4.1 T-test on Surface Fields

The Student's t-statistic was used to identify significant changes between the modified and the original model results. The advantage of using the t-statistic is that all areas and times are standardized with respect to each other by consideration of the variance (Karl and Riebsame 1984).

Chervin and Schneider (1976) used the next quantity to determine the statistical significance of climate experiments with AGCMs.

$$t = \frac{\bar{y} - \bar{x}}{s(\frac{1}{n} + \frac{1}{m})^{\frac{1}{2}}} \tag{5.1}$$

where x and y are two samples with length of m and n respectively; $\bar{x}$ and $\bar{y}$ are averages of x and y respectively; and s is defined as following

$$s^2 = \frac{\sum_{i=1}^{m}(x - \bar{x})^2 + \sum_{i=1}^{n}(y - \bar{y})^2}{m + n - 2}$$

In this thesis, x is the original model result and y is the modified model result. They have the same sample length in this study, which is 8 (years for annual averages or seasons for seasonal averages). With this sample length, areas with $|t|$ values over 1.345 have significance levels over 80%. Positive values means the modified model increased the variable and negative values means the modified model decreased the variable.

Again, we will begin the significance check with total runoff; the most modification related field, then surface temperature and surface pressure. After this, we will check the t-test scores for the vertical cross sections of atmospheric temperature and specific humidity corresponding with Figures 5.18 and 5.20.

T-test scores of total runoff are plotted in Figure 5.43. Shaded areas are those with over 80% significance level. Significant changes can be found at most big topography vicinities. Generally, the total runoff is reduced at higher topography sites (along

mountain bodies), and increased at the lower topography sites (along mountain feet). This mechanism is most clearly demonstrated at the Andes Mountains vicinities, most probably due to its dimensional simplicity compared with other regions over the world (e.g., the Rocky Mountains and Tibet Plateau, etc.). This mechanism is also most clearly shown up in this area in the surface temperature analysis (Figures 5.44, 5.45, and 5.46). That is why we chose this area for the point budgets analysis in section 5.2.2.

Presented in Figure 5.44 are the t-test scores on the annual averaged surface temperature and surface pressure. Areas with significance levels over 80% are shaded. And contours between -1 and 1 are not plotted. From the upper panel of Figure 5.44, the most significant changes are found at the vicinities of the Andes Mountains in South America, showing a heating (over mountains) and cooling (lee side of the mountains) dipole. Relatively significant changes can also be found in the Tibet Plateau vicinities, most areas of Africa, Russia and Mexico, Australia and over the central Antarctic. T-test scores for the annual averaged surface pressure reveal several areas with significant rises, for example at the central Pacific, north-west of Europe; and four areas with significantly lowered surface pressure, the west coastal area of South America, east Atlantic ocean and North Africa, the Central and Southern United States, and over the North Pacific ocean and the Central Arctic Ocean. No significant changes are found at the north portion of the Rocky Mountains vicinities in this annual time scale analysis. That is why we did not see much difference in Figure 5.16 in last section. This is possibly due to the less precipitation (at the north portion of Rockies), which is directly related to the modification.

In the JJA t-test scores of the seasonal averaged surface temperature and surface pressure (Figure 5.45), more significant changes are found generally at similar locations as in the annual analysis. The highest score for surface temperature changes

from 6 to 10 (over the Tibet Plateau). And the areas with significant changes are larger than in the annual analysis, especially for the surface pressure. Significant changes of surface temperature show up along the whole Rocky Mountains at this seasonal time scale. The surface pressure is significantly lowered across the Central Africa, at the downstream side of the Rocky Mountains throughout to the east coast in North America, and over the ocean to the west of South America. Surface pressure significantly rises over the Central and Eastern Europe, over the Pacific Ocean and over the Bellingshausen Sea area between the South America and the Antarctic.

Compared with the DJF t-test scores of the seasonal averaged surface temperature and surface pressure (Figure 5.46) and the annual t-test scores (Figure 5.44), the modification brought the most significant changes to both the surface temperature and the surface pressure in the Northern Hemisphere summer. This is understandable because the runoff parameterization is mainly based on precipitation. So, the modification is very sensitive to precipitation, the more precipitation, the more impact the modification will cause to the model climate.

From the t-test for the surface pressure, one will easily raise a question: the modification made to the model is on land, why has the surface pressure changed over the ocean? This reminds us to check whether the modification also changed the basic atmospheric structure. The following subsection will answer this question.

5.4.2 T-test on Atmospheric Temperature and Humidity

Recalling Figures 5.18 and 5.20, one can remember that we claimed some small numbers as significant changes in atmospheric temperature and specific humidity. Are they really significant? Corresponding t-test scores for these two graphs are plotted in Figures 5.47 and 5.48. Again, the most significant changes are found in summer, which is consistent with all of the previous analysis. The 0.2K correction on the warm

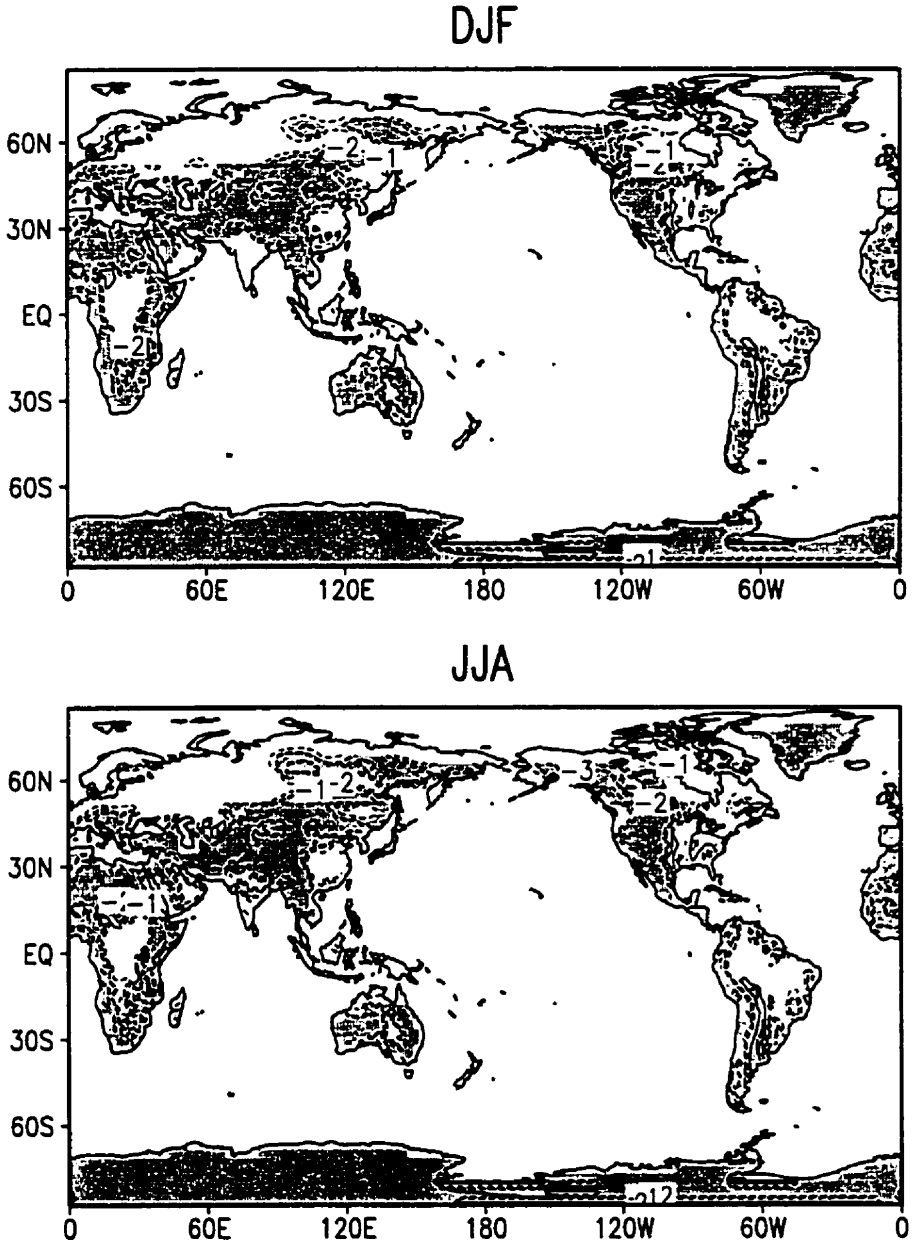

Figure 5.43: T-Test scores on the seasonal averaged total runoff. Areas with significance levels over 80% are shaded. Positive areas represent the modified model result is larger than the original result.

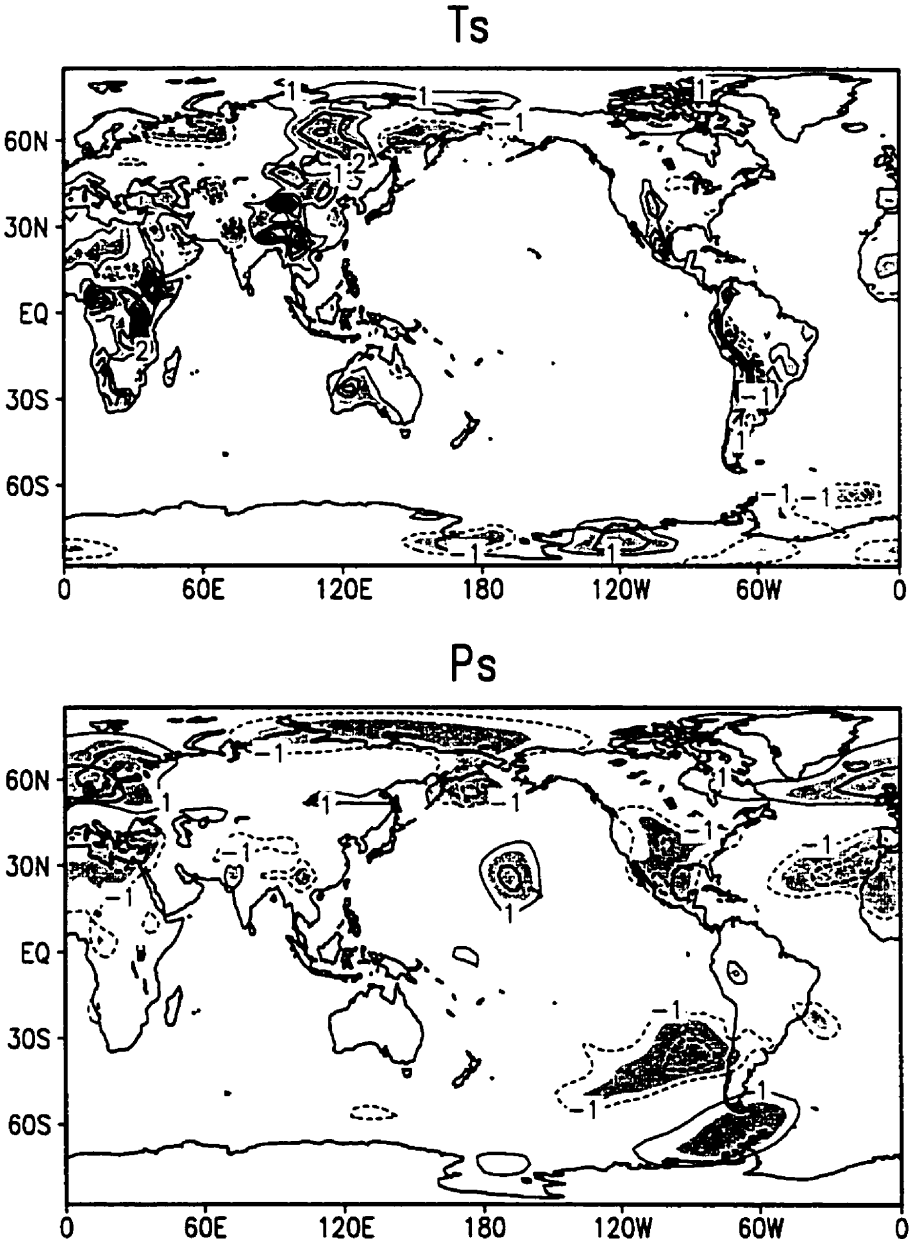

Figure 5.44: T-Test scores on the annual averaged surface temperature (T_s) and surface pressure (P_s). Areas with significance levels over 80% are shaded. Positive areas represent the modified model result is larger than the original result.

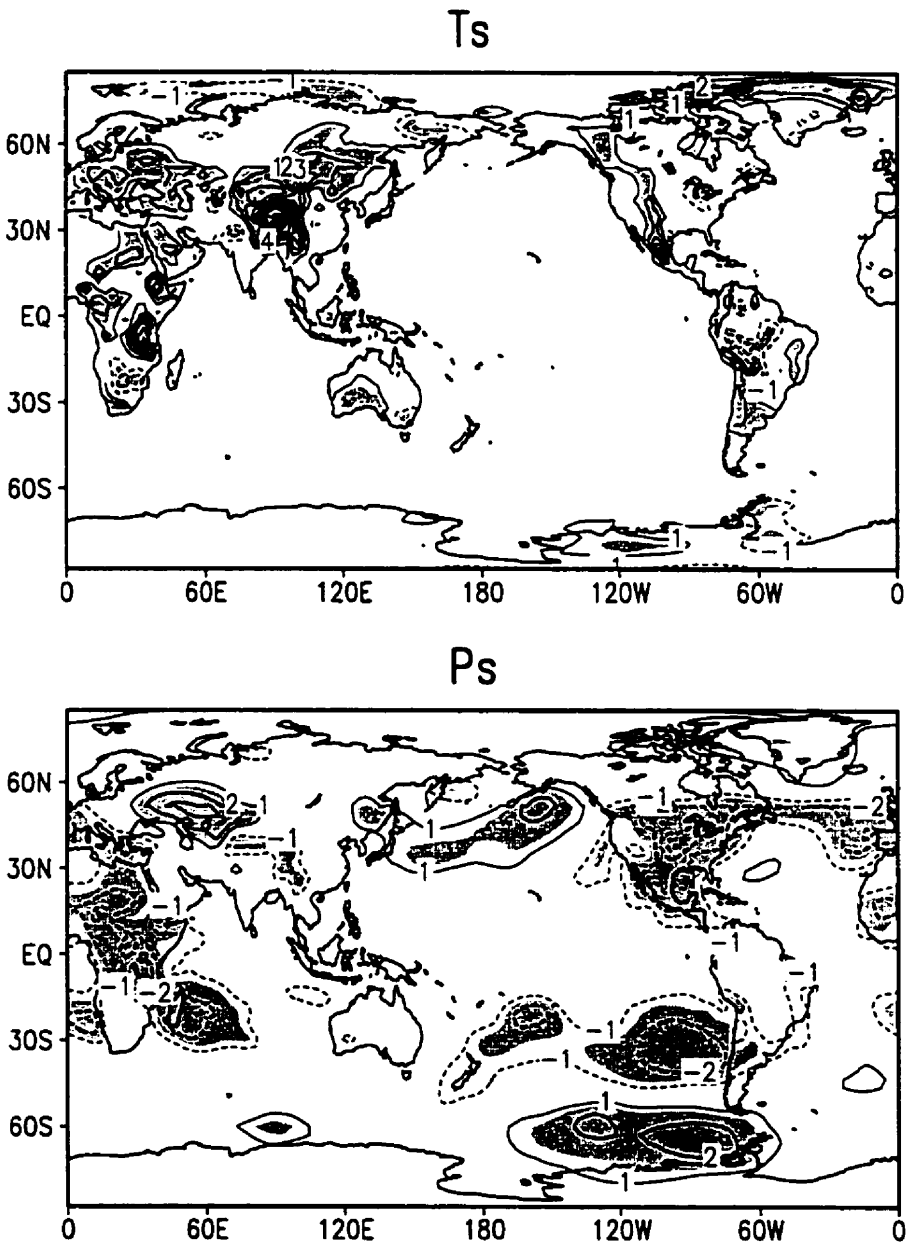

Figure 5.45: T-Test scores on the seasonal (JJA) averaged surface temperature (T_s) and surface pressure (P_s). Areas with significance levels over 80% are shaded. Positive areas represent the modified model result is larger than the original result.

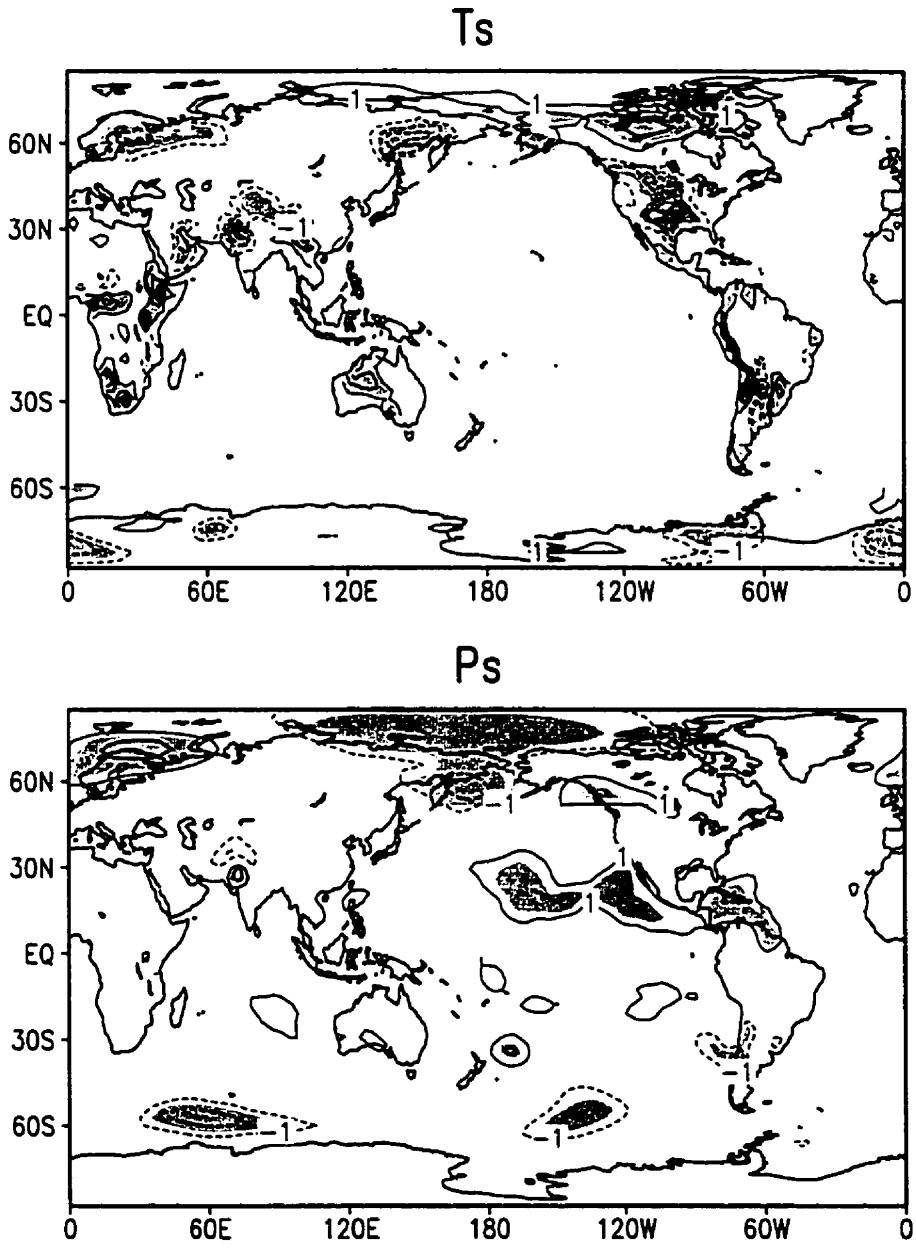

Figure 5.46: T-Test scores on the seasonal (DJF) averaged surface temperature (T_s) and surface pressure (P_s). Areas with significance levels over 80% are shaded. Positive areas represent the modified model result is larger than the original result.

bias at the middle tropical troposphere in DJF in Figure 5.18 is not small, it is with an over 80% significance level. The 1.2K correction at the lower polar troposphere for DJF is also at 80% significance level. The most significant changes in the summer atmospheric temperature are found at the middle troposphere at the north polar region, with a high t-test score of over 3.0. The warm-up at the 30S is also a significant change. The 0.6K correction of the cold troposphere temperature simulation is indeed at an over 80% significance level.

Corresponding with the most significant changes in the summer atmospheric temperature are the most significant changes in atmospheric specific humidity at the same region (Figure 5.48). This significant change in atmospheric moisture the modified model generated is most probably due to the simple treatment of the surface processes in the polar region in the original model. The increased moisture could cause more latent heat release in the air column and thus increase the atmospheric temperature in the air column (shown in Figure 5.47) and, consequently, improves the model simulations of these basic atmospheric variables in this region. This implies that the modification makes the LSM more realistic and forces the AGCM to generate a more realistic climate.

Besides the most significant changes in the north polar region, the correction of the moist bias at the lower tropical troposphere and the correction between 30S and 60S are also significant. The deficiency over 30N in the moisture is also reported to be significant. As mentioned in last section, this problem is most probably rooted in the AGCM. No significant changes in specific humidity are found for the DJF season, mainly due to the fact that the ground surfaces are frozen during winter.

To explain the significant changes over the ocean brought by the modification made over land, we have proved that the basic atmospheric structure was changed by presenting the significant changes in the atmospheric temperature and specific

humidity. In next subsection we are going to further this discussion by describing the significant changes the modification brought to basic atmospheric waves and general atmospheric circulations.

5.4.3 Impact on the Atmospheric Waves

In this subsection, we are going to identify the changes in the basic atmospheric waves brought by the modification by extracting the single harmonic waves from 500hPa and 850hPa geopotential heights, using fast Fourier transform (FFT) (Press et al 1996).

The power spectrum is a very useful quantity to examine the changes in the atmospheric waves. Plotted in Figures 5.49, 5.50, and 5.51 are the power spectra for the first ten waves along the 45N latitude, extracted from the 500hPa and 850hPa geopotential heights, for the annual average, JJA average and DJF average, respectively. The 45N latitude represent middle latitude in Northern Hemisphere, where the dominant wave at the 500hPa level is Rossby wave which is the most important wave in this area. Another reason to analyze this area is that this area is a reasonable mixture of land (with moderate complex topography) and ocean than in other areas; To identify the relative significance of the changes between the high level (500hPa) and low level (850hPa, closer to the land surface), power spectra on 850hPa is also plotted. Only the first ten waves are plotted in these graphs because the waves after the tenth show little changes by the modification.

Going through Figures 5.49,5.50 and 5.51, one can easily find that the modification only changed the first 6 waves, with the most significant changes at the first wave followed by the second wave. Waves after the sixth show nearly no changes. On 500hPa (upper panels), the modification reduced the power of the first wave most significantly in the DJF season (over 100), less in the annual and seasonal averages

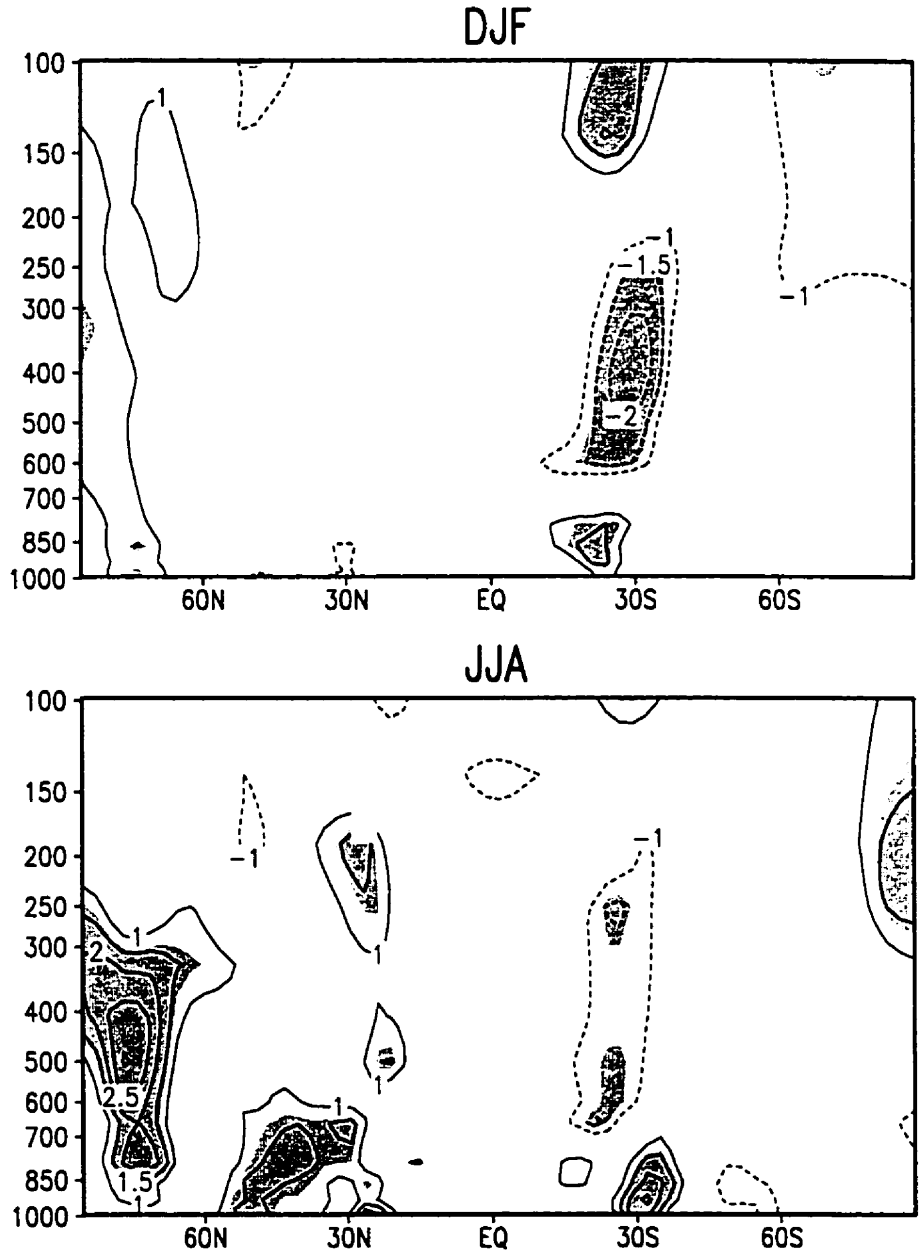

Figure 5.47: T-Test scores on the seasonal averaged atmospheric temperature corresponding with Figure 5.18. Areas with significance levels over 80% are shaded. Positive areas represent the modified model result is larger than the original result.

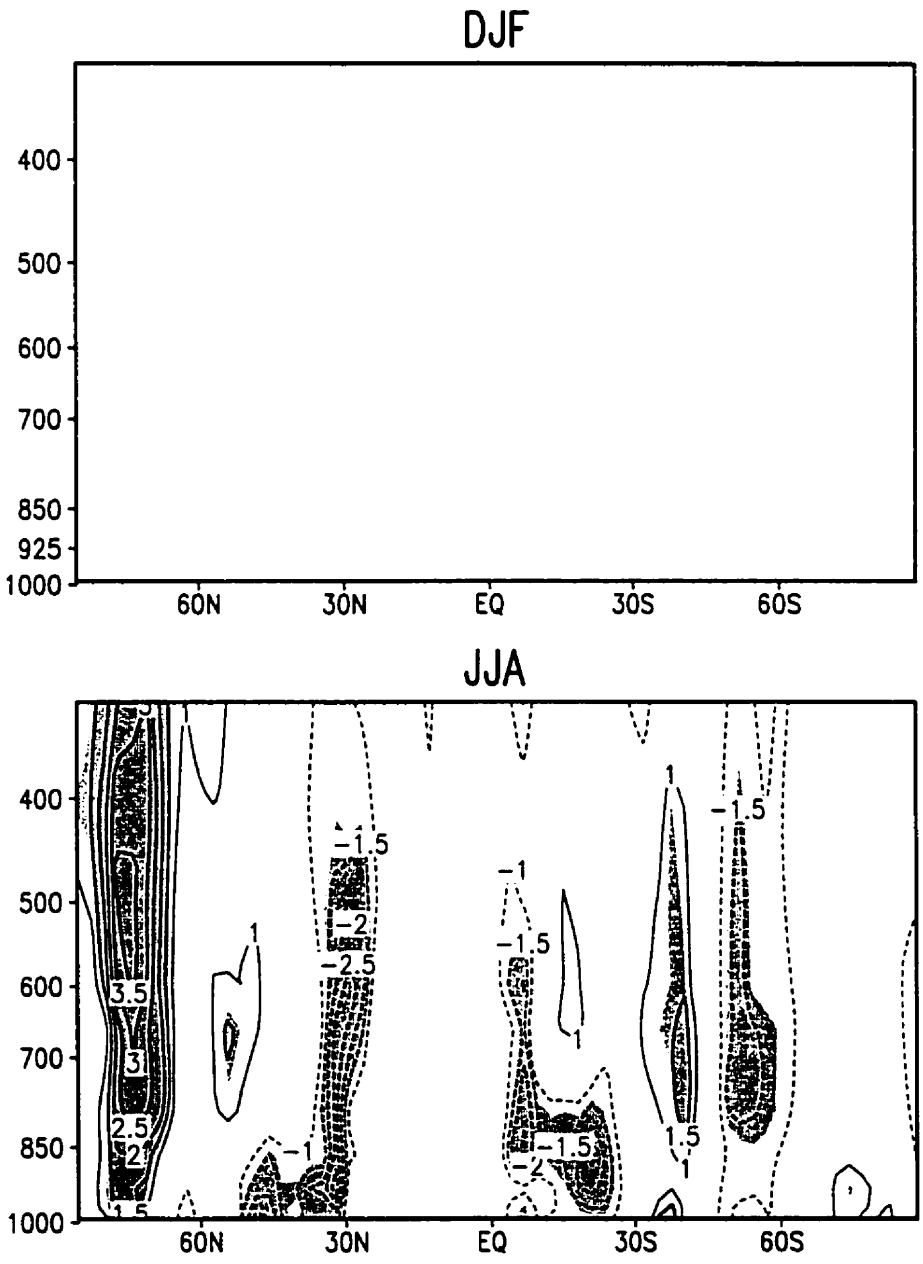

Figure 5.48: T-Test scores on the seasonal averaged atmospheric humidity corresponding with Figure 5.20. Areas with significance levels over 80% are shaded. Positive areas represent the modified model result is larger than the original result.

(around 20). For the second wave, the modification also reduced its power in the annual and JJA averages, while increased its power in the DJF average. On 850hPa, the power reduction on the first wave has the maximum in the DJF average (about 40), less in the JJA average (about 15), and the least in the annual average (just 2.5). The power of the second wave is increased by the modification, with the maximum increase in the JJA average (about 15), less in the DJF average (10) and the least (minor) in the annual average (about 2.5). Comprehensive comparison between 500hPa and 850hPa, the modification brought more significant changes on the Rossby waves on 500hPa than on the waves at 850hPa.

What exact changes has the modification brought to each wave? Plotted in Figure 5.52 are the first six waves extracted from the JJA average of the 500hPa geopotential height along the 45N latitude. These waves are those shown in Figure 5.50. The most significant changes are found in the first two waves, less significant changes in the third wave, and very slight changes in the fourth, the fifth and the sixth waves. This can be furthermore convinced by the corresponding t-test scores on these changes (Figure 5.53). Again, shaded areas are those with significance levels over 80%. More clearly, only the first three wave was significantly changed by the modification on 500hPa, while on 850hPa, significant changes can also be found in the sixth wave, with no significant changes in the fourth and the fifth waves.

Significant changes in these atmospheric waves must show up in the basic atmospheric circulations. For example, the Hadley circulation is mainly Rossby-wave-related, the significant changes mentioned above should have signs in the Hadley cell. Figure 5.54 and 5.55 will verify this point. Plotted in Figure 5.54 and 5.55 are the zonally averaged vertical velocity (ω) for DJF and JJA respectively. More significant changes were found in the Northern Hemisphere winter (Figure 5.54) than in the Southern Hemisphere winter. This is possibly due to the much less and much

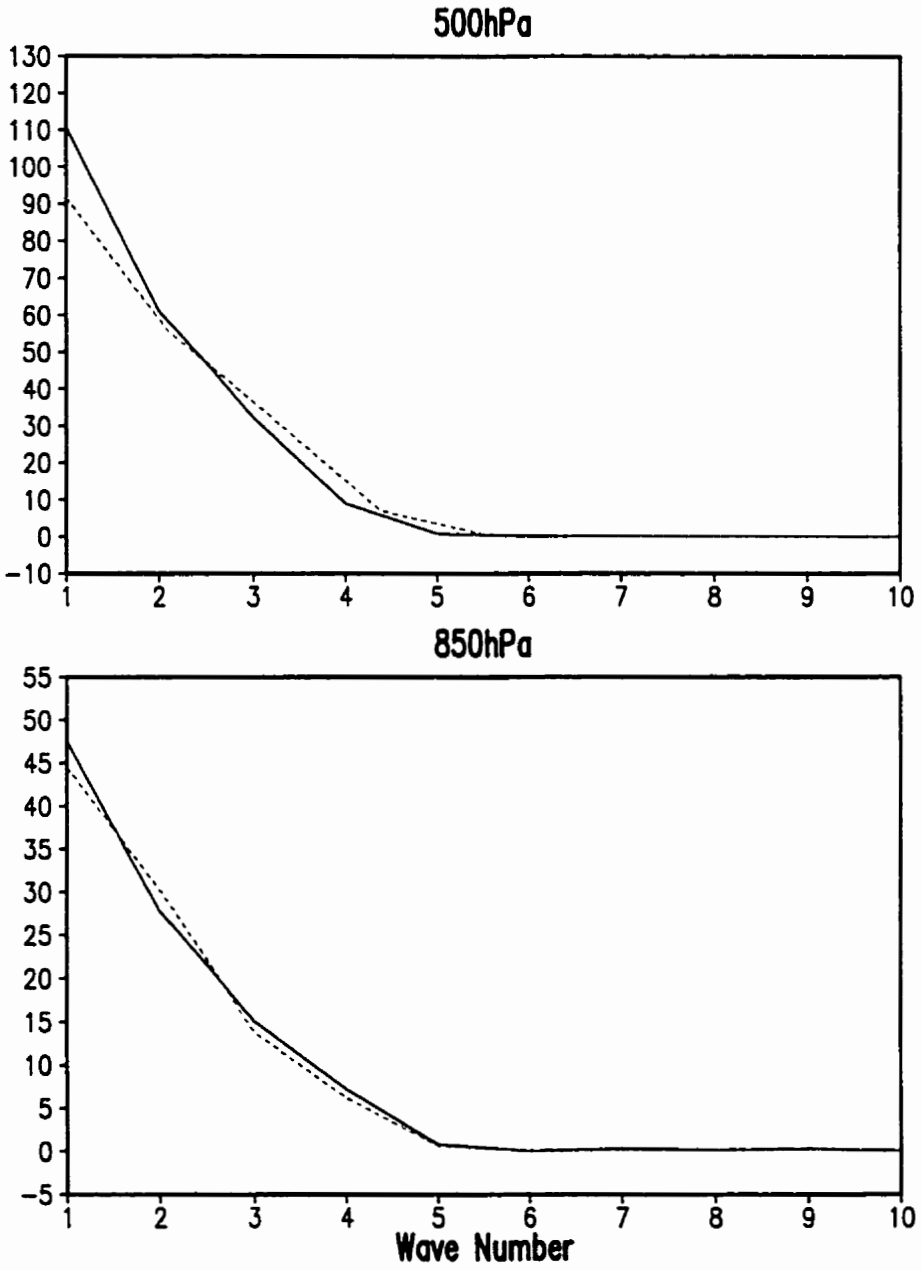

Figure 5.49: Power spectra (m^2) for the first ten waves along the 45N latitude, extracted from the annual averaged 500hPa and 850hPa geopotential heights. Solid line is for the original model and the dashed line is for the modified model.

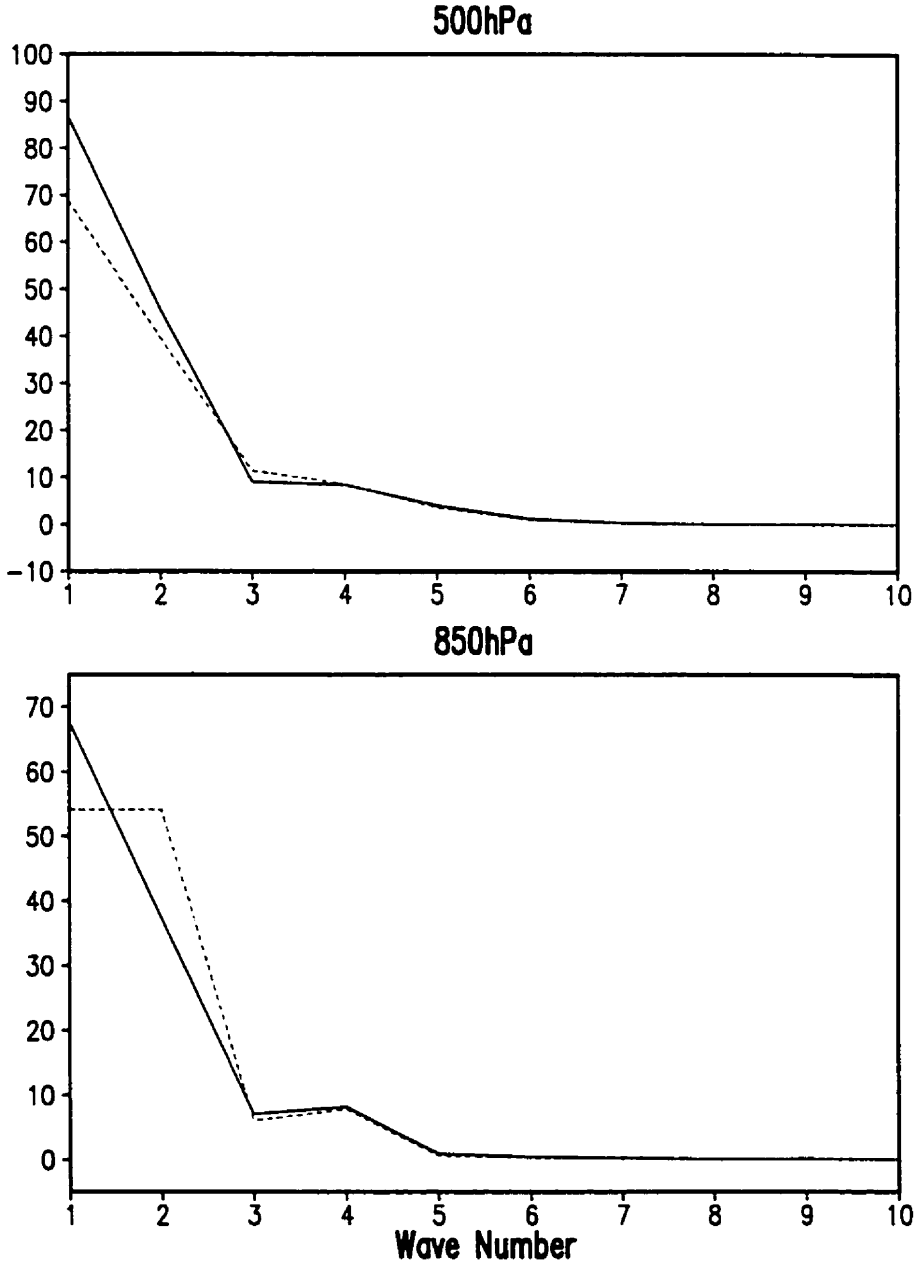

Figure 5.50: Power spectra (m^2) for the first ten waves along the 45N latitude, extracted from the seasonal (JJA) averaged 500hPa and 850hPa geopotential heights. Solid line is for the original model and the dashed line is for the modified model.

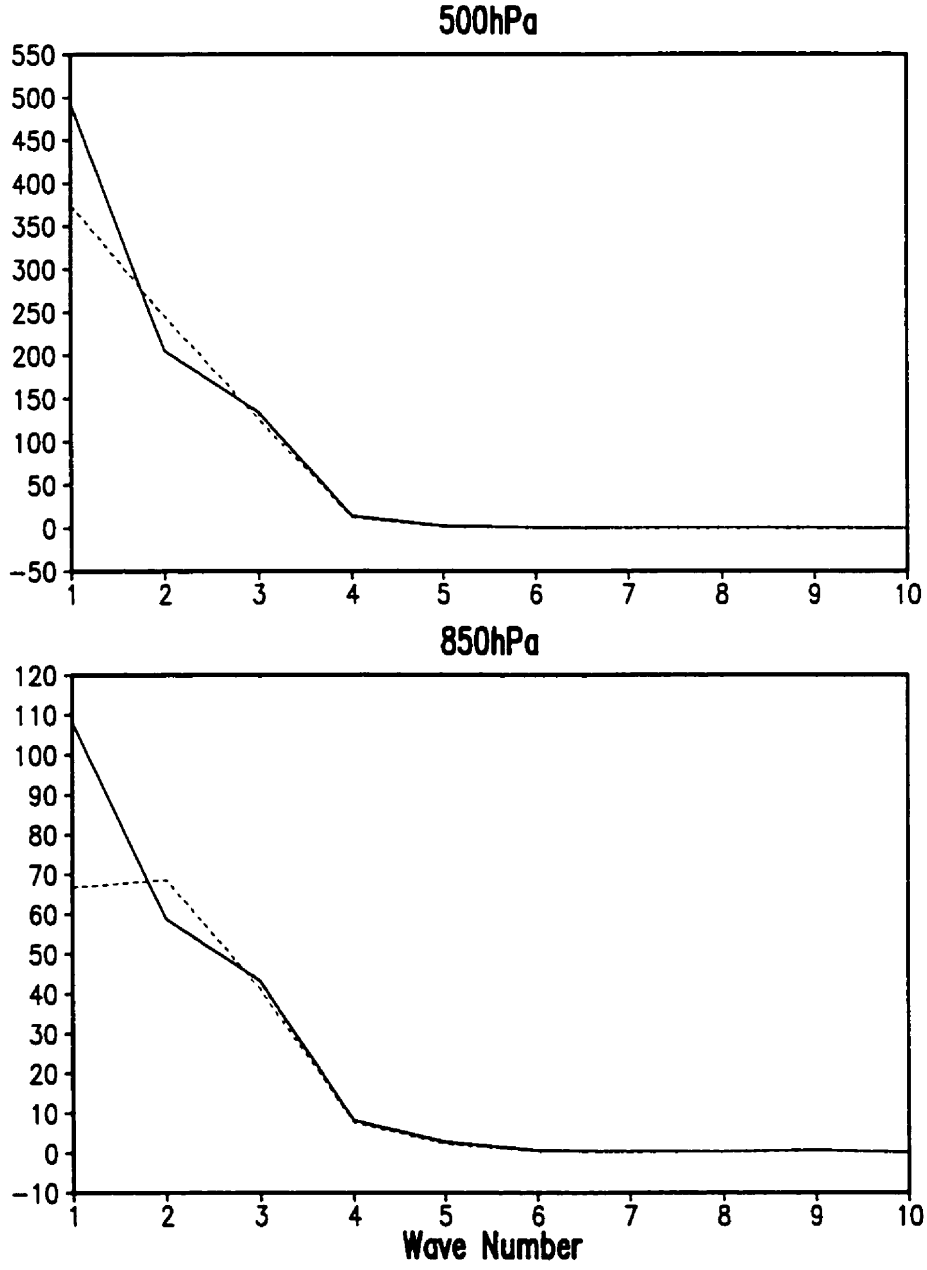

Figure 5.51: Power spectra (m^2) for the first ten waves along the 45N latitude, extracted from the seasonal (DJF) averaged 500hPa and 850hPa geopotential heights. Solid line is for the original model and the dashed line is for the modified model.

simpler topography in the Southern Hemisphere than in the Northern Hemisphere. Therefore, the modification on LSM brought less impact to the Southern Hemisphere than the Northern Hemisphere. The modification intensified the Hadley cell in the Northern Hemisphere winter by increasing both the upward and downward velocity over 0.05 hPa/s. Very slight changes can be found in the Hadley cell in the Southern Hemisphere winter (Figure 5.55).

The intensification of the Hadley cell could be explained by the mechanism of Hadley circulation. The modification results in drier surface at higher topography and wetter surface at lower topography. Drier surface has smaller heat capacity than wetter surface. Consequently, drier surface is easier to be cooled down in winter. The overall result of the modification in the Northern Hemisphere could be a cooler land, while the modification almost does not affect the temperature in the equator area. This will increase the temperature gradient between the equator area and the middle latitude, and thus intensified the Hadley cell.

Another important circulation is the Walker circulation, which is mainly Kelvin-wave-related. Comparison between the modified and the original model results show little difference on the Walker cell (not shown). This is mainly due to the fact that the Walker Circulation is a circulation in the equator area, where there is much less and much simpler topography than where the Hadley Circulation occurs. Therefore, modification on LSM should not cause much impact on Walker cell.

5.4.4 Summary

The modification brought significant changes to the surface temperature, especially in the vicinities of big topography (the Andes, and the Tibet Plateau, for example). Generally, the modification generates warmer surfaces at higher topography and cooler

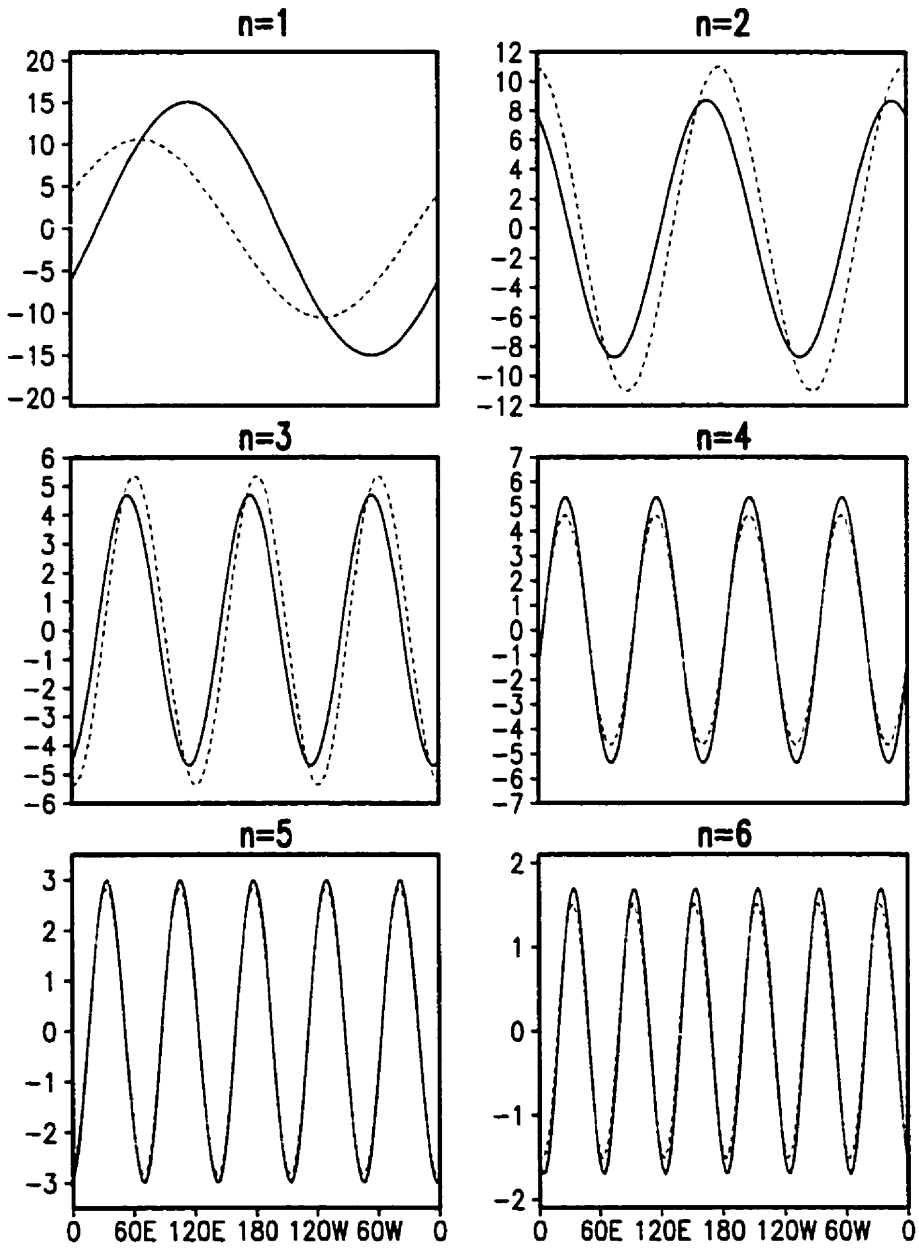

Figure 5.52: The first 6 waves along 45N on 500 hPa extracted from the seasonal (JJA) averaged 500hPa geopotential height. Solid lines are for the original model and dashed lines are for the modified model. The unit of amplitude is m.

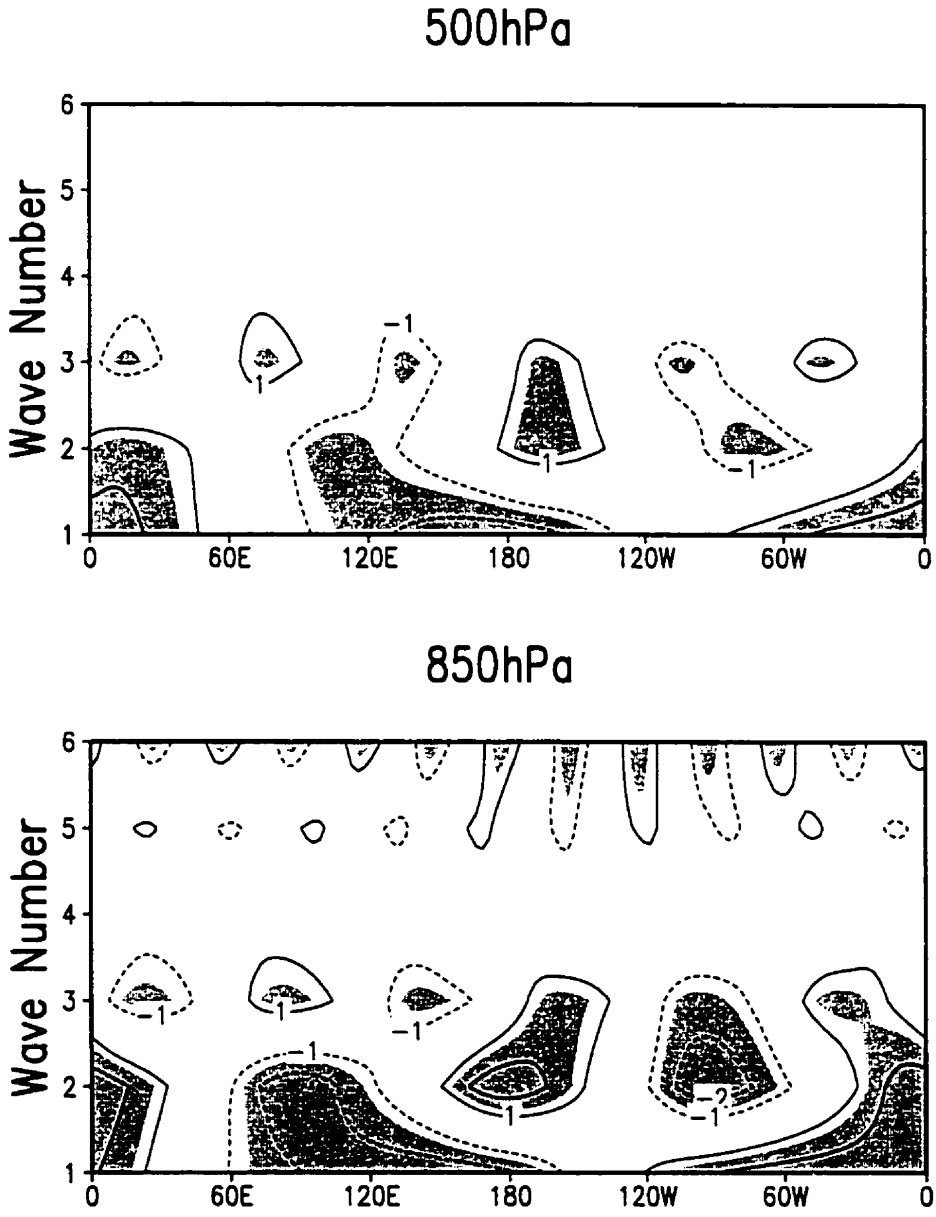

Figure 5.53: T-Test scores for the first 6 waves along 45N extracted from the seasonal (JJA) averaged 500hPa and 850hPa geopotential heights. Shaded areas are those with significance levels over 80%.

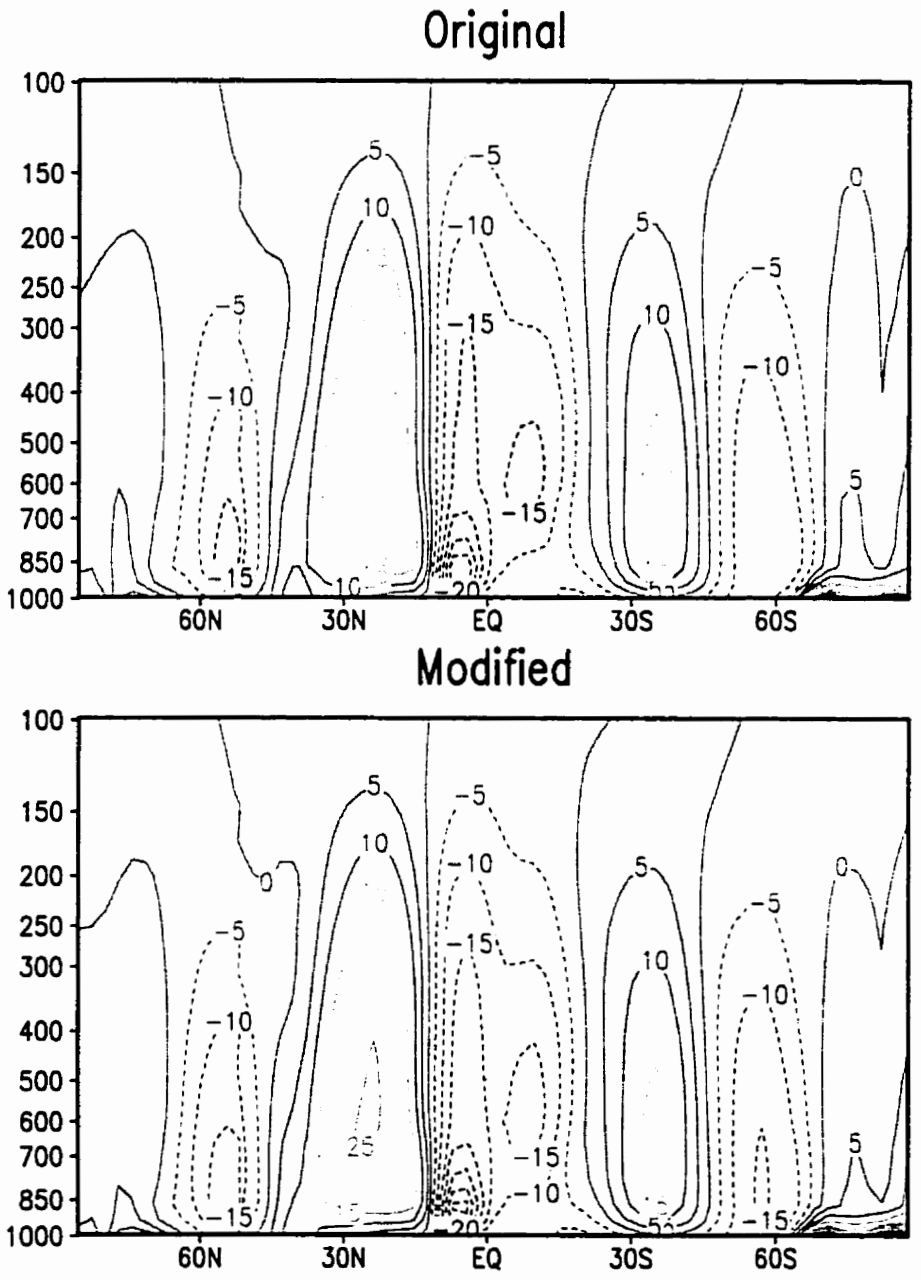

Figure 5.54: Comaprison of the simulated Hadley cells represented by the zonally seasonal (DJF) averaged vertical velocity (Pa/s). The upper panel is for the original model and the lower panel is for the modified model.

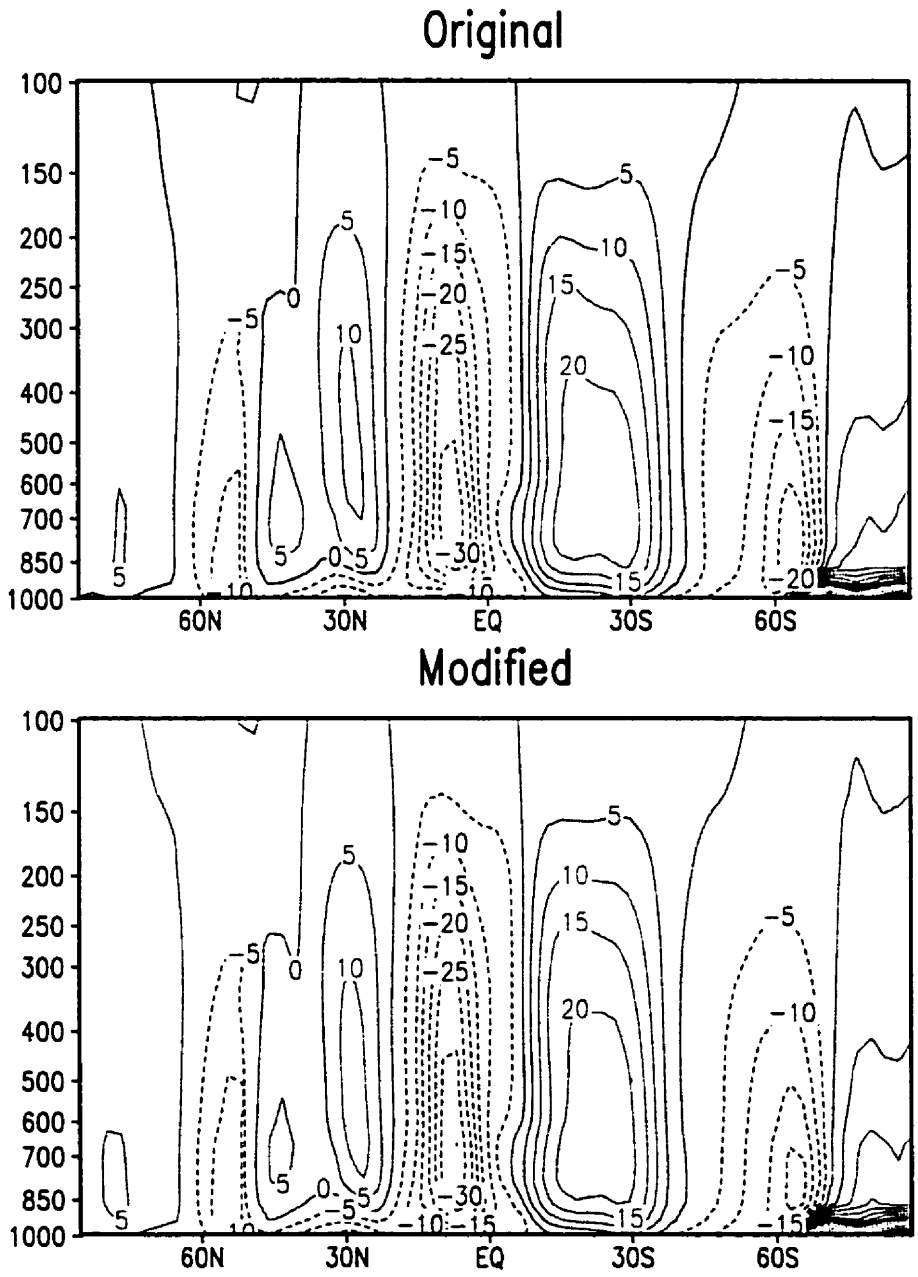

Figure 5.55: Comaprison of the simulated Hadley cells represented by the zonally seasonal (JJA) averaged vertical velocity (Pa/s). The upper panel is for the original model and the lower panel is for the modified model.

surfaces at the feet of the high topography, because the modification makes the surface drier at high topography and wetter at its feet. Changes of the surface moisture and temperature also caused significant changes in the atmospheric humidity at the upper atmosphere, which quite possibly changed the latent heating from condensation and consequently, changed the atmospheric temperature. Even more, these changes resulted in significant changes of the Rossby waves at the middle latitude. Significant changes are also found for the mainly Rossby-wave-related Hadley circulation. It is the significant changes in the basic atmospheric structure that extend the impact of the LSM modification from land to regions other than land.

Explanations to the impact the Hadley cell, and to the chain reaction to the modification from the surface variables to the upper Rossby waves given above are qualitative. Analytical explanations could be very difficult, especially for the impact of the modification on the Rossby waves. Many previous researches are on response of the equatorial Kelvin waves to simple forcing using very simple models (for example, Gill 1980; Gill 1982b; Horinouchi and Yoden 1996; Wang 1988; Wang and Rui 1990; Wang and Xie 1996; Webster 1972; Xie and Wang 1996). Similar work as Gill (1982b) and Clarke and Liu (1993) could be possible to get an analytical solution to the question raised here about middle latitude Rossby waves, but that could be another great thesis which needs a lot of work. Here I would like to end this subsection using Gill's words in his 1982 paper's summary (Gill 1982b), showing the complicated chain interaction in the atmosphere.

"*When many waves move through a region, rain occurs when conditions are favorable, thus leading to an eventual drying out of the atmosphere with saturation only just being reached during extreme events. The relative humidity of this state depends on the disturbance energy level. Evaporation of moisture from the surface will tend to restore moisture levels, however, thus balancing the tendency of the disturbances to*

dry out the atmosphere. The relative humidity of the atmosphere and the amount of precipitation that occurs depend on the balance between these processes."

Chapter 6

Conclusions and Discussion

6.1 Main Conclusions

Verification of Bonan's LSM by comparing the simulated with the diagnosed total runoff from NCEP/NCAR reanalysis data reported a problem that Bonan's LSM does not include the lateral water exchange between neighbouring grid cells caused by topographic slopes. Then, to fix this problem, based on previous research results on river re-distribution models, a modification on the original runoff parameterization was proposed and implemented in the original LSM. Analysis showed that the modification made the LSM physically more realistic in simulating the horizontal distribution pattern of total runoff, and furthermore, the improved LSM, as expected, forced the AGCM to give a more realistic climate.

Verification of the Original CCM3/LSM

Diagnosed runoff was estimated from NCEP/NCAR reanalysis data for an 8-year period from 1987 to 1994. Bonan's LSM was run for the same period coupled to

NCAR's CCM3. Comparisons between the diagnosed and simulated runoff indicate that, the runoff parameterization can regenerate the overall pattern of the diagnosed runoff over land but with substantial overestimates in some regions and underestimates in others. A closer look at the North America and the MRB shows that, the area integrals of runoff are fine in the MRB, but the runoff parameterization cannot reproduce the reasonable diagnosed horizontal distribution pattern of runoff, which is more important to the model climates. One of the possible reasons is that topographic effects are not included in the original runoff parameterization. Lateral water fluxes caused by topographic slopes not only affect the horizontal redistribution of runoff, but also directly affects the infiltration capacity.

Modification on the Original Runoff Parameterization

Based on some previous research results on river re-distribution models, modification on the original runoff parameterization was proposed and implemented into the original model (NCAR's CCM3/LSM). Modification is in two aspects: the topographic slopes cause outflows from higher topography (mountain tops) and inflows into the lower topography points (mountain feet). Topographic slopes will also cause decrease of infiltration at higher topography and increases of infiltration at lower topography. The surface runoff and infiltration are adjusted according to the topographic slopes between neighboring grid cells.

Impact of the Modification on the Land Surface Climate

Analysis from a regional scale perspective in the Canadian GEWEX basin, the Mackenzie River basin, shows that the modified runoff parameterization can generate the expected horizontal distribution pattern of total runoff, which is much closer

to the observed and diagnosed runoff horizontal distribution patterns, and which is much more consistent with topography and thus very easy to explain physically. This represents the improvements in runoff simulation over the original model.

Because the LSM uses infiltration as the boundary conditions to solve the soil hydraulic properties including the subsurface runoff, the modified model also changed other land surface climate variables. Consequently, the modified model gives less (more) sub-surface runoff at higher (lower) topography points where infiltration decreases (increases). Increases (decreases) of infiltration increase (reduce) the soil wetness at the top soil layer, and generally increase (reduce) the ground evaporation. Then surface latent and sensible heat fluxes are changed and as a result, surface temperature may also be changed.

Impact of the Modification on the Atmospheric Climate

Surface temperature was changed by the modification and our conclusions are consistent with previous studies. At higher topography points, the modification results in less infiltration into the soil; the reduced infiltration dries the soil, reduces the surface latent heat flux, and consequently raises the surface temperature. This mechanism is very clearly demonstrated in the point budgets analysis at the Andes Mountains vicinities. The analysis result and its interpretation in this thesis are more self-consistent than in some previous studies.

From a regional scale perspective, **time scale sensitivity analysis** shows that, the model is most sensitive to the modification at monthly time scale, less sensitive at seasonal scale and least sensitive at annual time scale.

More importantly, the modified model improved the original model on simulating the basic atmospheric climate properties such as, thermodynamic features (structure

of temperature and specific humidity), precipitable water, net water exchange, and precipitation.

In summer, the most significant improvement in the simulated vertical structure of zonally seasonally averaged **atmospheric temperature**, introduced by the modified model, is found at the north polar area by correcting the cold bias in the original model in the entire air column with a 1.2K maximum at the lower troposphere and the other at the upper troposphere; while the most significant improvement in winter is in the upper troposphere at the south polar area and the middle troposphere at the north polar region, where the modified model reduced the cold bias in the original model by over 0.6K. And improvements can also be found at many other regions.

Zonally seasonally averaged cross sections of **specific humidity** differences between the modified and the original CCM3/LSMs show the most obvious improvements in the tropics at lower troposphere, where the modified model reduced the moist bias in the original model by up to 0.2g/kg for both summer and winter seasons.

Because the precipitable water is defined as the vertical integral of the specific humidity, changes in the vertical structure of the specific humidity made by the modified model do not necessarily result in much difference in the **zonal- and seasonally averaged precipitable water** between the modified model and the original model. But slight improvements are still visible in our analysis.

The modified model also obviously improves the simulation of **horizontal distribution of the precipitable water** at the Amazon basin, South America, South Africa in winter; and at east side of the Rockies in North America, China - Russia area, especially at the vicinity of the Tibet Plateau, Central Africa, Northern Australia, and east part of Amazon basin in summer.

Generally the original CCM3/LSM overestimates the **zonally and annually precipitation rate** except at the ITCZ. While the modified model drags the curves closer

to the Xie and Arkin (1996) analysis at most of the Northern Hemisphere and some areas in Southern Hemisphere, The most significant improvement is found between 15N and 60N, and between the equator and 30S.

The modified model reduced the **evaporation** between 50N and 30S. This enhanced suppression of evaporation in the vicinity of ITCZ convection is a more realistic feature of the CCM3/LSM simulation, showing good agreement with corresponding oceanic estimates (e.g., see Oberhuber 1988; Doney et al. 1998; Kiehl 1998). The modified model more obviously reduced the seasonal mean evaporation rate between 20S and 30S in DJF, and between 30N and 60N in the JJA, where the maxima occur for corresponding seasons. Consequently, the modified model also reduced the zonal annually averaged **net water exchange** $E - P$, especially the source regions of total water.

Analysis of the **global distribution of precipitation** shows significant improvements introduced by the modification. The modified model gives very obvious corrections for every significant bias the original model gives as Hack et al. (1998) mentioned. Two very good examples directly related to topographic effects are the removal of the "precipitation lock" at the Andes Mountains in DJF (Hack et al. 1998) and the correction of the precipitation anomaly at the Tibet Plateau. These two examples illustrate that the modified LSM including topographic effects gives a more realistic AGCM climate.

The **simulated 1987 ENSO response** was examined by checking the longer-term average precipitation differences between DJF 1987 (warm event) and DJF 1989 (cold event). The modified model can still reproduce the main features of this ENSO event as the original model does. This implies that the modified model performs properly, even though the patterns of the zonal- seasonally averaged precipitation and evaporation are different from those in other studies. The most obvious improvement

by the modified model was found in the Indian Ocean. The original model gives a high there, while the modified model gives a low as in the observation.

Analysis on the **annual hydrologic cycle** shows that, the modified model slightly improved the original model between in September and October on the annual cycle simulation of precipitable water, possibly due to the fact that the modification in the runoff parameterization is more effective when there is more surface water supplies during summer and fall. The modified model also slightly improved the original model on the annual cycle simulation of the precipitation throughout the whole year except October, and also improved the annual cycle simulation of $E - P$ throughout the whole year.

Potential Impact of the Modification on the Environment

The modified model produced more **net CO_2 flux** over higher topographic areas, less CO_2 flux over lower topographic areas, when the modification on the runoff parameterization has stronger impact on the model climate in respective hemisphere seasons. And changes in the net CO_2 flux between the land surface and the atmosphere must have impact on other lower boundary layer variables through very complicated biochemical mechanism (Bonan 1996b; Bonan 1998), and further have impact on the atmospheric CO_2 distribution (Craig et al. 1998), thus must affect the carbon cycle in the global environment. According to Craig et al. (1998), the modified model may improve the atmospheric CO_2 simulation which is very important to global environmental studies.

Significance Check and Impact on Basic Atmospheric Waves

T-test scores show significant changes in total runoff, surface temperature, moisture, resulting in significant improvements in the basic atmospheric thermodynamic variables, humidity and temperature; and consequently, the modification significantly changed the basic atmospheric waves and thus some of the basic atmospheric circulation. This confirms again that the modification on the LSM makes the LSM more realistic in some areas and force the AGCM to produce a more realistic climate. It is the significant changes in the basic atmospheric structure that extends the impact of the LSM modification from land to regions other than land.

6.2 Discussion

There are many ways in which topography affects regional and global climate. This thesis affected one aspect of that: an indirect way, i.e., topography affects the regional and global climate via its impact on the land surface hydrological processes. In fact, the whole issue as to where precipitation falls in a mountainous region is very relevant to this study. The thesis "assumes" that this major problem is a "given" and then it considers the lateral transport of moisture arising from that precipitation and the sloping terrain.

Although improvement over the original model introduced by the modification is dominant in the analysis, some deficiencies can also be found at some areas. Some of the deficiencies are most possibly rooted in the AGCM, CCM3 in this case (Hack at el. 1998), for example, the cold polar tropopause simulations have been documented to be a pervasive problem in atmospheric circulation modeling (Boer et al. 1992). These kinds of deficiencies can be improved by improving the approximation of the numerical schemes in the AGCMs (Williamson and Olson 1998). However, a very encouraging conclusion is that the modified model even corrected some of these kinds

of deficiencies, such as the "precipitation lock" over the Andes Mountains, a problem in many other AGCMs (Hack et al. 1998).

The modified model gives a more realistic runoff horizontal distribution pattern. However, the calculation of the lateral water fluxes still needs to be refined. For example, the water flux calculation double counted the topographic height. This definitely introduced nonlinear effects on our adjustment on runoff and infiltration. To better testify the efficiency of the modification, longer model runs are needed, although the current 8-year run already shows many obvious improvements. This will be the next step on this study. Inter-comparison with other LSMs (CLASS, WATCLASS, etc.) will also help for further improvement on the runoff parameterization.

More work is also needed to verify the potential improvement the modification may introduce to the atmospheric CO_2 simulation which is very important to global environmental studies. And much more efforts are needed to give a quantitative explanation on the response of the Rossby waves to the modification in the LSM.

Bibliography

[1] Alestalo, M., 1983: The atmospheric water budget over Europe. In *Variations in the Global Water Budget.* (eds. A. Stree-Perrott and R Ratcliffe). D. Reidel Publ. Co., Dordrecht, Holland, 67-79

[2] Boer, G.J., 1992: Some results from and an intercomparison of the climates simulated by 14 atmospheric general circulation models. *J. Geophys. Res.*, **97**, 12771-12786

[3] Bonan, G.B., 1995: Sensitivity of a GCM simulation to inclusion of inland water surfaces. *J. Climate*, **8**, 2691-2704

[4] Bonan, G.B., 1996a: Sensitivity of a GCM simulation to sub-grid infiltration and surface runoff. *Climate Dyn.*, **12**, 279-285

[5] Bonan, G.B., 1996b: A land surface model (LSM version 1.0) for Ecological, Hydrological, and Atmospheric Studies: Technical description and user's guide. *NCAR Technical Note NCAR/TN-417+STR*, National Center for Atmospheric Research, Boulder, CO., 150pp

[6] Bonan, G.B., 1998: The land surface climatology of the NCAR land surface model coupled to the NCAR community climate model. *J. Climate*, **11**, 1307-1326

[7] Brubaker, K.L., D. Entekhabi, and P.S. Eagleson, 1994: Atmospheric water vapor transport and continental hydrology over the Americas. *J. Hydrol.*, **155**, 407-428

[8] Bryan, F. and A. Oort, 1984: Seasonal variation of the global water balance based on areological data. *J. Geophys. Res.*, **89** , 11717-11730

[9] Chervin, R.M., and S.H. Schneider, 1976: On determining the statistical significance of climate experiments with general circulation models. *J. Atmos. Sci.*, **33** , 405-412

[10] Cho, H.-R., and J. Liu, 2000: Improvement in runoff parameterization for regional and global climate modelling - A final report. *Proceedings of the 6th Scientific Workshop for the Mackenzie GEWEX Study [MAGS]*, November 14-17, 2000, Saskatoon. In press

[11] Cho, H.-R., and J. Liu, 2001: Verification of runoff parameterization using atmospheric reanalysis data. Submitted to *Tellus*

[12] Clapp, R.B., and G.M. Hornberger, 1978: Empirical equations for some soil hydraulic properties. *Water Resour. Res.*, **14**, 601-604

[13] Clarke, A.J., and X. Liu, 1993: Observations and dynamics of semiannual and annual sealevels near the eastern equatorial Indian Ocean boundary. *Journal of Physical Oceanography*, **23**, 386-399

[14] Coe, M.T., 1998: A linked global model of terrestrial hydrologic processes: Simulation of modern rivers, lakes and wetlands. *J. Geophys. Res.*, **103**, No. D8, 8885-8899

[15] Cosby, B.J., G.M. Hornberger, R.B. Clapp, and T.R. Ginn, 1984: A statistical exploration of the relations of soil moisture characteristics to the physical properties of soils. *Water Resour. Res.*, **20**, 682-690

[16] Craig, S.G., K.J. Holmen, G.B. Bonan, and P.J. Rasch, 1998: Atmospheric CO_2 simulated by the NCAR community climate model: I. Mean fields and seasonal cycles. *J. Geophys. Res.*, **103**, D11, 13213-13235

[17] Danielson, D. A., 1997: *Vectors and tensors in engineering and physics.*(2nd ed.), Reading, Mass.: Addison-Wesley Pub., 282pp

[18] Dickinson, R.E., A. Henderson-Sellers, and P.J. Kennedy, 1993: Biosphere-Atmosphere Transfer Scheme(BATS) version 1e as coupled to NCAR Community Climate Model. *NCAR Technical Note NCAR/TN-387+STR*, National Center for Atmospheric Research, Boulder, CO., 170pp

[19] Dolman, A.J., and D. Gregory, 1992: The parameterization of rainfall interception in GCMs. *Quart. J. Roy. Meteor. Soc.*, **118**, 455-467

[20] Doney, S.C., W.G. Large, and F.O. Bryan, 1998: Surface ocean fluxes and water mass transformation rates in the coupled NCAR Climate System Model. *J. Climate*, **11**, 1420-1441

[21] Ducoudre, N. I., K. Laval, and A. Perrier, 1993: SECHIBA, a new set of parameterizations of the hydrologic exchanges at land-atmosphere interface within the LMD atmospheric general circulation model. *J. Climate*, **6**, 248-273

[22] Entekhabi, D., and P.S. Eagleson, 1989: Land surface hydrology parameterization for atmospheric circulation models including subgrid scale spatial variability. *J. Climate*, **2**, 816-831

[23] Gill A.E., 1980: Some simple solutions for heat-induced tropical circulation. *Quart. J. Roy. Met. Soc.*, **106**, 447-462

[24] Gill A.E. (Ed), 1982a: Atmosphere-Ocean Dynamics. Academic Press, Inc., San Diego, California, 31-33

[25] Gill A.E., 1982b: Studies of moisture effects in simple atmospheric models: the stable case. *Geophys. Astrophys. Fluid Dynamics*, **19**, 119-152

[26] Hack, J.J., J.T. Kiehl, and J.W. Hurrell, 1998: The hydrologic and thermodynamic characteristics of the NCAR CCM3. *J. Climate*, **11**, 1179-1206

[27] Horinouchi, T., and S. Yoden, 1996: Exitation of transient waves by localized episodic heating in the tropics and their propagation into the middle atmosphere. *J. Meteo. Soc. of Japan*, **74**, 189-210

[28] Hornberger, G.M., J.P. Raffensperger, P.L. Wiberg, and K. Eshleman.(Ed), 1998: *Elements of physical hydrology*. Baltimore, MD: Johns Hopkins University Press, 314pp

[29] Jeffery T.K., J.H. James, B.B. Gordon, A.B. Byron, P.B. Bruce, L.W. David, and J.R. Philip, 1996: Description of the NCAR Community Climate Model (CCM3). *NCAR Technical Note NCAR/TN-420+STR*, National Center for Atmospheric Research, Boulder, CO., 142pp

[30] Johnson, K.D., D. Entekhabi, P.S. Eagleson, 1993: The implementation and validation of improved land surface hydrology in a atmospheric general circulation model. *J. Climate*, **6**, 1009-1026

[31] Kiehl, J.T., 1998: Simulation of the tropical Pacific warm pool with the NCAR Climate System Model. *J. Climate*, **11**, 1342-1355

[32] Kalnay, E., M. Kanamitsu, R. Kistler, W. Collins, D. Deaven, L. Gandin, M. Iredell, S. Saha, G. White, J. Woollen, Y. Zhu, M. Chelliah, W. Ebisuzaki, W. Higgins, J. Janowiak, K.C. Mo, C. Ropelewski, J. Wang, A. Leetmaa, R. Reynolds, Roy Jenne, and Dennis Joseph, 1996: The NCEP/NCAR 40-year reanalysis project. *Bull. Amer. Meteor. Soc.*, **77**, 437-478

[33] Karl, T.R., and W.E. Riebsame, 1984: The identification of 10- to 20-year temperature and precipitation fluctuations in contiguous United States. *J. Climate Appl. Meteor.*, **23**, 950-966

[34] Krauss, T.W., 1995: The Mackenzie GEWEX Study(MAGS): Basic Information and Critical Characteristics of the Mackenzie River Basin and its Energy and Water Fluxes. *A MAGS Internal Report*, 45pp

[35] Legates, D.R., and C.J. Willmott, 1990: Mean seasonal and spatial variability in gage-corrected, global precipitation. *Int. J. Climate*, **10**, 111-127

[36] Liston, G. E., Y.C. Sud, and E.F. Wood, 1994: Evaluating GCM land surface hydrology parameterization by computing river discharges using a runoff routing model: application to Mississippi basin. *J. Appl. Meteor.*, **33**, 394-405

[37] Liu, J., H.-R. Cho, and R. E. Stewart, 2001: Characteristics of the water vapour transport over the Mackenzie River Basin during the 1994-95 water year. Accepted by *Atmosphere - Ocean*

[38] Liu, J., and H.-R. Cho, 2001a: Estimating atmospheric moisture flux convergence using the Green's Theorem. To be submitted to *Int. J. Climatol.*

[39] Liu, J., and H.-R. Cho, 2001b: An improved runoff parameterization for global climate modelling. To be submitted to *J. Climate*

[40] Matthews, G.J., and R. Morrow, Jr., (Ed).1995: *Canada and the world*, (2nd ed.). Scarborough, ON : Prentice Hall Canada, 210pp

[41] Miller, J.R., G.L. Russel, and G. Caliri, 1994: Continental-scale river flow in climate models. *J. Climate*, **7**, 914-928

[42] Oberhuber, J.M., 1988: An atlas based on the "COADS" dataset: The budgets of heat, boyancy and turbulent kinetic energy at the surface of the global ocean. Max-Planck Institute for Meteorology Rep. 15, 199pp

[43] Oki, T., K. Musiake, H. Matsuyama, and K. Masuda, 1995: Global atmospheric water balance and runoff from large river basins. In *Scale Issues in Hydrological Modelling* , (eds. J. D. Kalma and M. Sivapalan), John Wiley & Sons, Chichester, Toronto, 411-434

[44] Peixoto, J.P., 1970: Pole to pole divergence of water vapor. *Tellus*, **22**, 17-25

[45] Peixoto, J.P., 1973: Atmospheric water vapor flux computations for hydrological purposes. *WMO Publ.*, **No. 357**, WMO, Geneva, 83pp

[46] Peixoto, J.P. and A.H. Oort, 1983: The atmospheric branch of the hydrological cycle and climate. In: *Variations in the Global Water Budget*, (eds. A. Stree-Perrott and R Ratcliffe), D. Reidel Publ. Co., Dordrecht, Holland, 5-55

[47] Pinsky, M.A., (Ed), 1991: *Partial Differential Equations and Boundary-Value Problems with Applications*, 2nd Edition, McGraw-Hill, Inc., New York, 78-81

[48] Pitman, A.J., 1991: A simple parameterization of sub-grid scale open water for climate models. *Climate Dyn.*, **6**, 99-112

[49] Pitman, A.J., A. Henderson-Sellers, and Z-L., Yang, 1990: Sensitivity of regional climates to localized precipitation in global models. *Nature*, **346**, 734-737

[50] Pitman, A.J., Z-L., Yang, J. G. Cogley, and A. Henderson-Sellers, 1991: Description of bare essentials of surface transfer for the Bureau of Meteorology Research Center AGCM. *Bur. Meteor. Res. Center Rep.*, **32**, 117pp

[51] Pitman, A.J., Z-L., Yang, and A. Henderson-Sellers, 1993: Sub-grid scale precipitation in AGCMs: re-assessing the land surface sensitivity using a single column model. *Climate Dyn.*, **9**, 33-41

[52] Press, W.H., S.A. Teukolsky, W.T. Vetterling, and B.P. Flannery, (Ed), 1996: Numerical Recipes in Fortran 90: the art of parallel scientific computing, 2nd Edition, Cambridge University Press, New York, USA, 498-504, 881-894

[53] Randel, D.L., T.H. Vonder Haar, M.A. Ringerud, G.L. Stephens, T.J. Greenwald, and C.L. Combs, 1996: A new global water vapor dataset. *Bull. Amer. Meteor. Soc.*, **77**, 1233-1246

[54] Rasmusson, E.M., 1968: Atmospheric water vapor transport and the water balance of North America. II: Large-scale water balance investigations. *Mon. Wea. Rev.*, **96**, 720-734

[55] Rasmusson, E.M., 1977: Hydrological application of atmospheric vapor-flux analyses. *Hydrol. Rep.*, **11**, WMO, Geneva, 50pp

[56] Sellers, P.J., Y. Mintz, Y.C. Sud, and A. Dalcher, 1986: A simple biosphere model(SiB) for use within general circulation models. *J. Atmos. Sci.*, **43**, 505-531.

[57] Serreze M.C., et al., 1995: Atmospheric Water Vapor Characteristics at 70°N. *J. Climate*, **8**, 719-731

[58] Starr, V.P., and J.P. Peixoto, 1958: On the global balance of water vapor and hydrology of deserts. *Tellus*, **10**, 189-194

[59] Soulis, E.D., N. Kouwen, F. Segelenieks, K. Snelgrove, E. Whidden, A. Graham, M. Lee, and S. Solomon, 2000: New development in WATFLOOD for coupling to CLASS. Presented on the *2nd Workshop on MAGS and CAGES Analysis*.March 31, 2000, Waterloo, Canada

[60] Stewart, R.E., N. Bussieres, Z. Cao, H.-R. Cho, J. Liu, B. Kochtubajda, H. Leighton, P.Y.T. Louie, M.D. Mackay, P. Marsh, J. Pomeroy, T.D. Prowse, E.D. Soulis, K.K.Szeto and A.E. Walker, 2001: On the atmospheric, surface and hydrological processes influencing the Mackenzie Basin climate system during the 1994/1995 water year: a period of record low discharge. Accepted by *Atmosphere-Ocean*

[61] Thomas, L.A., E.B. Lawrence, M.R. James, and E.T. John, 1996: User's Guide to NCAR CCM3. *NCAR Technical Note NCAR/TN-421+STR*, National Center for Atmospheric Research, Boulder, CO., 210pp

[62] Trenberth, K.E. and C.J. Guillemot, 1996: Evaluation of the atmospheric moisture and hydrological cycle in the NCEP reanalysis. *NCAR Technical Note NCAR/TN-430+STR*, National Center for Atmospheric Research, Boulder, CO., 308pp

[63] Verseghy, D.L., 1991: CLASS-A Canadian land surface scheme for GCMs. I: Soil model. *Int. J. Climatol.*, **11**, 111-133

[64] Verseghy, D.L., N.A. McFarlance, and M. Lazare, 1993: CLASS-A Canadian land surface scheme for GCMs. II: Vegetation model and coupled runs. *Int. J. Climatol.*, **13**, 347-370

[65] Walsh, J.E., X. Zhou, D. Portisi and M.C. Serreze, 1994: Atmospheric contribution to hydrologic variations in Arctic, *Atmosphere-Ocean*, **32**, 733-755

[66] Wang B., 1988: Dynamics of tropical low-frequency waves: An analysis of the moist Kelvin wave, *J. Atmos. Sci.* , **45**, 2051-2065

[67] Wang B., and H. Rui, 1990: Dynamics of the coupled moist Kelvin-Rossby wave on an equatorial β-plane, *J. Atmos. Sci.* , **47**, 397-413

[68] Wang B., and X. Xie, 1996: Low-frequency equatorial waves in vertically sheared zonal flow, Part I: stable waves, *J. Atmos. Sci.* , **53**, 449-467

[69] Webster, P.J., 1972: Response of the tropical atmosphere to local steady forcing, *Mon. Wea. Rev.* , **100**, 518-541

[70] Williamson, D.L., and J.G. Olson, 1998: A comparison of semi-Lagragian and Eulerian polar climate simulation. *Mon. Wea. Rev.*, **126**, 991-1000

[71] Xie, P., and P.A. Arkin, 1996: Analyses of global monthly precipitation using gauge observations, satellite estimates, and numerical model predictions. *J. Climate*, **9**, 840-858

[72] Xie, X., and B. Wang, 1996: Low-frequency equatorial waves in vertically sheared zonal flow, Part II: unstable waves, *J. Atmos. Sci.* , **53**, 3589-3605

[73] Xue, Y., P.J. Sellers, J.L. Kinter, and J. Shukla, 1991: A simplified biosphere model for global climate studies. *J. Climate*, **4**, 345-364